Design of a Shape Memory Alloy Actuator for Soft Wearable Robots

by

Álvaro Villoslada Peciña

A dissertation submitted in partial fulfillment of the requirements for the degree of Doctor of Philosophy in

Electrical Engineering, Electronics and Automation

Universidad Carlos III de Madrid

Advisors:

Luis Enrique Moreno Lorente
María Dolores Blanco Rojas

Tutor:

Luis Enrique Moreno Lorente

June 2019

Imagination will often carry us to worlds that never were,
but without it we go nowhere.
Carl Sagan

Acknowledgments

Since this section is more informal than the rest of the present document, I would like to express my gratitude in my mother tongue.

En primer lugar, y como no puede ser de otra forma, tengo que agradecerles a mis directores de tesis, Luis y Dolores, el haberme dado esta oportunidad. Cuando me comentasteis la posibilidad de realizar una tesis doctoral con vosotros, yo me encontraba con el máster recien acabado, un poco perdido, buscando trabajo, pero con unas ganas enormes de poder continuar trabajando en el campo de la investigación. Para mí, trabajar como investigador es lo más parecido a ver el sueño de mi infancia cumplido: ser inventor. Por eso, no dudé ni un segundo en aceptar vuestra propuesta, y aquí estamos. En especial, quiero agradeceros vuestra dedicación y paciencia en el intenso tramo final de la tesis.

Al profesor Mohamed Abderrahim, al que tengo un gran aprecio desde que le pude conocer mejor al trabajar con él allá por el año 2011, tengo que agradecerle toda la ayuda que me ha prestado en calidad de Director del Programa de Doctorado en los últimos días de la tesis. Muchas gracias, de todo corazón.

También quiero agradecerle a Manuel Prieto la ayuda y el apoyo que me ha dado para poder acabar la tesis. En gran medida, te debo a ti el haber podido terminarla.

Aunque llevo ya más de un año alejado de la Universidad, nunca me olvido de la gente del Robotics Lab. Tanto de los que ya os fuisteis, Tamara Ramos, Javier Quijano, Víctor Pacheco, Martin Stoelen, David Álvarez, Silvia Rodríguez, como de los que aún seguís por allí dando guerra, Jorge Muñoz, Juan G. Victores, José Carlos Castillo, David Estévez, Dorin Copaci, Fernando Martín... En fin, toda esa gente (que sois muchos) que le dais el toque humano al Robotics Lab de la UC3M. Mención aparte merecen los técnicos de laboratorio, Ángela Nombela y Fernando San Deogracias; gracias por estar siempre ahí, dispuestos a ayudar en lo que pudieseis.

Por último (porque suele hacerse así; vosotros sabéis que siempre ocupáis el primer puesto) tengo que dar las gracias a mi familia. A mis padres, Concha y Miguel Ángel, a mi hermano, Miguel, y a mi pareja, Andrea. Vosotros habéis hecho y hacéis de mí gran parte de lo que soy. Probablemente esta tesis estaría a medio acabar, olvidada en alguna carpeta de mi ordenador, si no hubiera sido por vuestro apoyo, motivación y ayuda, pero sobre todo, por vuestro cariño. Os quiero mucho a todos.

Published and presented contents

- **A. Villoslada**, C. Rivera, N. Escudero, F. Martín, D. Blanco, L. Moreno, *Hand exo-muscular system for assisting astronauts during Extravehicular Activities*, Soft Robotics, vol. 6, no. 1, pp. 21-37, 2019, DOI: 10.1089/soro.2018.0020.

  Main author. Totally included in Chapter 6. The material from this source included in the thesis is not indicated by typographical means or references.

- **A. Villoslada**, N. Escudero, F. Martín, A. Flores, C. Rivera, M. Collado, L. Moreno, *Position control of a shape memory alloy actuator using a four-term bilinear PID controller*, Sensors and Actuators A: Physical, vol. 236, pp. 257-272, 2015, DOI: 10.1016/j.sna.2015.10.006.

  Main author. Totally included in Chapter 5. The material from this source included in the thesis is not indicated by typographical means or references.

- **A. Villoslada**, A. Flores, D. Copaci, D. Blanco, L. Moreno, *High-displacement flexible shape memory alloy actuator for soft wearable robots*, Robotics and Autonomous Systems, vol. 14, pp. 91-101, 2015, DOI: 10.1016/j.robot.2014.09.026.

  Main author. Partially included in Chapter 3. The material from this source included in the thesis is not indicated by typographical means or references.

- **A. Villoslada**, A. Flores, D. Copaci, D. Blanco, L. Moreno, *High-displacement fast-cooling flexible SMA actuator: application to an anthropomorphic robotic hand*, in: 2014 14th IEEE-RAS International Conference on Humanoid Robots (Humanoids), pp. 27-32, 2014, DOI: 10.1109/HUMANOIDS.2014.7041333.

  Main author. Partially included in Chapter 3. The material from this source included in the thesis is not indicated by typographical means or references.

Other research merits

- A. Flores, D. Copaci, **A. Villoslada**, D. Blanco, L. Moreno, *Sistema Avanzado de Protipado Rápido para Control en la Educación en Ingeniería para grupos Multidisciplinares*, Revista Iberoamericana de Automática e Informática Industrial (RIAI), vol. 13, pp. 350-362, 2016.
- D. Copaci, A. Flores, **A. Villoslada**, D.s Blanco, *Modelado y simulación de actuadores SMA con carga variable*, in: Proceedings of the XXXVI Jornadas de Automática, pp. 481-486, Bilbao, Spain, Sep. 2015.
- M. Collado, C. Rivera, N. Escudero, **A. Villoslada**, F. Martín, L. Moreno, *Exomuscular Systems Based On SMA For Space Suits*, in: SMST-2015: The Model for Shape Memory Application, Proceedings of the Shape Memory and Superelastic Technologies Conference, Chipping Norton, Oxfordshire, UK, May. 2015.
- M. Collado, C. Rivera, N. Escudero, **A. Villoslada**, F. Martín, L. Moreno, *Flexible Exo-Muscular Actuators based on SMA for Space Robotics*, in: Plan the European Roadmap and its Activities for Space Exploitation of Robotics and Autonomy (PERASPERA) workshop, Noordwijkerhout, The Netherlands, Feb. 2015.

Abstract

Soft robotics represents a paradigm shift in the design of conventional robots; while the latter are designed as monolithic structures, made of rigid materials and normally composed of several stiff joints, the design of soft robots is based on the use of deformable materials such as polymers, fluids or gels, resulting in a biomimetic design that replicates the behavior of organic tissues. The introduction of this design philosophy into the field of wearable robots has transformed them from rigid and cumbersome devices into something we could call exo-suits or exo-musculatures: motorized, lightweight and comfortable clothing-like devices.

If one thinks of the ideal soft wearable robot (exoskeleton) as a piece of clothing in which the actuation system is fully integrated into its fabrics, we consider that that existing technologies currently used in the design of these devices do not fully satisfy this premise. Ultimately, these actuation systems are based on conventional technologies such as DC motors or pneumatic actuators, which due to their volume and weight, prevent a seamless integration into the structure of the soft exoskeleton.

The aim of this thesis is, therefore, to design of an actuator that represents an alternative to the technologies currently used in the field of soft wearable robotics, after having determined the need for an actuator for soft exoskeletons that is compact, flexible and lightweight, while also being able to produce the force required to move the limbs of a human user. Since conventional actuation technologies do not allow the design of an actuator with the required characteristics, the proposed actuator design has been based on so-called emerging actuation technologies, more specifically, on shape memory alloys (SMA).

The mechanical design of the actuator is based on the Bowden transmission system. The SMA wire used as the transducer of the actuator has been routed into a flexible sheath, which, in addition to being easily adaptable to the user's body, increases the actuation bandwidth by reducing the cooling time of the SMA element by 30 %. At its nominal operating regime, the actuator provides an output displacement of 24 mm and generates a force of 64 N.

Along with the actuator, a thermomechanical model of its SMA transducer has been developed to simulate its complex behavior. The developed model is a useful tool in the design process of future SMA-based applications, accelerating development

time and reducing costs. The model shows very few discrepancies with respect to the behavior of a real wire. In addition, the model simulates characteristic phenomena of these alloys such as thermal hysteresis, including internal hysteresis loops and return-point memory, the dependence between transformation temperatures and applied force, or the effects of latent heat of transformation on the wire heating and cooling processes.

To control the actuator, the use of a non-linear control technique called four-term bilinear proportional-integral-derivative controller (BPID) is proposed. The BPID controller compensates the non-linear behavior of the actuator caused by the thermal hysteresis of the SMA. Compared to the operation of two other implemented controllers, the BPID controller offers a very stable and robust performance, minimizing steady-state errors and without the appearance of limit cycles or other effects associated with the control of these alloys.

To demonstrate that the proposed actuator together with the BPID controller are a valid solution for implementing the actuation system of a soft exoskeleton, both developments have been integrated into a real soft hand exoskeleton, designed to provide force assistance to astronauts. In this case, in addition to using the BPID controller to control the position of the actuators, it has been applied to the control of the assistive force provided by the exoskeleton. Through a simple mechanical multiplication mechanism, the actuator generates a linear displacement of 54 mm and a force of 31 N, thus fulfilling the design requirements imposed by the application of the exoskeleton. Regarding the control of the device, the BPID controller is a valid control technique to control both the position and the force of a soft exoskeleton using an actuation system based on the actuator proposed in this thesis.

Resumen

La robótica flexible (*soft robotics*) ha supuesto un cambio de paradigma en el diseño de robots convencionales; mientras que estos consisten en estructuras monolíticas, hechas de materiales duros y normalmente compuestas de varias articulaciones rígidas, el diseño de los robots flexibles se basa en el uso de materiales deformables como polímeros, fluidos o geles, resultando en un diseño biomimético que replica el comportamiento de los tejidos orgánicos. La introducción de esta filosofía de diseño en el campo de los robots vestibles (*wearable robots*) ha hecho que éstos pasen de ser dispositivos rígidos y pesados a ser algo que podríamos llamar exo-trajes o exo-musculaturas: prendas de vestir motorizadas, ligeras y cómodas.

Si se piensa en el robot vestible (exoesqueleto) flexible ideal como una prenda de vestir en la que el sistema de actuación está totalmente integrado en sus tejidos, consideramos que las tecnologías existentes que se utilizan actualmente en el diseño de estos dispositivos no satisfacen plenamente esta premisa. En última instancia, estos sistemas de actuación se basan en tecnologías convencionales como los motores de corriente continua o los actuadores neumáticos, que debido a su volumen y peso, hacen imposible una integración completa en la estructura del exoesqueleto flexible.

El objetivo de esta tesis es, por tanto, el diseño de un actuador que suponga una alternativa a las tecnologias actualmente utilizadas en el campo de los exoesqueletos flexibles, tras haber determinado la necesidad de un actuador para estos dispositivos que sea compacto, flexible y ligero, y que al mismo tiempo sea capaz de producir la fuerza necesaria para mover las extremidades de un usuario humano. Dado que las tecnologías de actuación convencionales no permiten diseñar un actuador de las características necesarias, se ha optado por basar el diseño del actuador propuesto en las llamadas tecnologías de actuación emergentes, en concreto, en las aleaciones con memoria de forma (SMA).

El diseño mecánico del actuador está basado en el sistema de transmisión Bowden. El hilo de SMA usado como transductor del actuador se ha introducido en una funda flexible que, además de adaptarse facilmente al cuerpo del usuario, aumenta el ancho de banda de actuación al reducir un 30 % el tiempo de enfriamiento del elemento SMA. En su régimen nominal de operación, el actuador proporciona un desplazamiento de salida de 24 mm y genera una fuerza de 64 N.

Además del actuador, se ha desarrollado un modelo termomecánico de su transductor SMA que permite simular su complejo comportamiento. El modelo desarrollado es una herramienta útil en el proceso de diseño de futuras aplicaciones basadas en SMA, acelerando el tiempo de desarrollo y reduciendo costes. El modelo muestra muy pocas discrepancias con respecto al comportamiento de un hilo real. Además, es capaz de simular fenómenos característicos de estas aleaciones como la histéresis térmica, incluyendo los bucles internos de histéresis y la memoria de puntos de retorno (*return-point memory*), la dependencia entre las temperaturas de transformacion y la fuerza aplicada, o los efectos del calor latente de transformación en el calentamiento y el enfriamiento del hilo.

Para controlar el actuador, se propone el uso de una técnica de control no lineal llamada controlador proporcional-integral-derivativo bilineal de cuatro términos (BPID). El controlador BPID compensa el comportamiento no lineal del actuador causado por la histéresis térmica del SMA. Comparado con el funcionamiento de otros dos controladores implementados, el controlador BPID ofrece un rendimiento muy estable y robusto, minimizando el error de estado estacionario y sin la aparición de ciclos límite u otros efectos asociados al control de estas aleaciones.

Para demostrar que el actuador propuesto junto con el controlador BPID son una solución válida para implementar el sistema de actuación de un exoesqueleto flexible, se han integrado ambos desarrollos en un exoesqueleto flexible de mano real, diseñado para proporcionar asistencia de fuerza a astronautas. En este caso, además de utilizar el controlador BPID para controlar la posición de los actuadores, se ha aplicado al control de la fuerza proporcionada por el exoesqueleto. Mediante un simple mecanismo de multiplicación mecánica, el actuador genera un desplazamiento lineal de 54 mm y una fuerza de 31 N, cumpliendo así con los requisitos de diseño impuestos por la aplicación del exoesqueleto. Respecto al control del dispositivo, el controlador BPID es una técnica de control válida para controlar tanto la posición como la fuerza de un exoesqueleto flexible que use un sistema de actuación basado en el actuador propuesto en esta tesis.

Contents

List of Tables

List of Figures

Chapter 1

Introduction

1.1 Motivation

What if we humans could use some kind of external wearable device, as comfortable as our everyday clothing, powered by muscle-like actuators, that would amplify our strength, make us less prone to injury while performing physically demanding tasks, improve our quality of life during aging or even help us explore the confines of the universe? These "power suits" that are part of popular culture thanks to science fiction works such as Starship Troopers, Aliens, Metal Gear or Iron Man are, in fact, the object of study of one of the fields in robotics that, in terms of the number of publications and commercially available devices, is experiencing a great growth in the present day: the field of wearable robotics.

The term *wearable robot* encompasses two families of devices: exoskeletons and robotic prostheses [1]. The former are the external wearable devices mentioned above, designed to provide force augmentation (empowering robotic exoskeletons) or motion assistance (orthotic robots) to the human wearer. Their applications range from the military field (increasing the soldiers' endurance allowing them to carry more weight), the heavy industry (reducing the workers' fatigue) or the medical field (as rehabilitation or assistive devices). Exoskeletons can be either full-bodied or cover only a specific part of the body (elbow, hand, knee...). Robotic prostheses, on the other hand, are designed to replace a lost limb with an mechatronic artificial counterpart and its purpose is to replicate as closely as possible the functionality of the missing limb.

Designing a highly dexterous robotic hand or an exoskeleton whose control is almost transparent to the user, capable of accurately reproducing the human function they replace, assist or enhance, remains an open challenge, mainly because of their actuation systems (and also due to the complexity of controlling these devices). Think of the number of "actuators" our body has: the hand alone needs more than thirty muscles to reach the degree of dexterity it has. Building a robotic hand with such a large number of actuators using conventional actuation technologies would result in a device with such a size and weight that it would be unusable as a prosthesis. This problem is further aggravated in the case of exoskeletons since, in addition to their actuation systems, their rigid structures also add to the bulkiness and weight of the device. However, a recent trend in robot design can help solve some of these problems.

Soft robotics has emerged over the last decade as an alternative to the conventional design approach of "hard" robots. Traditionally, robots have been designed as rigid structures, composed of hard links and discrete joints that can move only in one rotational or translational direction, which hinders their adaptability to unstructured environments and makes them dangerous in their interaction with humans. Taking inspiration from nature, soft robots are mostly or totally made of deformable materials such as soft polymers, fabrics, fluids or gels [2].

It should be noted that throughout this thesis, when using the term *soft robotics*, we are referring to those devices in which softness is achieved passively, thanks to the properties of the materials with which they are made. Although this is the common definition of soft robotics, there is a second approach to achieve a soft interaction between the robot and its surroundings. This second category includes those robots that, despite having rigid bodies, are considered as part of the soft robotics field because the stiffness of their actuators can be adjusted using impedance or compliance controllers [3].

By using a flexible body with distributed deformation instead of an articulated structure with discrete joints, soft robots theoretically have an infinite number of degrees of freedom [4]; one can think of the deformable structure of a soft robot as a set of infinite joints that can stretch, compress and rotate in any direction. This property of soft robots implies that they are highly adaptable to unstructured environments since they can easily conform to unknown obstacles and their high dexterity allows them to manipulate objects of different sizes and shapes. Also, their robustness is superior to that of conventional robots because impact forces are absorbed by their soft body and distributed over a larger volume [5]. These features not only make soft robots capable of operating in a wide range of environments, with potential applications in search and rescue or disaster response scenarios, but also allow them to safely interact with humans, leading to the design of better personal, medical and assistive robots [2].

Precisely in the area of assistive robotics, wearable devices for human motion assistance can be greatly benefited from this paradigm shift in robot design. Within this field, a new kind of devices known as soft exoskeletons are the result of applying the soft robotics design principles to the fundamental idea behind conventional rigid exoskeletons, which is to augment, reinforce or restore human performance by means of an actuated wearable device. In a soft exoskeleton, the rigid frame of a conventional exoskeleton is replaced by textiles that transmit the forces generated by the actuators to the user's limbs and provide support for the actuators, electronics and power sources. This is the major advantage of soft exoskeletons over rigid ones, since it solves one of the most difficult problems to avoid in conventional exoskeletons: kinematic incompatibility [1]. Rigid exoskeletons have to be carefully designed from a kinematic point of view because their kinematic chain overlaps that of the human body. Since the latter is very complex and difficult to replicate, usually the differences between the two cause interaction forces, joint misalignment and motion restrictions, which ultimately cause discomfort and difficulties in controlling the device. By getting rid of the rigid frame, soft exoskeletons do not have a kinematic chain in the strict sense of the word, which means that there are no joints that must be aligned with those of the human wearer.

The adoption of the soft robotics approach in the design of exoskeletons also involves a change in the actuation systems of these devices. In a rigid frame exoskeleton, the actuators are usually installed on the joints of the device, applying the torque directly to the biological joint over which they are located. In the mechanical structure of a soft exoskeleton, however, there are no joints over which the actuators can be placed. For this reason, a bio-inspired approach is often adopted, with actuation and transmission systems that mimic the human musculoskeletal system, replicating the tendons, ligaments and muscles of the human body with artificial counterparts. This results in actuation systems in which the actuators do not transfer torque directly to the user's biological joints, but rather drive them remotely by means of cables. This is the usual arrangement when using tension-based actuators, such as DC motors or pneumatic artificial muscles. Other soft actuators are designed to produce a bending or linear motion, or a combination of both. In this case, the actuators are placed over the biological joints they mobilize as in a rigid frame exoskeleton, except that these actuators are lightweight and inherently compliant.

Despite all these years of research and innovation in soft actuation systems, the main technologies currently in use still fail in enabling the design of truly flexible, lightweight and compact devices. Although desirable, these features are not necessarily required in the design of actuators for soft robots, but in the specific case of soft wearable robots, they are mandatory if one wants to design a truly portable and wearable device. However, if the main technologies on which soft actuators are based (pneumatics, hydraulics, granular jamming and cable driven systems) are analyzed, they all share a common problem: they depend on some stiff and heavy element to operate, as will be seen in Section 1.2. Take, for example, a cable driven transmission; in this case, the driving force is provided by a DC motor which, given that it must be powerful enough to meet the force requirements of wearable devices, is bulky, heavy and probably requires a gearbox that makes its output stiffer. In the case of pneumatic devices, although the actuator itself can be built using compliant and flexible materials (as is the case of McKibben artificial muscles or actuators made of elastomeric materials), a pressure source, usually a compressor, is needed to provide the driving force. Hydraulic actuators face a similar problem: pumps and pressure regulators are necessary to displace the fluid, as well as a tank to store it. Having all these external elements is not only a problem if one wants to use these soft actuators in an untethered robot; it also shares the disadvantages of cable driven transmissions when it comes to their miniaturization and weight reduction, since compressors and pumps use DC motors to operate [6]. This might not be an issue if using the described actuators in non-mobile soft robots or in conventional exoskeletons, where the added weight and volume are not as relevant when compared to the structure of the device, but if the aim is to design a clothing-like powered system, the use of rigid and heavy elements should be avoided.

For the above reasons, it can be concluded that the design of a flexible and lightweight actuator capable of delivering high forces remains one of the biggest challenges in the soft robotics field [7, 8]. In the particular case of soft wearable robots, there is a need for an actuation system that can be integrated with the fabrics that compose the structure of the device, with no rigid elements that restrict the wearer's natural range of motion or increase the volume and weight of the robot. This need is leading to increasing research efforts into emerging actuation technologies applied to the soft robotics field, technologies that allow the miniaturization and weight reduction of the actuators without compromising their mechanical power delivery. For this purpose, some of the so-called smart materials, such as electroactive polymers (EAP), piezoelectric crystals or shape memory alloys (SMA), are particularly interesting since their main performance parameters (force density, bandwidth, power density...) scale positively upon miniaturization, in contrast to conventional actuation technologies.

Among the materials listed above, SMAs possess a number of features that make them appealing to be used as transducers in the design of new actuators for soft robots. An SMA is a metallic alloy (being Nickel and Titanium the most common metals used in its manufacturing) that can recover a predefined (memorized) shape after being subjected to a plastic deformation, thanks to a thermally triggered crystalline phase transformation process called shape memory effect (SME). Depending on the memorized shape, linear, bending or twisting motions can be obtained from this phase transformation, a property that can be exploited in the design of a variety of devices and actuators. Another property that defines NiTi-based SMAs is pseudoelasticity, a physical feature by which an SMA above can be subjected to large deformations without suffering a plastic deformation when an almost constant stress is applied to the material. While the SME is used in active applications, pseudoelasticity is exploited in passive elements such as dampers, pipe couplers, orthodontic wires... Due to the unique properties of SMAs, their use spans an array of applications in aerospace, structural or mechanical engineering, in the medical field or in robotics [9].

Considering its active application as transducers, the main attribute that characterizes SMA-based actuators and sets them apart from other actuation technologies is their high force density, which is defined as the ratio of maximum available force to the volume or weight of the actuator. For a given volume, an actuator using an SMA wire transducer in an axial deformation configuration outperforms conventional actuation technologies, such as pneumatic or hydraulic actuators, and has the highest force density among existing emerging technologies [10]. This property enables the design of very compact and lightweight actuators, due to the reduced volume of the transducer, yet capable of delivering forces at par with other heavier and bulkier technologies. Certainly, these materials are not exempt from problems when used as active transducers in the design of new actuators, and precisely these drawbacks prevent their widespread use despite the advantages they offer. The most noteworthy are their low actuation bandwidth, their thermal hysteresis that causes problems in their control and the limited displacements with respect to their total length that they produce.

Concerning the field of soft wearable robotics, SMA-based actuators, and more specifically those that use a wire of this material as a transducer, have a number of very attractive features. Naturally, the already mentioned high force density allows an actuation system based on these alloys to have a very reduced size and weight, an important aspect in this subfield of wearable robotics, but at the same time capable of generating the necessary force to mobilize the user's limbs. If we think of the ideal soft wearable robot as a device that does not differ much from normal clothing, the biomimetic behavior similar to that of the human muscles that SMA wires exhibit would allow the design of some sort of "exomusculature", a simple garment that would amplify the wearer's strength. Its silent operation should also not be neglected, as the noise made by conventional actuators can be a major nuisance to the user after an extended session using a wearable robot. Naturally, the problems mentioned above regarding their low strain, low actuation bandwidth and nonlinear behavior should be addressed in order to have a device that would be a real alternative to the actuation technologies currently used in this field.

What we propose in this thesis is that, through a proper mechanical design and designing control system able to overcome the controllability difficulties of these alloys, SMAs have a great potential to design the kind of actuator wanted by the soft wearable robotics community, a powerful actuator that is flexible, lightweight and easily integrable into fabrics and clothing.

1.2 Brief overview of soft wearable robots

In this section we are going to briefly review the existing literature in the field of soft wearable robots, to get to know the main trends regarding the design of these devices and their actuation systems. Practically all soft exoskeletons are meant for rehabilitation purposes, which makes sense if one considers that in the absence of a rigid structure, it is the user's body that has to withstand the applied loads. For this reason, soft devices cannot be used for heavy-duty tasks, unlike some conventional exoskeletons such as those emerging in the automotive industry, whose rigid structures are capable of absorbing these high loads.

Soft exoskeletons, on the other hand, are designed to assist those people who, either because of their age or because of some medical condition, need movement and force assistance to rehabilitate impaired motor functions or to carry out their activities of daily life (ADL). An example of this type of device aimed at restoring lost motor functions is the hand exoskeleton designed by Seoul National University [11, 12]. This device, aimed at restoring basic hand functionality, consists of a glove used as the interface between the user's fingers and the actuation system. Using a glove as the supporting element of a hand exoskeleton fulfills the features of flexibility, absence of rigid elements, low volume and comfort that characterize soft exoskeletons. Other examples of this type of design can be found in the works of Nilsson *et al.* [13], Fausti and Seneci [14], Delph *et al.* [15] and Nycz *et al.* [16] (Figure 1.1).

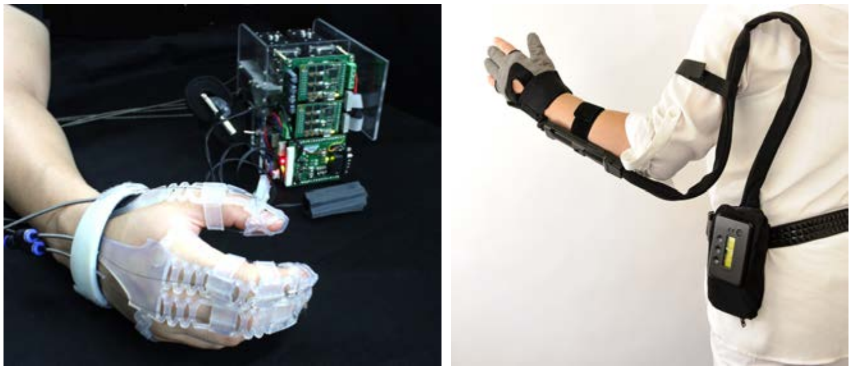
(a) (b)

Figure 1.1: Cable-driven soft hand exoskeletons: (a) SNU Exo-Glove Poly [12] and (b) SEM glove [13] (reproduced with the permission of the authors).

All the above exoskeletons are cable-driven (or tendon-driven) devices in which the actuation system consists of a set of DC motors remotely placed (housed inside a backpack or another kind of portable structure as Figure 1.1 shows) and that use a series of cables that play the role of artificial tendons to transmit the generated motion and force to the fingers. A common practice to reduce the complexity, size and weight of cable-driven hand exoskeletons is to use less actuators than degrees of freedom, which is known as underactuation. Most devices use one actuator per finger, but some devices use more complex grasping adaptation mechanisms that allow manipulating objects of different shapes with less actuators than fingers [17].

The soft robotics design principles can also be applied to the actuators of soft exoskeletons, so that they can be easily integrated into the device itself. These actuators are made of elastomeric materials and they generally work by changing the pressure of a fluid contained inside the actuator. There is a subtype of this method called granular jamming actuation that, instead of using a fluid to generate motion, uses a granular material contained inside a soft membrane which changes from a fluid-like state to a solid one when negative pressure is applied [18]. Soft pressurizable actuators are usually used in hand exoskeletons, as can be seen in the publications of Polygerinos *et al.* [19, 20, 21], Yap *et al.* [22], Thompson-Bean *et al.* [18] and Yun *et al.* [23] (Figure 1.2).

(a) (b)

Figure 1.2: Soft pressurizable hand exoskeletons: (a) Polygerinos *et al.* [20] and (b) SNU Exo-Glove PM [23] (reproduced with the permission of the authors).

The motion direction of soft pressurizable actuators is defined by the stiffness of the material: when pressurized, fluid channels and chambers expand towards the less stiff points of the actuator, resulting in bending, twisting or linear motions. The stiffness of the actuator can be adjusted by changing the thickness of the elastomeric material, as shown in [22], where soft pneumatic actuators were used to drive the bending of the fingers of a soft hand exoskeleton. To set the bending angles of the designed actuators, a grooved profile was used at those points corresponding to the finger joints, to reduce the stiffness of the material by reducing the amount of material at those points. Another method to change the stiffness of the actuator is by reinforcing its outer part using additional stiffer layers, which limit longitudinal deformations, and fibers installed following an helical pattern, which limit radial expansion. These actuators are known as soft fiber-reinforced actuators and, by combining different fiber patterns and strain limit layers, they can be mechanically programmed in such a way that one actuator can be divided into multiple segments that perform several combined motions [24, 25].

The soft robotics philosophy is also applied to the design of lower limb exoskeletons, and we can find some examples in the works of Asbeck *et al.* [26, 27, 28, 29], Park *et al.* [30, 31] and Wehner *et al.* [32] (Figure 1.3). As with the reviewed hand devices, soft leg exoskeletons use textiles to transmit the forces generated by the actuation system to the body. In this case where the exoskeletons are used for gait assistance, these clothing-like structures have a substantial impact on the metabolic cost of using the device. The reduction of weight when compared to the rigid structure of a conventional exoskeleton already implies a decrease in the metabolic cost, but additionally, as the inertia in the legs is lowered, the effort required to accelerate and decelerate them is further reduced. Some studies have shown that energy expenditure is increased if the wearer's natural gait pattern is altered [33]. Soft leg exoskeletons mitigate this problem because, as mentioned above, their flexible structure avoids kinematic constraints and joint misalignments [29].

(a) (b) (c)

Figure 1.3: Soft leg exoskeletons: (a) Park *et al.* [31], (b) Wehner *et al.* [32] and (c) Asbeck *et al.* [29] (reproduced with the permission of the authors).

The preferred actuation methods of soft leg exoskeletons are cable-driven and pressurized air systems, as illustrated in Figure 1.3. Similarly to hand exoskeletons, soft leg devices using cable-driven actuation systems, as the one shown in Figure 1.3c, use geared DC motors that are not placed directly over the joint they actuate, but instead are installed separately and connected to the body by means of cables routed inside Bowden sheaths [26, 27, 29]. This configuration leads to an additional reduction of the inertia in the legs.

Those exoskeletons that rely on pressurized air to operate are based on a type of actuator called pneumatic artificial muscle (PAM), also known as a McKibben artificial muscle. These actuators consist of a pneumatic bladder and an external braided fiber mesh that restricts the bladder expansion. When pressurized air is applied, the rubber air chamber expands, generating a contraction or extension movement, depending on the configuration of the actuator. This type of actuator, which is used in the devices depicted in figures 1.3a and 1.3b, is somewhat similar to the soft pressurizable actuators cited above in that its principle of operation is essentially the same and it is also a device that complies with the design principles of soft robotics, being lightweight and intrinsically compliant. However, these actuators are capable of exerting greater forces (¿ 150 N) by working at greater air pressures. The downside of this is that they need more powerful air compressors to operate [27].

1.3 Context

The work presented in this thesis has largely been developed as part of the EU-funded STAMAS (Smart technology for artificial muscle applications in space) project [1], which has been conducted from 2013 to 2016 by a consortium of European research centers. The ultimate goal of this project is to improve human life in space by enhancing the performance of spacesuits and by reducing the negative impact of microgravity on health. To reach this goal, the STAMAS project has focused on the research and development of new bio-inspired actuation systems, based on non-conventional actuation technologies such as SMAs and EAPs, and on their application into biofeedback suits for astronauts that could replace current countermeasure devices. The final outcome of the project has been the construction of a hand and leg biofeedback suit demonstrators in which the developed actuation systems, as well as all the additional systems required for their operation, have been tested.

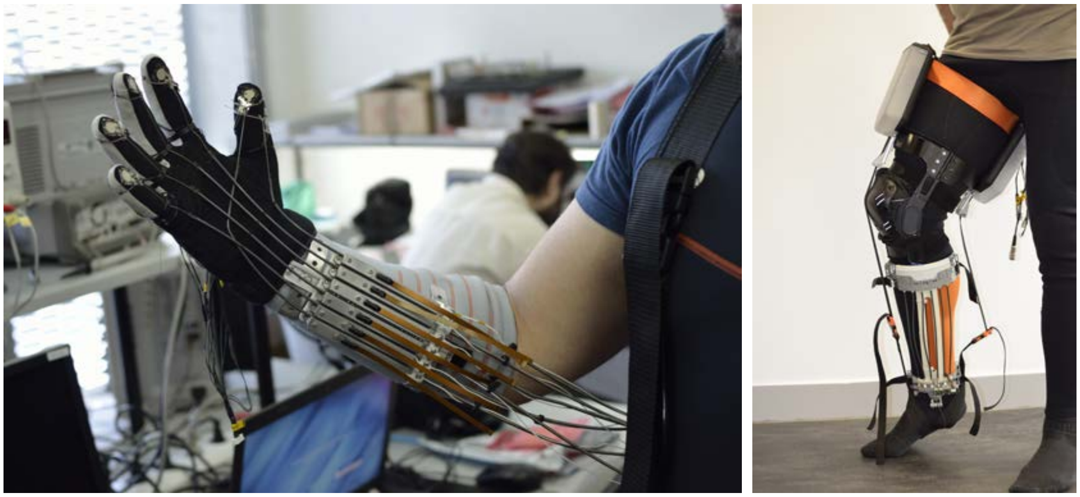

(a) (b)

Figure 1.4: STAMAS demonstrator: (a) hand demonstrator and (b) leg demonstrator.

The lower limb demonstrator (Figure 1.4b) is intended to be used inside a spacecraft as an exercising device, to address the problem of weightlessness that results in a loss of bone density and muscular mass. The leg demonstrator is divided into three different actuating subsystems, each one designed to tackle different pathologies associated with prolonged stays in a microgravity environment (muscle atrophy, bone loss and shifting of blood distribution). The first subsystem uses two SMA-based

---

[1] `www.stamas.eu`

actuators in antagonist configuration, consisting of several wires of this material arranged in parallel, that exert lateral forces on the ankle with the aim of training the user's proprioceptive abilities. The second subsystem uses two variable stiffness SMA-actuators, also in antagonist configuration, that oppose the flexion/extension movement of the wearer's knee. This subsystem is designed to exercise the leg muscles by varying the degree of the opposing force exerted by the actuators, which are spring-like actuators made of pseudoelastic SMA sheets. The last subsystem of the leg demonstrator consist of EAP bands that generate a periodic compression motion around the calves to help blood flow in the lower limbs.

The upper limb demonstrator is a soft hand exoskeleton (Figure 1.4a) designed to mitigate hand fatigue and hand-related injuries, two problems that astronauts suffer during extravehicular activities and which limit the duration of spacewalks. These problems are caused by the force astronauts have to exert when moving their fingers to overcome the opposing force caused by the inner pressure of the spacesuit gloves. The task of the developed hand demonstrator is to overcome the rigidity of the gloves by means of a SMA-based actuation system that operates alongside the wearer, combining its output force with that exerted by the user. By amplifying the astronaut's grasping force, hand fatigue and injuries caused by applying excessive force would be reduced. The hand demonstrator has been designed as a soft exoskeleton due to the constraints imposed by its planned application. By not using a rigid frame, its volume is reduced, allowing for a better integration into a space suit glove. Being flexible, a soft exoskeleton will not make the spacesuit stiffer. Also, the weight of the device is reduced, a very desirable property taking into account the cost per kilogram of payload sent to space. Chapter 6 covers the design and testing of this soft hand exoskeleton, which serves as a use case of the actuator designed in this thesis.

1.4 Thesis objectives

The main objective of this thesis is the design of an actuator that satisfies the characteristics sought in the field of soft wearable robotics, namely: capable of providing high forces, flexible, compact, lightweight and that can be seamlessly integrated into fabrics and clothing. This design will be based on the use of an SMA wire as the transducer of the actuator, as we consider that the properties of this material with this particular form factor are very well suited to attain the aforementioned characteristics.

To realize the proposed objective, this thesis addresses the three main challenges identified above when designing a SMA actuator for soft wearable robots, namely:

1. **Reduced output displacement with respect to the length of the transducer.** Due to the limitations of SMA wires in this aspect, the actuator will

have to use very long wires to provide displacements in the order of several centimeters, but it should not fall into the usual drawbacks of existing designs based on the use of long SMA wires. To comply with the design considerations of soft robotics, the actuator design must be flexible.

2. **Reduced actuation bandwidth.** As the shape memory effect of SMAs is a thermally triggered process, actuators using these materials as transducers can be quite slow, mainly due to the cooling time. The cooling time should be reduce, and this improvement should be done by passive methods. The use of active cooling methods, such as liquid cooling, which increase the volume and weight of the actuator, as well as its power consumption, must be avoided.
3. **Nonlinear behavior.** The control of SMA-based actuators presents presents some challenges due to their thermal hysteresis, distinctive of these materials, which introduces nonlinearities that affect their controllability. In this case, the objective is to develop a control algorithm that is capable of providing a robust and precise control of the designed actuator, but whose computational cost is not too high, as it is intended to be integrated in an embedded system.

In addition to the above, the following developments have been realized:

1. A model of the SMA wire transducer, to better understand and to be able to analyze the different processes that take place during its operation. The purpose of this model is to provide a tool to assist in the development of future actuator designs using this type of transducer, by performing mechanical simulations and testing controllers.
2. As a proof of concept of the work developed on the thesis, the designed actuator and controller have been integrated in a real soft hand exoskeleton. This will demonstrate how both the proposed actuator and its control system can be used in a real device designed according to the soft robotics principles.

1.5 Document Structure

The rest of this thesis is organized as follows:

- Chapter 2 is dedicated to study the physical phenomena that take place during the martensitic transformation responsible of the two distinct properties of shape memory alloys: the shape memory effect and pseudoelasticity. This chapter also reviews the different modeling techniques developed to reproduce the particular behavior of these materials. Finally, an overview of the application of SMAs as an actuation technology is given, including a section with the most relevant control methods applied to overcome the nonlinear response of SMA-based actuators.

- Chapter 3 presents the design of the flexible SMA actuator which is the core of this thesis. In addition to describing the mechanical design of the actuator and analyzing its main features, a series of characterization tests have been performed to study its nominal performance and operational limits. The first actuator designed according to the concepts proposed in this chapter was presented in the Robotics and Autonomous Systems journal [34]. This design was further refined in a subsequent publication in the Humanoids conference [35]. This chapter is the result of the research conducted in those publications.
- Chapter 4 features the development of a thermomechanical model of the SMA wire transducer used in the designed actuator. For its validation, a series of experimental tests have been carried out with a real SMA wire that have been replicated with the model, comparing the data obtained in both cases.
- Chapter 5 discusses the control algorithm developed to deal with the problem of uncontrollabilty due to the nonlinear hysteretic behavior of the material. In addition to the proposed controller, two other controllers have been implemented and a series of validation tests have been performed comparing the performance of the three systems. This chapter is based on the research published on the Sensors and Actuators A: Physical journal [36].
- Chapter 6 presents the integration of the different developments of this thesis in a soft hand exoskeleton that has been designed according the concepts explained in Section 1.2. Its actuation system is based on the flexible SMA actuator developed in Chapter 3 and the device is controlled by the control algorithm proposed in Chapter 5. The contents of this chapter have been published in the Soft Robotics journal [37].
- Chapter 7 summarizes and analyzes all the work done in this thesis. Based on the drawn out conclusions, some possible future developments are proposed to further improve and expand the lines of research proposed in this work.

Chapter 2

Shape memory alloys

Shape memory alloys (SMA) are a group of metallic alloys with two distinct macroscopic properties: the shape memory effect (SME) and pseudoelasticity. The SME is the process by which the material recovers a previously "memorized" shape after being deformed when heated above a specific range of temperatures. Pseudoelasticity, on the other hand, is the phenomenon by which the material can undergo large recoverable deformation strains without suffering a plastic deformation under isothermal conditions. In the next section, we are going to briefly review the history of the discovery of these two properties and some of the alloys that have them, as well as some of the applications in which these materials are used.

The rest of this chapter is organized as follows. Section 2.2 details the chemical and physical processes responsible of the SME, pseudoelasticity, hysteresis and other phenomena observed in SMAs. Section 2.3 reviews the different techniques that exist to model these properties and reproduce the behavior of these alloys, which will provide a theoretical basis for the model developed in Chapter 4. Next, Section 2.4 examines the state of the art and current trends in the design of SMA-based actuators, to identify their strengths as well as the problems that have to be addressed so that they can represent a viable alternative to other conventional actuation systems. Finally, Section 2.5 is focused on the solutions proposed by different authors to tackle one of the main problems of the use of these alloys in the design of actuators: their difficult control resulting from their non-linear behavior arising from the thermal hysteresis of these materials.

2.1 A brief history of shape memory alloys

Research on shape memory alloys traces back to the studies on the martensitic transformation in the early 20th century. Originally, this phenomenon, observed in FeC alloys, was thought to be irreversible until thermally reversible martensite was discovered in CuZn and CuAl alloys by Kurdyumov and Khandros, who proposed the concept of thermoelastic martensitic transformation in 1949 [38]. Before that, Arne Ölander was the first to observe one of the particular properties that characterize SMAs. In a 1932 paper [39], he reported a very elastic, rubber-like behavior in AuCd alloys with a 47.5% cadmium. The property that Ölander was describing was what Rachinger later, in 1958, called super-elasticity (another way of referring to pseudoelasticity) [40]. As for the shape memory effect, Chang and Read published a paper in 1951 [41] describing how a AuCd rod became straight again when heated back to the cubic (austenitic) phase after being permanently deformed in the martensitic phase. A year later, Reynolds and Bever also reported this effect in CuZn alloys [42].

Research into the thermally reversible martensitic transformation continued during the second half of the 20th century, and other alloys such as InTi [43], CuZn

[44, 45], CuAlNi [46] or AuAgCd [47] were found to exhibit the SME and pseudoelasticity. Some of these alloys were even used in a few practical applications, such as the first SME heat engine presented by Read in the 1958 Brussels World Fair [48] or a thermally operated electrical switch, which was the first device using the SME to be patented. However, despite the number of alloys displaying these effects that were being discovered, they never came to constitute a separate research field, in part because their mechanical properties prevented them from being used in engineering applications. This changed in 1961 with the discovery of the SME in NiTi alloys.

As many scientific discoveries, the SME phenomenon was observed in NiTi by accident. In the late 1950s, William J. Buehler and other researchers were studying different alloys to be used in missile heat shielding and, among the different tested materials, NiTi stood out because of its good mechanical properties [49]: considerable ductility at room temperature, good strength, corrosion resistance... One day, while making some NiTi bar samples, Buehler tested the damping capacity of the material by dropping a cold NiTi bar on the floor. This produced a sound similar to the one a lead bar would make. Buehler was worried that there might be microstructural damage, so he proceeded to drop the rest of the samples, some of which were still hot after being removed from the furnace. To his surprise, the hot samples produced a bell-like sound [50]. This difference in the emitted sound depending on the temperature of the alloy suggested that a temperature-induced atomic structural change was occurring. In a later occasion, during a demonstration to other colleagues, Raymond C. Wiley, Buehler's metallurgical assistant, deformed a NiTi strip several times giving it a corrugated shape, to show the ductility of the material. One of the attendants, Dr. Muzzey, took the deformed sample and heated it with a lighter, apparently to test the reported sound difference between phases. Unexpectedly, the NiTi strip reacted to the applied heat by reverting back to its initial straight shape [51]. These findings were reported in a 1965 paper in which it was stated that the transition from room temperature to higher temperatures lowered the damping capacity of the material and was "accompanied by a perfect "memory" [making] it regain the original shape when heated to temperatures above the transition" [52].

The discovery of the SME in this material, called Nitinol after the combination of the names of the elements of the alloy and the acronym of the laboratory where it was developed, the U.S. Naval Ordnance Laboratory (NOL), initiated a research effort by various groups to fully understand the mechanisms behind the observed phenomena. At first, several theories involving different crystallographic processes were proposed, but in the early 1970s the consensus was that the SME in Nitinol was the result of the same crystallographic transformation discovered in AuCd decades earlier. In 1972, NASA published a complete report in which the crystallography, processing techniques, physical, mechanical and chemical properties, and potential applications of Nitinol were detailed [53]. The effects of adding other elements to the alloy composition were also investigated. It was found that adding Co or Fe to the alloy greatly reduced its transformation temperature, which led to the first use of an SMA in a commercial device: a pipe coupler for F-14 aircraft called CryoFit, which is still commercialized [54]. The opposite effect of increasing the transformation temperature of NiTi by adding other elements to the alloy was also investigated, resulting in the development of NiTiNb alloys [55], as well as other high-temperature SMAs such as TiPd, TiPt and TiAu [56]. Research on SMAs, their properties, applications or the effects of alloying different metals, has continued to this day day and has recently lead to the discovery of a new class of Ni-based alloys whose shape memory properties are not triggered by a change of temperature, but by the application of a magnetic field. These magnetic SMAs (MSMAs) operate at higher frequencies than thermal SMAs and generate larger strains but further research has to be done to have more data regarding their operational limits, creep, fatigue... [57, 58].

The development of Nitinol and other NiTi alloys marks the start of the commercial use of SMAs. Unlike previously developed alloys, this new material had the mechanical properties that made it practical in several applications, specially in the medical and engineering fields. Besides the SME and pseudoelasticity, the properties that made NiTI alloys very appealing for their use in the medical field were their biocompatibility, kink and corrosion resistance and MRI compatibility. Existing applications of NiTi SMAs in this field include: orthodontic wires that make use of pseudoelasticity to exert an almost constant force over a wide range of tooth displacement [59, 60]; self expanding stents [61], atrial occlusion devices [62] and thromboectomy devices [63] that are introduced into the body deformed in the martensite phase and transform back to austenite when heated by the temperature of the body, recovering their functional shape by means of the SME; guide wires and catheters that can be easily guided through the human body thanks to the rubber-like behavior of the austenitic phase [64]; orthopedic staples that, like SMA orthodontic wires, apply an almost constant force to reduce the healing time of fractured bones [65] and orthopedic rods that are used to correct scoliosis [66].

As for the existing applications in the engineering field, SMAs are used in civil engineering, aerospace, automotive and even consumer applications, mainly because of their pseudoelastic behavior. SMA elements with different geometrical configurations (rods, springs, beams...) are used as vibration dampers in bridges, buildings, high rise structures... [67, 68, 69] The large hysteresis of the loading-unloading cycle during the pseudoelastic response of SMA elements makes them excellent energy dissipation devices. An interesting application that has been proposed in the field of civil engineering is in self-healing “smart concrete structures” [70]. These are concrete blocks with several embedded SMA wires in the martensitic phase that, upon the appearance of cracks in the structure, would be heated to the austenitic phase.

The phase change would trigger the SME, shortening the wires and thus generating large recovery forces that would close the cracks.

The aerospace industry was the early adopter of SMAs for a commercial use with the aforementioned Cryofit coupler. Since then, other applications have been proposed and developed. The proposed use of SMAs in aerospace structures span from fixed-wings with embedded SMA wires and torque tubes [71], variable geometry airfoils [72], engine inlets or chevrons [73], or adjustable helicopter rotor blades [74]. Because of the great force density of SMAs, these alloys have found some applications in the space industry, where, given of the cost per kilogram put into orbit, weight reduction is of great importance. These applications are mostly limited to non-explosive release devices for satellites [75] or solar sails [76], and damping mechanisms to mitigate vibrations during launch [77]. There are also some examples of SMA-based actuators for space applications such as pseudoelastic hinges for solar arrays [78, 79] or the rotational actuator used in a dust cover of the Mars Pathfinder [80].

SMAs can also be found in some transportation applications, such as the SMA-actuated valve used in the gearbox of the Shinkansen Nozomi-700 bullet train to regulate the oil level inside the gearbox depending on its temperature [81]. SMA devices have also been used in the automobile industry, to control the air intake manifolds of combustion engines [82], to actuate protective lids in the lighting system, adaptive transmissions [83], impact dissipation [84], mirror and seat adjustment [85]...

Besides the aforementioned medical and engineering applications, SMAs are used in a variety of consumer applications such as temperature-operated automatic valves for coffee makers, rice cookers, sprinklers or showers, eyeglass mountings tan can be deformed without breaking or golf clubs with embedded pseudoelastic SMA elements to better absorb the impact of the ball [83]. SMAs in the pseudoelastic regime are also used in electrical cable connectors or embedded antennas that can withstand large deformations.

We have seen how, since the discovery of the SME and pseudoelasticity in AuCd, many different alloys having these properties have been developed, being NiTi-based alloys the ones that are usually used in commercial applications. To design the SMA-based actuator presented in this thesis, a commercially available NiTi alloy called Flexinol [86] has been used. For this reason, unless otherwise specified, all references to SMAs in general will refer to NiTi-based alloys, which are the most commonly used alloys in both research and commercial applications.

2.2 Phenomenology of shape memory alloys

The remarkable properties of SMAs, the SME and pseudoelasticity, are the consequence of a reversible diffusionless transformation from a high temperature parent phase (austenite) to a low temperature product phase (martensite), caused by shear distortion of the lattice structure (movement of atoms from their original position) [83], unlike other material transformations that occur by diffusion of atoms.

The martensitic transformation in SMAs is a thermoelastic process that can be either thermally-induced (SME) or stress-induced (pseudoelasticity). The driving force of this transformation is the difference in Gibbs free energy between the two different crystallographic structures of austenite and martensite (Figure 2.1). When the material is cooled below or heated above a specific temperature at which the free energy of both phases is equal (the equilibrium temperature), the energy difference induces a change of the type, direction and/or lengths of the interatomic bonds, causing an atomic rearrangement in the crystallographic structures [87].

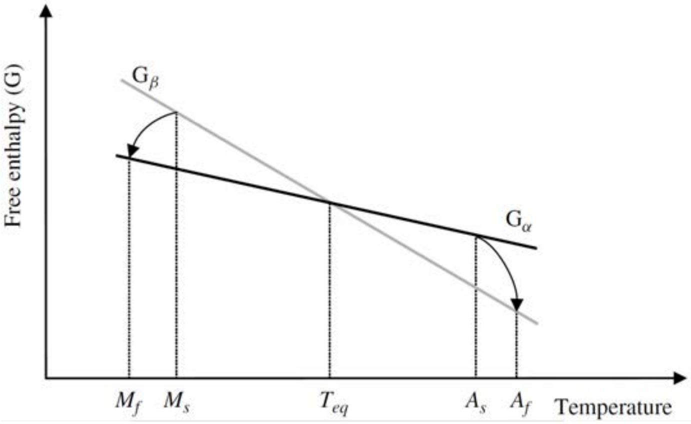

Figure 2.1: Gibbs free enthalpy diagram [10] (reproduced with the permission of the author).

During the austenite to martensite, or forward, transformation, martensite crystals are formed by nucleation and growth within the parent phase [88]. The forward transformation induces an elastic strain around the martensite forming in the austenite phase and, in the absence of an external stress, martensite crystals are self-organized in such a way that the associated elastic strain energy is reduced, in a process known as *self-accommodation*, illustrated in Figure 2.2. The crystals formed by this process are called *variants* and have different crystallographic orientations [83, 89]. The combination of the self-accommodated martensitic variants exists as *twinned* martensite, in which there is no observable macroscopic deformation. If an external stress is applied, the twinned variants are reoriented by *stress-induced accommodation*, causing variants with a particular orientation to expand at the expense of variants with other less favorable orientations. The reoriented martensitic variants form *detwinned* martensite and an observable macroscopic strain of up to 8 % is obtained [83]. When the forward transformation is stress-induced, by applying an external load to the material in the austenite phase at constant temperature, the resulting martensite is directly formed in a detwinned state, with no self-accommodation process taking place.

As for the martensite to austenite, or reverse, transformation, the combination of the elastic energy stored in the material during the forward transformation and the thermal driving force cause the transformation of the detwinned martensitic variants back into austenite [90, 91]. As the austenite crystals are highly symmetrical and form a single variant, the reverse transformation reverts the inelastic strain induced by the applied stress, resulting in the recovery of the macroscopic shape the material had prior to the martensitic transformation.

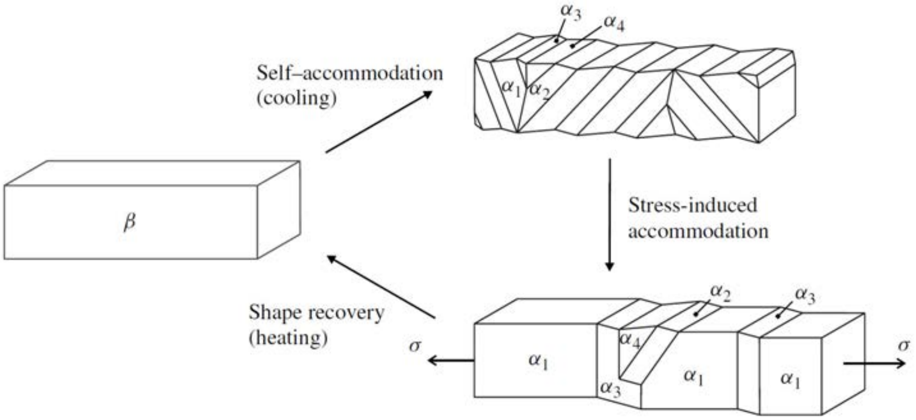

Figure 2.2: Formation of variants by self accommodation and stress induced accommodation, and thermal shape recovery [10] (reproduced with the permission of the author).

The transformation cycle from austenite to martensite and back to austenite has an associated hysteresis (Figure 2.3), which is another characteristic property of SMAs. The temperatures at which an SMA starts and finishes the transformation from the parent to the product phase (M_s and M_f) are different than the ones at which the material starts and finishes the reverse transformation (A_s and A_f). This gives rise to a hysteresis loop in the strain-temperature ($\varepsilon - T$) space in a thermally-induced transformation, as well as in the stress-strain ($\sigma - \varepsilon$) space in a stress-induced transformation. The area enclosed inside the hysteresis loop represents the energy dissipated as internal work in the transformation cycle [83, 90].

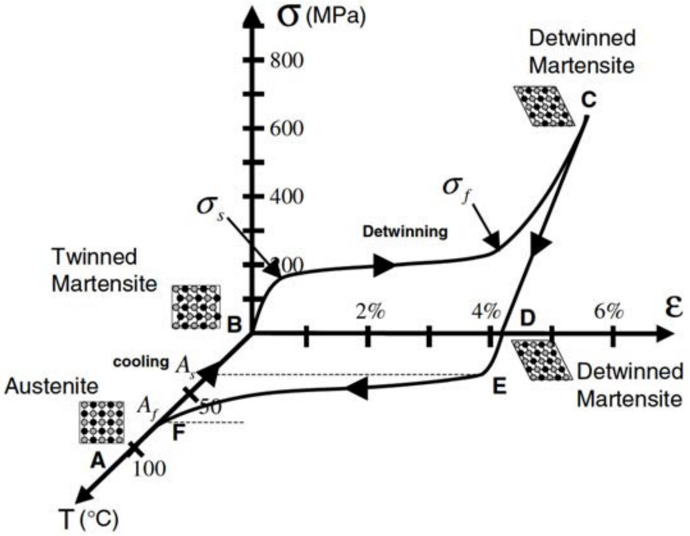

Figure 2.3: Temperature dependent stress-strain hysteresis [83] (reproduced with the permission of the authors).

Internal work arises to overcome the frictional forces resulting from the motion of the austenite-martensite interface. During the forward transformation it is necessary to undercool the material below the equilibrium temperature, because an additional contribution to the free energy change is required to overcome friction resistance. This is also the case for the reverse transformation: although the stored elastic energy is enough to start the transformation to austenite, internal friction ends up opposing interfacial motion, so the material has to be overheated above the equilibrium temperature to provide the required driving force [90]. Although there are other irreversible contributions to the free energy change in the energy balance (the occurrence of transformation induced defects [92] and the atomic rearrangement and volume change associated with the transformation [93]), energy dissipated in the form of work is the main cause of the thermal hysteresis of SMAs [94].

2.3 Shape memory alloy modeling

The complex behavior described above often makes the development of SMA based applications a costly and time-consuming trial and error process. For this reason, a great amount of the literature about SMAs is devoted to modeling the properties and physical processes that we have discussed in the last section.

Having models that can simulate the complex behavior of these materials is of great importance since they allow a better understanding of their operation and can reduce the development time and cost of SMA-based applications, by enabling the study of their behavior under all kinds of conditions without the need to experiment with real devices. For this reason, part of the work done in this thesis has been the development of an SMA wire model, presented in Chapter 4. In this section, we are going to review some of the most relevant works on SMA modeling, to provide the theoretical background from which the proposed model has been built.

Cisse *et al.* [95] propose the following classification of existing SMA models according to the modeling scale and the level of detail in the description of some aspects of the material behavior:

- Microscopic thermodynamic models: these models describe phenomena occurring in the material at a microscopic level, such as phase nucleation, interface motion or martensite twin growth.
- Micro-macro models: so called because they first describe the SMA behavior at a microscopic level by modeling, for instance, the behavior of individual grains, in order to obtain the equations that describe the macroscopic behavior of the material using scale transition techniques.
- Macroscopic models: these models include those based on phenomenological considerations, simplified micro-macro thermodynamics and those resulting from direct experimental data fitting (black box models).

These approaches are further subdivided into several different modeling techniques. Although both microscopic thermodynamic and micro-macro models provide very accurate results and are well founded in terms of physics, they are very complex and computationally expensive [95]. Some phenomenological macroscopic models, on the other hand, incur some simplifications that make them easier to implement and reduce the computational load. Phenomenological models are widely used in engineering applications for this reason, and also because they rely on a set of parameters that can be easily measured. Despite their simplifications, these models provide results in accordance with experimental tests in some cases, such as one-dimensional modeling of SMA wires under axial stress.

2.3.1 Tanaka-type phenomenological models

The most popular one-dimensional phenomenological models are those developed by Tanaka [96], Liang and Rogers [97], Brinson [98], Ivshin and Pence [99] and Boyd and Lagoudas [100], with the former three being the ones from which most of the one-dimensional phenomenological models found in the literature have been developed. These models are also known as assumed phase transformation kinetics models because the constitutive equation that relates stress, strain and temperature, also includes an additional dimensionless state variable ξ that represents the martensite volume fraction (the amount of transformed material). This variable is calculated in a separate equation that represents the evolution (kinetics) of the phase transformation as a function of stress, temperature and, in some cases, the previous values of the martensite fraction itself.

From thermodynamic considerations, by writing the Clausius-Duhem inequality in terms of the Helmholtz form of free energy, Tanaka [96] derived a constitutive equation in the rate form by which the stress rate is expressed as a function of the strain, temperature and martensite fraction rates. This equation has been rewritten by other authors as:

$$\dot{\sigma} = E\dot{\varepsilon} + \Omega\dot{\xi} + \Theta\dot{T} \tag{2.1}$$

where σ, ε, T and ξ are the stress, strain, temperature and martensite fraction of the SMA, respectively. The other material properties are the Young's modulus E, the transformation tensor Ω and the thermoelastic tensor Θ, parameters that Tanaka assumed to be constant. In this model, phase transformation kinetics is characterized as a function of temperature and stress, by means of two exponential equations that correspond to the forward and reverse transformations:

$$\xi_{\mathrm{M-A}} = \exp[A_{\mathrm{a}}(T - A_{\mathrm{s}}) + B_{\mathrm{a}}\sigma] \tag{2.2a}$$

$$\xi_{\mathrm{A-M}} = 1 - \exp[A_{\mathrm{m}}(T - M_{\mathrm{s}}) + B_{\mathrm{m}}\sigma] \tag{2.2b}$$

where A_{a}, A_{m}, B_{a}, and B_{m} are material constants in terms of the transformation temperatures A_{s}, A_{f}, M_{s} and M_{f}.

In their model, Liang and Rogers used the constitutive equation proposed by Tanaka, but opted for a cosine function to model phase transformation kinetics [97]:

$$\xi_{\mathrm{M-A}} = \frac{\xi_{\mathrm{M}}}{2}\cos[a_{\mathrm{A}}(T - A_{\mathrm{s}}) + b_{\mathrm{A}}\sigma] + \frac{\xi_{\mathrm{M}}}{2} \tag{2.3a}$$

$$\xi_{\mathrm{A-M}} = \frac{1 - \xi_{\mathrm{A}}}{2}\cos[a_{\mathrm{M}}(T - M_{\mathrm{f}}) + b_{\mathrm{M}}\sigma] + \frac{1 + \xi_{\mathrm{A}}}{2} \tag{2.3b}$$

where a_{A} and a_{M} are two material constants related to the transformation temperature range, and b_{A} and b_{M} are two material constants that capture the dependence of the transformation temperatures on the applied stress. By including the terms ξ_{M} and ξ_{A}, these two equations also take into account the value of the martensite fraction prior to the transformation process.

While both the Tanaka and the Liang and Rogers models are able to reproduce the pseudoelastic behavior of an SMA wire, according to Brinson [98] they cannot model the SME at temperatures below the martensite start temperature M_s because they only consider the temperature-induced twinned martensite, and not the stress-induced detwinned martensite responsible of the macroscopic deformation observable during the SME. For this reason, Brinson defined the martensite fraction variable as the sum of a temperature-induced part ξ_T and a stress-induced part ξ_S. Moreover, taking into account experimental evidence that shows that the value of the Young's modulus E is different for martensite than for austenite, Brinson defined the elastic modulus as a linear function of the martensite fraction. Also, the transformation tensor Ω is not assumed to be constant, but a function of E. Applying all these changes to the Tanaka's constitutive equation, the general differential form of the constitutive equation of the Brinson model is:

$$\dot{\sigma} = E(\xi)\dot{\varepsilon} + \Omega(\xi)\dot{\xi_S} + \Theta\dot{T} \tag{2.4}$$

Brinson chose the cosine functions proposed by Liang and Rogers to describe phase transformation kinetics, modifying them to accommodate the new definition of the martensite fraction. The stress and temperature conditions for which each of these equations is applicable were also modified, dividing the forward transformation process into two expressions, to take into account the twinned and detwinned martensite.

2.3.2 Hysteresis models

In addition to the described piecewise exponential and cosine functions, there is a great number of publications devoted to hysteresis modeling that describe other methods that can be applied to the modeling of phase transformation kinetics in a phenomenological model. For example, Ivshin and Pence [99] coupled a Tanaka-type constitutive model with a Duhem differential model for the phase transformation kinetics. Visintin [101] and Bo and Lagoudas [102] provide a detailed overview of the existing models of hysteresis. Essentially, the different modeling techniques described by these authors can be divided in two categories: differential models and models based on hysteresis operators. To these, a third category should be added to include more recent works on black box models.

Differential models

This group includes those models that reproduce the hysteretic behavior of a system by means of a differential equation, such as the Duhem model [103, 104] and the Bouc-Wen model [105, 106].

The basic assumption of the Duhem model is that the output changes its characteristics with a change of the direction of the input. This is expressed mathematically as follows:

$$\begin{cases} \dot{w} = g_+(u(t), w(t))(\dot{u})^+ - g_-(u(t), w(t))(\dot{u})^- \\ w(0) = w_0 \end{cases} \tag{2.5}$$

where $u(t)$ is the input, $w(t)$ is the hysteresis output and w_0 is the initial value of the hysteresis output. The shape of the hysteresis loop is defined by the slope functions g_+ and g_-, where the subscripts $+$ and $-$ indicate the increasing and decreasing curve, respectively. Finally, $(\dot{u})^\pm$ is defined as:

$$(\dot{u})^\pm = \frac{|\dot{u}| \pm (\dot{u})}{2} \tag{2.6}$$

In the case of SMA hysteresis modeling, g_+ and g_- can be any continuous function that is capable of describing the saturated hysteresis that occurs when the transformation finish temperatures are exceeded. For example, in [107, 108] the authors use Gaussian probability distribution functions as slope functions, while in [109], a combination of two modified Gaussian membership functions is used.

Likhachev and Koval proposed in a series of articles [110, 111, 112] a Duhem-type model that, by introducing scaling coefficients that depend on the equations that define the main hysteresis loop, is able to represent the minor hysteresis loops observable in partial phase transformations of SMAs.

As for the Bouc-Wen model, it has been widely used to model all kinds of components and devices that show hysteretic behavior, although it has barely been used to model SMAs. In the Bouc-Wen model, the relationship between the input displacement and the output restoring force in the equation of motion of a single-degree-of-freedom system is defined by a first-order non-linear differential equation in a hysteretic way. By adjusting a set of parameters, the model can be fitted to a wide range of real hysteretic responses.

Models based on hysteresis operators

The underlying idea of models based on hysteresis operators is that the main hysteresis loop and the minor loops are a combination of infinite simple hysteresis relays, each of which is represented mathematically by a hysteresis operator. The Preisach [113], Krasnosel'skii-Pokrovskii [114] and Prandtl-Ishlinskii [115, 116] models belong to this category.

In the former, hysteresis is computed as a weighted summation of n two-valued relay operators connected in parallel. The higher the number of operators, the more precise the model will be, at the expense of a higher computational cost.

The Krasnosel'skii-Pokrovskii model is a formulation of the Preisach model that introduces a generalized hysteresis operator in which different continuous functions can be used, avoiding the jump discontinuities that exist in the Preisach operator. Among its advantages, this operator is able to represent minor hysteresis loops.

Finally, the Prandtl-Ishlinskii model is also a Preisach-type model that represents the hysteresis loop as a superposition of two different operators, which are parameterized with a simple threshold variable. The generalized form of the Prandtl-Ishlinskii model replaces the threshold value by two envelope functions, which determine the shape of the hysteresis loop and allow the saturation phenomenon to be included in the model. Although it is easy to implement, the Prandtl-Ishlinskii model cannot reliably model minor hysteresis loops [117].

One of the common disadvantages of models based on hysteresis operators is that they depend on a set of parameters that have to be estimated, which makes their implementation more complex and time-consuming. In addition, it makes the model very dependent on the conditions under which the identification is carried out. Several system identification techniques can be used to perform this estimation, such as least mean squares, recursive least squares, genetic algorithms or neural networks.

Black box models

Black box models are widely used to model different kinds of nonlinear systems, including systems with hysteresis. Their operation is based on the identification of the system to be modeled: from a series of inputs given to the real system and its corresponding outputs, a predictive mathematical model capable of replicating the behavior of the system is constructed. Likewise to hysteresis operator models, the resulting model is highly dependent on the conditions under which the identification is performed.

Among the different types of existing black box models, some have been applied to SMA modeling, such as the Hammerstein-Wiener model [34] or neural networks [118]. Usually, these models are used in control applications, including the model in the controller as a feedforward term or, as in the case of [119], to implement a sensorless controller that uses the model to estimate the value of the controlled variable.

2.4 Shape memory alloy-based actuators for mechatronics

In Section 2.1, some of the applications of SMAs in different fields have been briefly reviewed, listing several commercial uses of the SME and pseudoelasticity. These two properties, along with the other features of these alloys, render SMAs a very attractive material with potential applications in many other fields. This interest is reflected in a multitude of theoretical studies and experimental prototypes but, either because of a lack of further development or because some of the inherent limitations of these alloys have yet to be overcome, there has not been a transfer of these purely research applications to a commercial use. One of these areas in which SMAs have a great application potential but have not yet made the transition to a commercial use, except in some marginal cases, is the design of actuators for mechatronic devices.

2.4.1 Available transduction methods

Generally speaking, an actuator is a device that transforms energy into motion/force. More specifically, an actuator changes the mechanical state of a system (the energy level it has at a given moment) by converting an input energy (usually electrical, but it also can be pneumatic, magnetic, thermal...) into mechanical energy, to either dissipate or increase the energy level of the system [10]. According to Busch-Vishniac [120], the energy conversion can be between different energy domains, such as magnetic to mechanical energy, or between different energy types belonging to the same domain, as is the case of rotational to translational energy conversion. In an actuator, the element that performs this energy conversion is the transducer.

Although the transduction process can be either between any two different energy domains or within the same domain, the vast majority of actuators take an electrical input and produce a mechanical output. According to Pons [10], using electrical energy as the input of an actuator has some advantages in terms of compatibility with the energy domain of the rest of the system where the actuator is installed, faster operation and availability and simplicity of the electronic components used in the control and conditioning systems. Even though there are transducers that cannot make this conversion directly, the actuator may include more than one transducing material, or several transduction processes may take place within the same material, resulting in an energy flow between an electrical input and a mechanical output. The latter is the case for electrically driven SMA-based actuators.

An SMA actuator uses an SMA element as the transducing material and, depending on the domain of the input energy, is based on one of the following transduction phenomena:

- **Thermomechanical transduction.**

  In this case, the SMA transducer is directly exploiting the thermally triggered SME. The input thermal energy induces the martensitic transformation, and the resulting transformation strain produces mechanical work.

  This heat can be transferred by conduction from an external source, e.g. hot air or a liquid flowing around the material [121]. However, this technique has the drawback of requiring additional hardware (pumps, valves...) that increases the weight, volume and overall complexity of the actuator, nullifying all the advantages of SMAs over other actuation technologies.

Other possible external heat sources are resistive heaters or Peltier cells in contact with the SMA element. There are flexible film resistive heaters that can adhere to a surface, making them an interesting option to heat any SMA element with a relatively large surface area, like SMA ribbons. However, in the case of SMA wires, this is an impractical method due to their small surface area compared to the minimum area that these heaters usually have.

- **Electromechanical transduction.**

  If an electric current is passed through an SMA element, preferably a wire, two transduction processes take place. First, electrical energy is transformed into thermal energy thanks to the Joule effect, the process by which an electrically conducting material is heated by an electric current flowing through it. This thermal energy triggers the shape recovery process of the SMA element and the resulting recovery energy is transformed into mechanical work. In an SMA wire, the input electrical current can be directly provided by a current source, or can be the product of applying a differential voltage between both ends of the wire.

  Another approach to trigger the SME that belongs to this transduction category is inductive heating, a non-contact method that, ultimately, also heats an electrically conductive material by means of the Joule effect. In this case, the currents that produce Joule heating are the so-called eddy currents: closed loops of current flowing inside the SMA, produced by a rapidly alternating magnetic field applied by a solenoid surrounding the transducer. According to some authors [10], when using inductive heating some parts of the material heat more than others. This causes an uneven transformation of the SMA, generating internal stresses that lead to microscopic internal damage which, in the end, shortens the service life of the actuator.

- **Magnetomechanical transduction.**

  There are a special type of SMAs in which the martensitic transformation is not triggered by a change of temperature but by a magnetic field [10]. In this case, when the SMA specimen is in the martensite phase, the application of a magnetic field perpendicular to the magnetically active axis of the crystallographic lattice makes other twin variants to appear and grow, changing the length of the specimen.

2.4.2 Advantages and disadvantages of SMAs in the design of actuators

Why are SMAs so appealing when compared to other conventional actuation technologies such as electromagnetic motors, hydraulic or pneumatic actuators? Technological development and research in new types of materials and manufacturing methods have led to the appearance of increasingly smaller sensors, embedded control systems, lighter and stronger structures, better energy sources... Some fields of mechatronics where miniaturization and weight reduction are of great importance, such as soft wearable robotics, have been benefited from these technological advances, resulting in the development of lighter, smaller and thus, more portable devices. However, actuators, which are a key element of a mechatronic device, have not undergone similar development. Power delivery is one of the most important parameters of an actuator, and the cost of miniaturizing devices based on conventional actuation technologies is an important reduction in the power they can deliver. Precisely SMAs, thanks to their high force density, are not affected by this factor, enabling the design of very compact actuators capable of producing forces comparable to those generated by much larger and heavier devices.

Several authors have identified some of the properties of SMAs as very beneficial when designing new actuators based on these materials. The main one is the aforementioned high force density, which greatly surpasses that of pneumatic and hydraulic actuators and is the highest among most emerging technologies such as piezoelectric actuators, electroactive polymers or magnetostrictive devices [10]. To put this in perspective, a Nitinol wire with a diameter of 0.5 mm is able to deliver nominal forces of up to 35 N [86]. The consequence of this is that really small actuators can be designed and, due to the ratio between delivered force and transducer volume, they can be very light. In addition to these properties, their operation is silent, a feature that, in the case of wearable robots, helps improve user acceptance. Finally, depending on the form factor and configuration, their behavior is biomimetic, a feature that leads to the design of muscle-like actuators or bioinspired robots, as we will see below.

On the other hand, the negative aspects of SMAs should also be highlighted. Due to the rate of cooling until completion of the austenite to martensite phase transformation, the actuation bandwidth of SMA-based actuators is usually slow. As the size of the transducer is reduced, and therefore the ratio between its mass and its surface is increased, the cooling speed is increased. According to Pons, this increment can be by a factor of 100 if the scale is reduced by a factor of 10 [10]. However, reducing the scale of the transducer also reduces the force it is capable of delivering, so when designing an actuator based on these alloys, a trade-off must be found between the two factors.

Another important consideration for SMA-based actuators is their difficulty of control. The thermal hysteresis we have discussed in Section 2.2 makes the behavior of the system to be nonlinear. This causes the most common linear control techniques, such as proportional-integral-derivative (PID) controllers, to induce steady state errors, limit cycles and overshooting and undershooting when heating and cooling, respectively.

Finally, another constrain of SMAs when designing an actuator that has to provide a high output displacement is their maximum attainable strain, which in the case of an SMA wire is an 8% of its total length. The displacement can be greatly increased when the SMA transducer is a spring but, in this case, the provided force is too low, so this type of form factor is often relegated to passive applications [10].

2.4.3 Overview of existing SMA-based actuators

We can find some examples in the literature in which the authors address the problem of the limited strain of SMA wires. The most common approach is to use a very long wire and route it back-and-forth in a system of pulleys in such a way that the length of the SMA is enclosed in a compact package. Pittaccio *et al.* have adopted this solution in the design of the actuator for an ankle orthosis presented in [122]. Its actuator consists of a 250 cm long SMA wire, routed around a total of 10 pulleys so that it can be installed inside a 150 mm long housing. To recover the initial length of the SMA during its cooling phase, the wire is connected to a pseudoelastic spring. With this configuration, the actuator provides a maximum linear displacement of 8 cm (more than 50 % of its total length) and a peak force of 8.83 N.

This same approach has been adopted by Andrianesis *et al.* in the designed of their proposed SMA actuator for robotic hands [123, 124]. In this case, a long SMA wire has been folded forming two N-shaped parallel branches (Figure 2.4a) so that it operates as if it were two wires with half the length but which, being mechanically connected in parallel, generate double the force. This arrangement has been enclosed in a 147 mm long actuator which provides a maximum force of 18 N and a maximum linear displacement of 15 mm, which is more than a 10 % of the total length of the device.

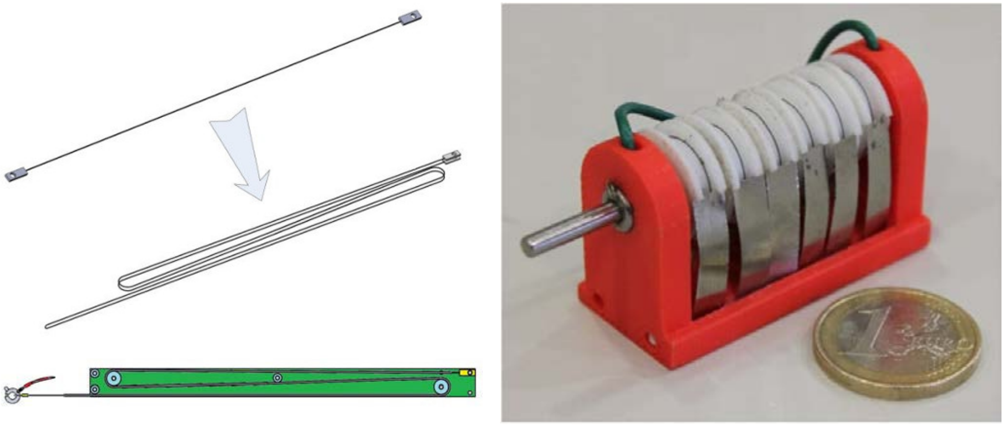

(a) (b)

Figure 2.4: Examples SMA-based actuators: (a) folded SMA actuator [124], (b) Continuous rotary SMA minimotor [125] (reproduced with the permission of the authors).

A design concept similar to the above is proposed by Song [126]. In this work, the designed device is a rotary actuator that uses a 74 cm long SMA wire wrapped around a 3 cm diameter cylinder that acts as the actuator rotor. By fixing one end of the SMA wire to the actuator housing and the other end to the rotor, the contraction of the former generates a rotary movement of the latter. A torsion spring connected to the output of the rotor causes the actuator to return to its initial position during the cooling phase of the SMA wire. With this configuration, the actuator generates a maximum angular output of 100 degrees and a torque of 0.26 Nm.

Mammano and Dragoni propose a similar rotary actuator [125]. Like the actuator proposed by Song, this device uses the principle of winding a long SMA wire around a cylinder to generate a large rotational movement from the wire contraction. The actuator has been engineered in such a way that it is capable of generating a continuous rotational motion by means of a set of six cylinders, or drums, each with its own SMA wire, and a clutch that couples their motion to the output shaft (Figure 2.4b). To generate a continuous rotational motion, the drums are activated sequentially. When the first drum reaches its rotational limit of 15 degrees, the second drum is coupled to the output shaft of the actuator and its corresponding SMA wire is activated, continuing the movement. Simultaneously, the first drum is decoupled and its SMA wire is deactivated to allow it to cool down and return to its initial position by means of a spring. Once all six drums have been activated, this sequence is restarted. With this innovative mechanism, the authors have managed to design a really compact actuator, 48x22x30 mm, which generates a maximum output torque of 20 Nmm and a free continuous speed of 4.4 rpm.

Although the above solutions do allow reducing the size of an SMA actuator that uses a long wire to produce high displacements, at the same time entails the emergence of other problems. Naturally, the longer the SMA wire, the more pulleys will be needed to keep its size confined in a compact housing. This increases both the mechanical complexity of the actuator, increasing the risk of failure, and decreases its performance due to frictional losses. Another consideration is that the heat of the wire is transferred by conduction at the points of contact with the pulleys. This means that the wire is not evenly heated, resulting in the presence of adjacent areas of the material whose martensite fraction differs significantly, causing internal stresses that eventually lead to wire breakage.

The miniaturization possibilities and the ductile nature of SMAs have led some authors to consider their use in the field of soft robotics. For example, in [127], a linear flexible actuator using SMA springs is presented (Figure 2.5a). The actuator comprises two SMA springs inside a bellow-shaped soft silicone body. The springs are activated by the application of electric current and a piano wire bias spring applies the resetting force to return the SMA springs to their initial length after heating. The actuator provides a maximum output displacement of about 16 mm and a maximum output force of 6.5 N.

A bending soft actuator for a robotic hand is proposed in [128, 129]. The actuator consists of an SMA strip with a curved memorized shape embedded inside a silicone rubber cover. Due to the low resistance of the SMA strip, a large current has to be applied to trigger the SME. To avoid this caveat, the actuator has been heated by an indirect method, wrapping Ni-Cr wires around the SMA strip. These wires are then heated by applying electrical current, and the generated heat is transmitted by conduction to the SMA element. According to the authors, energy efficiency is increased from 6.25 % in the case of direct heating to 95.59 % in the case of indirect heating. The robotic hand designed to use these actuators (Figure 2.5b) weighs only 250 g and is able to exert a pinch force of 3 N and a grip force of 9.7 N.

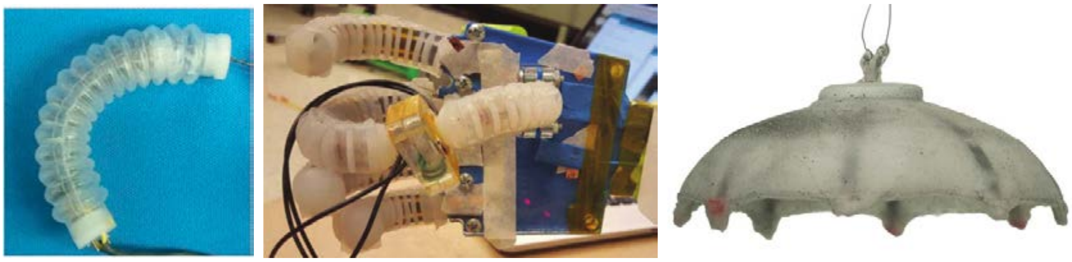

(a) (b) (c)

Figure 2.5: Examples of the use of SMAs in soft robotics: (a) linear flexible actuator [127], (b) robotic hand with soft bending actuators [128] and (c) robotic jellyfish [130] (reproduced with the permission of the authors).

In the field of soft robotics it is rather common to design SMA actuators by embedding components of this material in polymeric composites. The robotic jellyfish presented developed in [130] uses SMA composite actuators to propel itself. These bio-inspired actuators are formed by SMA wires installed longitudinally on steel strips. When the wires contract, the steel strips are bent, and during the cooling phase the strips pull the wires to their original length, thereby generating the undulatory propulsion movement of the jellyfish. The actuators are built into the body of the robotic jellyfish, made of silicone, which weights 242 g and has a diameter of 164 mm (Figure 2.5c). The thrust generated by the actuators has a proficiency of 0.19 s^{-1}, very similar to the 0.25 s^{-1} of a real jellyfish.

There are more examples of the use of SMA elements embedded inside soft structures, such as the robotic starfish designed by Mao *et al.* [131], the robotic inchworm by Wang *et al.* [132], the bend-twist actuators developed by Ahn *et al.* [133] for a robotic turtle [134], the twisting actuator proposed by Rodrigue *et al.* [135, 136, 137], which can reach actuation frequencies of up to 35 Hz, or the self-deployable structure designed by Wang *et al.* [138].

2.5 Control of SMA-based actuators

In Section 2.2 we have seen that one of the defining properties of SMAs is their thermal hysteresis caused by internal dissipative processes. While hysteresis is a desirable property in some SMA applications, mostly passive applications that make use of the pseudoelasticity of the material (such as vibration damping [75] or pipe coupling [139]), it has a negative impact on active applications in which the SME is exploited and the macroscopic strain or the force generated by the SMA element has to be precisely controlled. In this case, the hysteretic behavior of SMAs introduces nonlinearities that affect their controllability.

This well known problem, often cited as one of the main drawbacks when designing SMA-based actuators, has led to a thorough study of possible techniques to control the position and force SMA actuators. As stated before, the nonlinear behavior of SMAs implies that linear control methods, such as PID controllers, do not produce optimal results since they originate steady-state errors, limit cycle problems and overshooting upon heating and undershooting during cooling due to the nonlinear saturated hysteretic behavior of SMAs [10, 140, 141]. On the other hand, many different strategies can be applied to control nonlinear systems, but not all of them are appropriate for systems with hysteresis. In this section, some of the most relevant control strategies proposed by different authors to improve the controllability of SMA actuators are reviewed, to provide the theoretical background for Chapter 5, where the control algorithm proposed in this thesis to overcome this problem is presented.

2.5.1 Linear control

Several authors have demonstrated the controllability problems of using simple linear controllers. In [142], a proportional controller is used in active shape control of a flexible SMA beam. Experimental data show that a high gain is required to eliminate the steady-state error, but at the cost of a higher overshoot and actuator saturation. On the other hand, the results obtained by Asua *et al.* in [143] let them conclude that the best type of position controller for their SMA actuators is a PI with anti-windup.

In Yang *et al.* [144], a first-order system is used to model the step response of a composite beam with SMA actuators located on its surface. The parameters are experimentally determined and the model is used to tune a controller. To control the response of the hybrid composite beam, two methods are used. One of them is a conventional PID feedback controller and the other one is a feedforward controller. The experimental results have shown a reasonable settling time and high overshoot for the PID controller, and long settling time for the feedforward controller.

Popov *et al.* [145] have used two PID controllers to control an SMA actuator. The first one is a conventional PID whose gains are adjusted with Ziegler-Nichols. In the second one, which is called Internal Model Control (IMC), the SMA is modeled as successive series of four transfer functions: a gain, a first order transfer function, a second order transfer function, and a dead time. Results show that the time response of the IMC controller is significantly better than the conventional PID.

A particular case of linear controllers that have been successfully applied to SMA actuators are the Pulse Width Modulation (PWM) controllers. This type of controller differs in how the control action that commands the actuator is generated: they use discrete-time PWM signals as control actions. Therefore, this approach can be combined with linear on nonlinear compensators. In Joule heating actuation of SMA actuators, PWM controllers have shown to be an effective solution that reduces their energy consumption, improving their efficiency but reducing their response time. In [146], a PWM controller is used to control an SMA actuator and results show a 30 % reduction in the energy consumed when compared with a conventional PD controller, while maintaining the same position accuracy. An improved PWM technique called Pulse-Width-Pulse-Frequency (PWPF) modulator is used in [147] to modulate a PD controller, achieving a 50% reduction of the energy consumption with respect to the regular PD controller without modulation.

2.5.2 Nonlinear control

In recent years, experimental results using nonlinear controllers to control the position of SMA actuators show that it is possible to achieve faster tracking and greater accuracy than with linear techniques. Shameli *et al.* [148] have used a nonlinear variation of a PID controller referred to as PID-P^3 controller. Their simulations show that for large values of error, the cubic term of the regulator, which is the main difference with respect to a traditional controller, produces great control effort that reduces significantly the settling time. The cubic term vanishes for small values of error and the controller works as a conventional PID controller. This technique has not been validated experimentally.

Gain scheduling is another nonlinear control technique that has been used to control SMAs. Gain scheduling is based on the use of a series of linear controllers whose performance is optimized for different operating points of the plant to be controlled. To switch between the different linear controllers, the gain scheduler monitors one or more observable variables to infer in which operating range is the controlled process. There are some examples of gain scheduling control applied to control the position of SMA actuators, such as the works by Jayender *et al.* [149, 150] or Kilicarslan *et al.* [151]. Andrianesis *et al.* implemented a gain-scheduled controller to drive the output of the SMA actuation system of a robotic prosthetic hand [123].

Lee and Lee proposed the application of a time delay controller (TDC) to control the output angle of a rotary SMA actuator [140]. A model based on the constitutive equation of Tanaka and the kinematic model of Liang and Rogers was developed to tune the proposed model, but maybe this does not really matters. The authors identified the SMA actuator as a combination of a second order nonlinear system representing the dynamics relating the temperature of the transducer and the output angle and a first order equation relating the input voltage with the temperature. A main controller, the proposed TDC, is in charge of generating the desired temperature command, while a saturation plus anti-windup scheme converts this temperature to voltage in a magical and undefined way.

Gédouin *et al.* compare the performance of a linear PI controller with a nonlinear control method called model-free control (MFC) [152]. This technique relies on a purely numerical model that does not take into account any physical considerations regarding the plant to be controlled. The numerical model is defined by a few parameters which are estimated online from the input-output behavior of the system during operation. The numerical, or "local", model is valid only for a small time span, and it is continuously updated at each sample time to construct a feedback control law that adapts to the evolution of the plant [153]. Although in the conducted experiments the MFC controller outperforms the PI controller, the performance of the former is worst than expected by the authors. Better results are obtained in a second set of experiments, when an additional position-dependent gain is introduced in both the PI and MFC controllers. In part, these better results are due to the position references used by the authors. Instead of using step references with an immediate setpoint jump as in the first set of experiments, they used "smoothed"" trajectories generated with a polynomial with zero speed and acceleration at the starting and ending points, and a 10 s transfer time between setpoints, which obviously reduces overshoot and causes the controllers to perform better.

2.5.3 Model-based controllers

This type of controllers are based in constructing a model of the transducer or the complete actuator with one of the different modeling techniques reviewed in Section 2.3. The resulting model can then be used in simulations to design and tune the controller, or it can be integrated into the controller, usually as an inverse model.

The most typical configuration is a combination of feedforward and feedback controllers [154, 155, 156, 157, 158]. The main idea of feedforward controllers consists of using an inverse model of the system to generate the appropriate control input to obtain the desired response. According to Pons [10], model-based feedforward control techniques barely improve the performance obtained with classic feedback strategies due to the dependence of models on the external ambient conditions and the actuated load.

Asrafiuon and Jala [159] have used a model-based sliding mode control law with SMA actuators. Their model is obtained by combining the motion equation with the heat convection (constitutive law) and phase transformation (hysteresis) equations of the SMA. The resulting controller is used in a three-link planar robot for position control.

Elahinia and Ahmadian [160, 161, 162] have developed a nonlinear model of a 1-DOF rotary arm that is actuated by an SMA. The nonlinear approach uses three models: the arm nonlinear dynamic model, an SMA phase transformation model and a nonlinear heat convection model. The authors use two controller designs: a temperature-based controller and a stress-based controller. The temperature-based controller is a variable structure controller while the stress-based one is a sliding mode controller.

A special instance of SMA model-based controllers are the so-called self-sensing controllers. This technique relies on inferring the position of an SMA element from the change in its electrical resistance by modeling the relationship between these two variables. This information is used in the feedback loop of a controller, so that the use of a physical position sensor is not necessary. Therefore, to implement this type of controllers it is necessary to develop an inverse model of the resistance of the material which, once integrated in the controller feedback loop, will take the electrical resistance value measured in the real SMA element as input and will produce a displacement estimation as the feedback signal. The inverse model can be obtained from system identification techniques [163], polynomial curve fitting [164, 165] or differential models [108, 109], among other modeling techniques.

Finally, those techniques reviewed in Section 2.3.2, such as models based on hysteresis operators or black box models, are also widely used in the implementation of model-based SMA controllers. In this case, the premise is to develop an inverse hysteresis model that can be used as a feedforward compensator.The hysteresis model is built based on the experimental data of the system, trying to minimize the error between the real system and the model. The inverse model is then implemented in an open loop controller to adjust the actuator input to compensate the hysteresis of the system. This arrangement produces a linear relationship between the reference input and the system output [166]. In practice, the inverse model cannot cancel completely all hysteresis nonlinearities in SMA actuators, and some authors use a feedback controller together with the feedforward open loop controller [158]. The use of a feedforward controller can speed up the controlled system response and increase the bandwidth when compared with a PID controller. On the other hand, the PID controller provides better tracking performance at low frequencies [167].

In Ahn and Kha [168], the inverted numerical Preisach model is built into a closed loop PID control system to compensate the hysteresis in SMA actuators. Majima *et al.* [154] have developed a control system composed of two control loops: a PID feedback control loop and a feedforward loop. The feedforward loop is used to obtain the required control input corresponding to the commanded displacement. The feedforward control signal is obtained from a Preisach hysteresis model. Another example of the Preisach inverse model used to control an SMA actuator can be found in the work of Hughes and Wen [169].

Hysteresis compensation based on the Krasnosel'skii-Pokrovskii hysteresis inverse model has been proposed by Webb *et al.* [170]. The authors use an adaptive hysteresis model based on a linearly parameterized version of the Krasnosel'skii-Pokrovskii model to compensate the hysteresis effects. They have implemented a temperature control law (with electrical current as input) and an offline-identified model that is used as a fixed compensator.

According to Sayyaadi and Zakerzadeh [141], obtaining the inverse of some of the models based on hysteresis operators, such as the Preisach model, is a complex task. On the other hand, the inverse of generalized Prandtl–Ishlinskii model can be obtained by analytical methods, so that it can be easily used to compensate the nonlinear effects induced by the thermal hysteresis of SMA actuators by using it as a feedforward controller. In the cited work, the authors have implemented a feedforward–feedback controller to control the deflection of a flexible beam actuated by an SMA wire. The controller feedforward compensator is based on the aforementioned generalized Prandtl–Ishlinskii inverse model. A linear PI feedback controller is used in conjunction with the feedforward compensator to eliminate the steady state errors and increase the actuator position control.

As for black box models, Asua *et al.* [118, 143], have used an experimentally trained neural network to cancel the nonlinearities of an SMA wire. The neural network is trained to learn the inverse hysteresis behavior and, after that, an anti-windup PI control loop is used. Kumagi *et al.* [156] have proposed a controller with a feedforward block that uses a neuro-fuzzy inference system together with a PD controller. Song *et al.* [155] have designed a neural network feedforward controller for open loop tracking control of an SMA wire actuator without a position sensor. Their neural network controller is an inverse model of the hysteresis that maps the relationship between the applied voltage and the actuator displacement. In Rezaeeian *et al.* [157], an ANFIS inverse controller applied as a feedforward regulator for force control applications of SMA actuators is proposed.

Chapter 3

Flexible SMA actuator

In Chapter 1, we have briefly reviewed the main trends in the design of soft wearable robots and their actuation systems, examining their strengths and weaknesses. Taking into account the desirable characteristics that the actuators used in this type of devices should have, we have concluded that SMA-based actuators offer a number of advantageous features that make them a viable alternative to the most popular actuation technologies used in this field, provided that their limitations in terms of actuation bandwidth, total transducer length and nonlinear behavior are addressed. To gain a better insight of how SMAs behave and how their particular properties can be exploited and their drawbacks mitigated, an exhaustive analysis of their underlying working principles and its application as transducers in actuator design has been given in Chapter 2.

This chapter discusses the design of the SMA-based linear actuator that is the core of this thesis, covering its mechanical design, power and control electronics and characterization tests. The proposed actuator uses an SMA wire as its transducer and is conceived to take advantage of those properties of this material that can be exploited in the field of soft robotics, such as its actuation force, weight, volume and form factor. The presented design also tackles two of the main limitations of SMA-based linear actuators: the low output displacement with respect to the length of the SMA transducer and the low actuation bandwidth. As will be detailed below, the design of the actuator implements a practical and mechanically efficient solution to the need of using a very long SMA wire to produce displacements in the order of centimeters. Moreover, heat rejection is increased with a passive method, improving the actuation bandwidth without the need of using active cooling techniques.

The rest of the chapter is organized as follows. The proposed mechanical design of the SMA actuator is described in Section 3.1. The details of the design of the power and control electronic subsystems required to operate the actuator are given in Section 3.2. The characterization of the actuator is detailed in Section 3.3, including the description of the test bench used to perform the characterization tests and the analysis of the obtained results. Finally, the most relevant conclusions are summarized in Section 3.4.

3.1 Mechanical design

In Chapter 2 we have seen how using an SMA wire in tensile deformation as the transducer for a linear actuator is the most optimal configuration in terms of produced force and actuator efficiency, but the achievable output displacement is very low, with a maximum recoverable strain of up to 8-10 % of its length. To prevent structural damage and extend the service life of the transducer, the contraction of SMA wires is typically limited to 3-4 %, which implies the use of wires 25 times longer than the desired output displacement of the actuator. Although the actuation displacement can be increased up to 200-1000 % with respect to that of a straight SMA wire by using it in the form of a spring [171], we have seen how this configuration results in a very limited force generation.

In those applications where large displacements and forces are required, such as in the actuation systems of wearable robots, the common approach is to use a long wire routed back-and-forth through a pulley array, as Figure 3.1 illustrates. We have seen some examples of this type of actuators in Chapter 2, such as the works by Andrianesis *et al.* [123, 124] and Pittaccio *et al.*[122]. The drawback of this solution is that as the length of the wire increases, more pulleys are needed to keep the actuator compact, increasing the complexity and weight of the actuator as well as its frictional losses and fatigue [172]. In the specific case of soft wearable robots, there is an additional drawback: to hold the pulleys in place, a rigid structure is needed, which does not meet the design constraints of soft robotics and makes it difficult to integrate the actuator into the rest of the structure of the device.

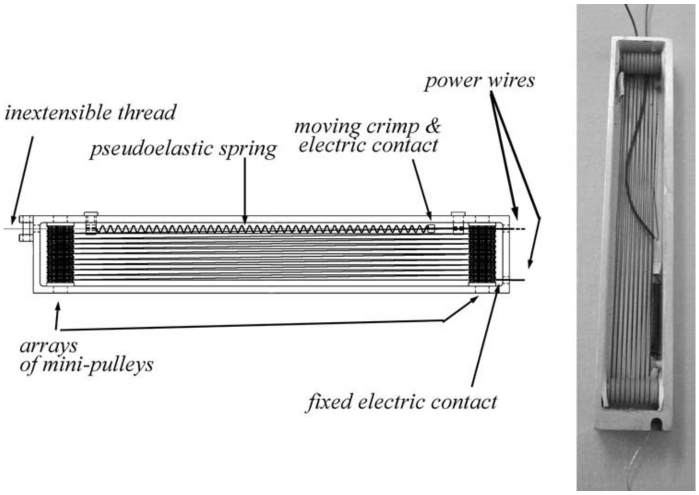

Figure 3.1: An example of a “pulley array” SMA-based actuator [122] (reproduced with the permission of the authors).

The premise of the design proposed in this thesis is that, in the case of soft wearable robots, the use of long SMA wires is not necessarily a problem, as long as the actuator design complies with the design principles of this field. We have seen how a very common actuation method in soft wearable robots is by means of electromagnetic or pneumatic actuators driving the wearer’s joints by means of cables, artificial tendons usually routed inside Bowden sheaths that are placed along the arms or the legs, as in the devices presented in [15] and [29], respectively. In these cases, the actuators are placed remotely from the joint they drive and a long cable is required to transmit their force and motion to the point of actuation.

Given that in the case of soft wearable robots it is acceptable to use long cables to transmit the motion from the actuators to the point of actuation, provided that they are routed along some kind of flexible element that can conform to the user's body shape and movements, why not apply this same concept to the design of an SMA-based actuator? This design approach is what this thesis proposes: the use of a long SMA wire, capable of providing displacements in the range of several centimeters, routed inside a Bowden sheath to implement a lightweight, powerful and flexible actuator to be used in soft wearable robots.

The SMA transducer of the actuator is a Flexinol high temperature wire, with an austenite start temperature of 90 °C, a diameter of 0.5 mm and a pull force of about 35 N [86]. The length of the wire is 900 mm to yield a displacement of the order of 20-30 mm. As for the Bowden sheath, it is composed of a polytetrafluoroethylene (PTFE) internal tube and a stainless steel helical outer sheath.

In a Bowden transmission system, the material of the sheath greatly affects the performance of the actuator because of the frictional losses between the inner wire and the outer sheath. In [173], frictional losses of Bowden cables are modeled as the frictional losses of a cable sliding at a constant velocity around a stationary cylinder according to the Capstan equation:

$$F_{S1}/F_{S2} \cong e^{-\mu\Theta} \tag{3.1}$$

where μ is the coefficient of sliding friction and Θ is the sum of all bending angles along the Bowden sheath.

From Equation 3.1 it is clear that using a sheath made of a material with a small coefficient of friction would reduce frictional losses and increase the force transmission efficiency of the actuator. The low coefficient of friction of PTFE (0.04) coupled to its high temperature tolerance (up to 250 °C) make this material well suited for this application. In addition, considering that the SMA transducer is activated by an electrical current, as will be seen in Section 3.2.1, the PTFE tube also acts as an electrical insulator. A very small diameter tube has been selected to minimize the volume of air between the SMA wire and the inner surface of the PTFE tube and thus maximize the conductive heat transfer from the wire to the tube.

As mentioned above, the Bowden sheath consists of two layers, because the PTFE tube is not rigid enough to withstand the force of the contracting SMA element without being deformed. The PTFE tube has been inserted into a stainless steel helical-shaped tube that is rigid enough not to be deformed when the SMA wire contracts, but at the same time, thanks to its helical shape, is flexible enough to allow the actuator to bend. The arrangement of the multilayer Bowden sheath is shown in Figure 3.2.

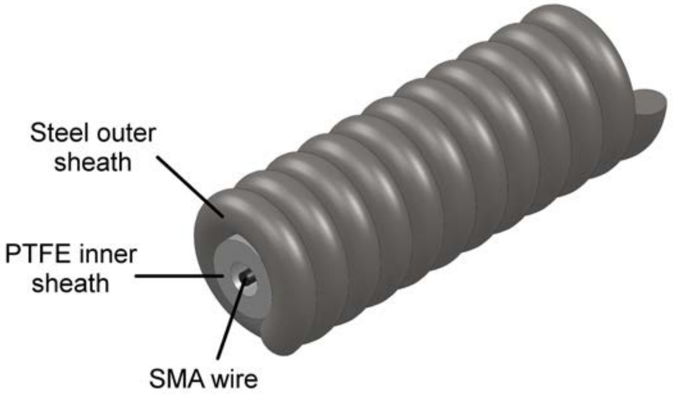

Figure 3.2: Multilayer configuration of the Bowden sheath.

One important outcome of this configuration regarding the performance of the actuator is that the helical outer tube acts as a heat sink, increasing the actuation frequency by reducing the cooling time of the SMA wire. The reason for this improvement is that heat rejection is increased because the sum of heat transfer by conduction through the two layers of the sheath and heat transfer by convection from the metallic sheath to the air is greater than the heat rejection from the SMA wire alone. Moreover, as the steel sheath is a helix, its convection area is larger than that of a tube with the same diameter, further improving heat rejection. The increased heat rejection capabilities of the actuator can be demonstrated computing the thermal resistance (the resistance of a material to heat flow) of each element of the thermal system comprising the SMA wire and the multilayer Bowden sheath, whose physical and thermal parameters are shown in Table 3.1.

Element	**Parameter**					
	h $(\frac{W}{m^2K})$	k $(\frac{W}{mK})$	$\varnothing_i(mm)$	$\varnothing_o(mm)$	A (m^2)	L (m)
SMA wire	44.37	-	-	0.508	$1.436 * 10^{-3}$	0.9
PTFE sheath	-	0.25	0.66	1.168	-	0.9
Steel sheath	13.68	12-45	1.4	3	$9.77 * 10^{-3}$	0.9

Table 3.1: Actuator parameters.

The convective thermal resistance of the SMA wire in still air is computed as:

$$R_{conv_{SMA}} = \frac{1}{h_{SMA} * A_{SMA}} = 14.2\, K/W \tag{3.2}$$

For the case of the SMA wire inside the multilayer sheath, the thermal resistance of the system is the sum of the conductive thermal resistance of the PTFE sheath and the conductive and the convective thermal resistances of the steel sheath:

$$R_{cond_{PTFE}} = \frac{ln(\varnothing_{o_{PTFE}}/\varnothing_{i_{PTFE}})}{2 * \pi * k_{PTFE} * L} = 0.4038\, K/W \tag{3.3}$$

$$R_{cond_{st}} = \frac{ln(\varnothing_{o_{st}}/\varnothing_{i_{st}})}{2 * \pi * k_{st} * L} = 4.73 * 10^{-3}\, K/W \tag{3.4}$$

$$R_{conv_{st}} = \frac{1}{h_{st} * A_{st}} = 7.48\, K/W \tag{3.5}$$

$$R_{tot} = R_{cond_{PTFE}} + R_{cond_{st}} + R_{conv_{st}} = 7.89\, K/W \tag{3.6}$$

With the above calculations it is demonstrated that the multilayer Bowden sheath improves heat rejection by reducing the thermal resistance of the system: the thermal resistance of the designed actuator is 45 % lower than that of the SMA wire without the multilayer sheath. As will be seen in Section 3.3.2, this can result in a 30 % reduction in cooling time compared to an unsheathed wire. On the other hand, the fact that the Bowden sheath increases heat rejection means that more energy has to be provided to trigger the SME of the SMA transducer, resulting in a higher power consumption than in the case of unsheathed wire.

The multilayer Bowden sheath has another advantageous feature regarding SMA actuation: it reduces the thermal runaway effect in the SMA wire. Thermal runaway, or positive feedback, is a process where, due to an increase in temperature, some property of the material changes in such way that makes temperature increase further, initiating a cycle in which the temperature rises rapidly and, if left uncontrolled, can destroy the material. In the case of SMAs, thermal runaway is a consequence of the shortening of the wire when it is heated and the material transforms from martensite to austenite. This shortening decreases the electrical resistance of the wire. If the voltage powering the actuator is constant, a decrease in its resistance means an increase of the electrical power in the wire, which causes an increase in temperature. The more the wire contracts, the more its temperature increases, which makes it contract faster, initiating the thermal runaway process. When the wire contraction is controlled, thermal runaway produces an overshoot when the commanded position reference is reached, regardless of how well the controller is tuned. Thanks to the multilayer sheath, the accelerated increase of the SMA wire temperature is absorbed and attenuated by the thermal conduction of both PTFE and steel. This has a beneficial effect on the control of the SMA actuator, as the overshoot that takes place when the wire is commanded to contract is greatly reduced, even eliminated.

3.2 Electronics

In order to operate the designed actuator, a power electronics system capable of providing the activation current to the SMA transducer in a regulated manner is required, as well as a control electronics system that executes the control loops to be able to command the output position of the actuator. Both systems are briefly described below.

3.2.1 Power electronics

As we have seen in Chapter 2, using electrical energy as the input of an actuator has some advantages in terms of compatibility with the energy domain of the rest of the system where the actuator is installed, faster operation and availability and simplicity of the electronic components used in the control and conditioning systems. In the case of SMAs, electrical energy activation triggers an electromechanical transduction process, in which the alloy is heated by means of the Joule effect by making an electrical current flow through the wire. We have also seen how, in this case, an SMA actuator driven by a PWM modulated controller is more robust to external disturbances and has a lower energy consumption than if it were controlled by a continuous signal, while maintaining the same control accuracy.

Based on these considerations, we have opted for electromechanical transduction by means of electrical current as the activation method of the designed actuator. For this purpose, we have designed a 16-channel power driver which can regulate the current of up to 16 actuators, each channel consisting of a STMicroelectronics STP310N10F7 power MOSFET[1] commutation circuit driven by a PWM signal from the control electronics. Due to the high current that can flow through the power drivers of the SMAs, each channel of the power electronics is electrically insulated from the rest of the hardware by an optocoupler, to protect the control electronics and other connected equipment.

3.2.2 Control electronics

In Chapter 2, we have seen how the nolinearities resulting from the thermal hysteresis of SMAs negatively impact the control of the position or force generated by an actuator using this material as a transducer. We have also reviewed some techniques that different authors propose to compensate for this nonlinear behavior and, in Chapter 5, the control algorithm proposed in this thesis to achieve a robust and accurate position control of the actuator will be detailed.

---

[1] `www.st.com/en/power-transistors/stp310n10f7.html`

The control loop of the actuator will be executed in an embedded system, in anticipation of a possible integration of the actuator, power electronics and control electronics in the same device. The actuator controller is a STMicroelectronics STM32F407VG high-performance microcontroller unit (MCU)[2]. This MCU is based on a 32-bit RISC ARM processor core belonging to the Cortex-M4 family. Among other features, this MCU has an operating frequency of 168 MHz, a floating-point processing unit (FPU), a digital signal processor (DSP), plenty of digital and analog inputs/outputs, and several different communication interfaces (UART, I2C, SPI) that allow connection to external devices such as sensors or computers. The controller firmware in charge of running the control loop, reading and processing data from the sensors and managing the communications is implemented in C.

The control electronics are connected to a host PC which is used to send both manual control commands for the power electronics (fixed values of the duty cycle of the PWM signal) as well as position references for the control loop. In addition, the control electronics sends to the host PC the data measured by the sensors available on the test bench used to characterize the actuator, as described in the following section. In order to send the control commands and visualize and save the received data for further analysis, an application developed in Python runs on the host PC.

3.3 Characterization

We have subjected the designed actuator to a series of characterization tests aimed to study its nominal and maximum operational values. For this purpose, the generated displacement and force and the cooling time for different input energy values have been measured.

The effects of the multilayer Bowden sheath have also been analyzed. First, the performance of the unsheathed transducer and of the complete actuator have been compared for the same input power, to show the negative effects of the Bowden sheath on the actuator power consumption. The reduction of the cooling time of the SMA transducer caused by the increased heat rejection due to the heat sink function of the sheath has also been quantified. Finally, the influence of the bending angle of the flexible body of the actuator on its performance has been measured.

3.3.1 Experimental setup

The test bench used in the characterization experiments has been specifically designed to study the influence of the Bowden sheath on the actuator performance. Its structure allows to set the bending angle of the actuator in a range of 0 to 180 degrees in

---

[2] `www.st.com/en/microcontrollers-microprocessors/stm32f407vg.html`

10 degree increments (as shown in Figure 3.3) to measure how this parameter affects the operation of the actuator. The test bench is composed of this hinged structure and the mechanical interfaces to fix the actuator, a Hall effect linear position sensor with a resolution of 0.488 μm (AMS AS5311[3]) to measure the displacement of the SMA wire, a miniature load cell (Omicron Sensors OMF02[4]) to measure the force exerted by the actuator, the power electronics that provides the electric current to the SMA element, the control and data acquisition electronics and a PC to store the data and communicate with the control electronics.

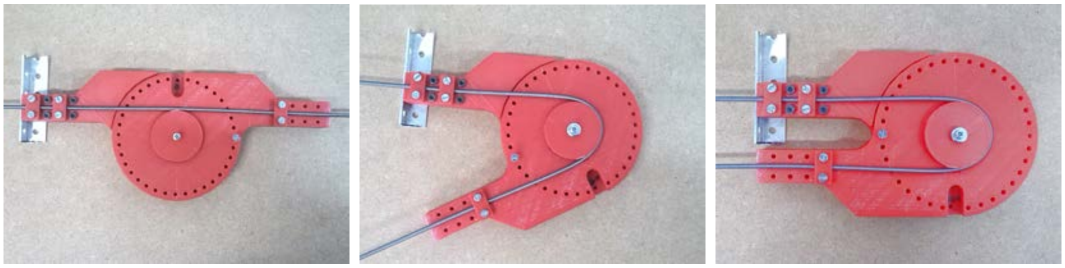

Figure 3.3: Bending angle test bench.

To achieve a repeatable actuation, an external load exerting a pulling force to elongate the SMA wire back to its initial length during the cooling phase is needed. The test bench allows using a hanging mass, a spring, or a combination of both as the source of this “resetting” force. The test bench has a sliding element that acts as the mechanical interface that connects the moving end of the SMA wire to the external load. This element is displaced upon the contraction of the wire during the M-A transformation and by the external load during the A-M transformation, so it also serves as the element whose displacement is measured to obtain the strain of the wire. A multipole magnetic strip is placed on top of this sliding part to be able to measure its displacement with the Hall effect linear position sensor installed on the test bench. The other end of the SMA wire is fixed to one end of the Bowden sheath, which in turn is attached to the structure of the test bench. The whole arrangement, including control electronics and power electronics, is shown in Figure 3.4.

---

[3] `www.ams.com/as5311`

[4] `www.omicron-sensors.eu`

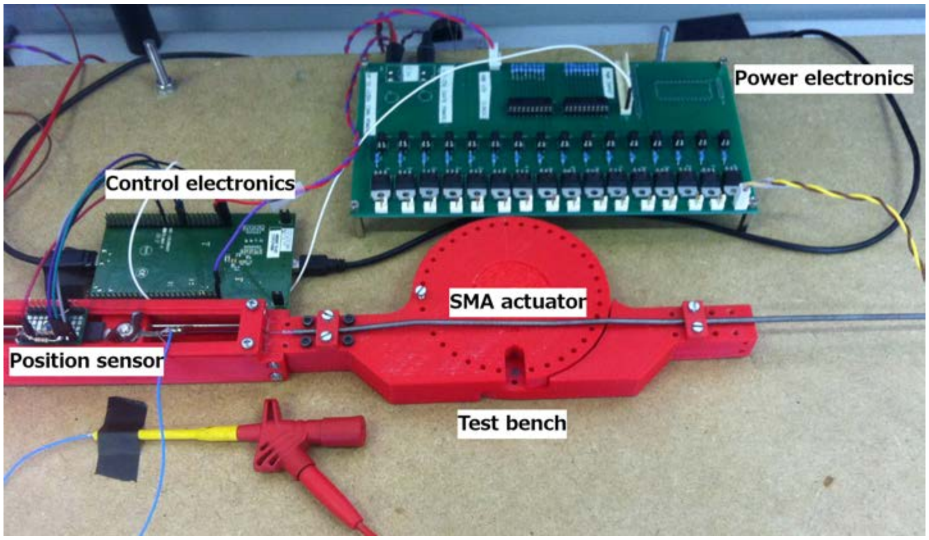

Figure 3.4: Test bench

3.3.2 Results

For the completion of these tests, the actuator has been preloaded with a total force of 50 N, divided between a constant force of 30 N provided by a hanging mass and a force of 20 N generated by the pretension of the bias spring. The actuator has been connected to one of the channels of the power electronics powered with a voltage of 18 V. The SMA transducer has been activated by means of different current pulses with a fixed amplitude of 4 A and a variable duration ranging from 1 s to 2.8 s, in 0.2 s increments. The average measured resistance of the wire has been 4.17 Ω, making an average power consumption of 66.75 W.

Nominal operation

The obtained nominal operation values are summarized in Table 3.2 and plotted in Figures 3.5 and 3.6. The cooling time has been computed taking into account that the manufacturer assumes that the wire has cooled when it reaches a deformation of 0.5 % of its initial length [86], which for our 900 mm long transducer is 4.5 mm.

Pulse duration (s)	**Input energy (J)**	**Maximum displacement (mm)**	**Maximum force (N)**	**Cooling time (s)**
1	66.75	5.94	51.82	0.34
1.6	106.8	15.25	57.06	2.36
2.2	146.85	24.53	63.7	3.74

Table 3.2: Nominal operation values.

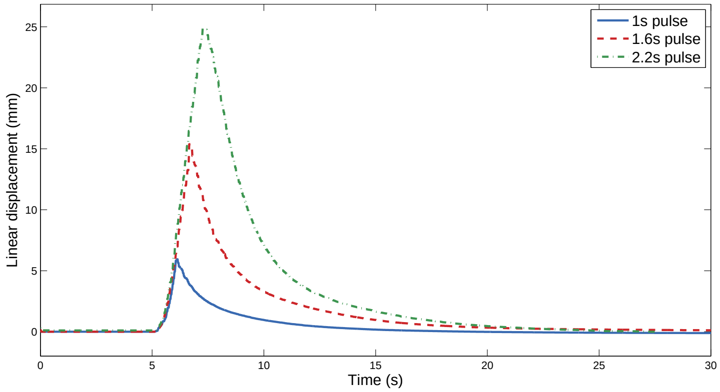

Figure 3.5: Actuator output displacement depending on input pulse duration.

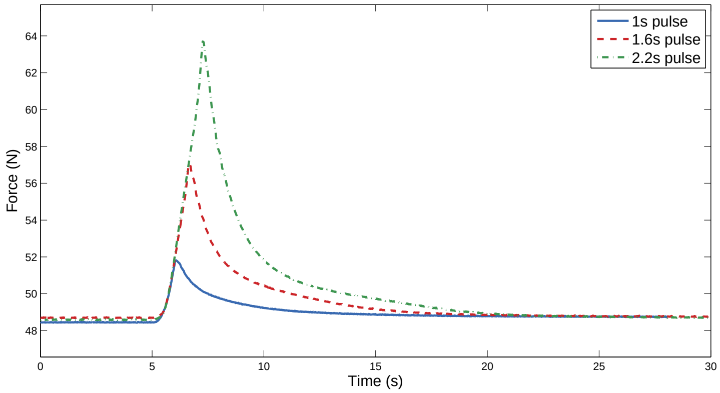

Figure 3.6: Actuator output force depending on input pulse duration.

In these figures we can see how the increment in both position and force for variations of about 40 J in the input energy is very noticeable, about 10 mm in the case of the position and about 6 N in the case of the force. It can also be seen how at first cooling is very fast, faster when the deformation is greater, but as the displacement approaches the curve asymptote, cooling becomes increasingly slower due to the smaller difference between the temperature of the transducer and ambient temperature.

Maximum operation

The obtained results regarding the maximum displacement and force of the actuator are summarized in Table 3.3 and shown graphically in Figures 3.7 and 3.8.

Pulse duration (s)	Input energy (J)	Maximum displacement (mm)	Maximum force (N)	Cooling time (s)
2.4	160.2	25.98	69.09	4.38
2.6	173.55	26.31	69.67	4.42
2.8	186.9	27.45	70.7	5

Table 3.3: Maximum operation values.

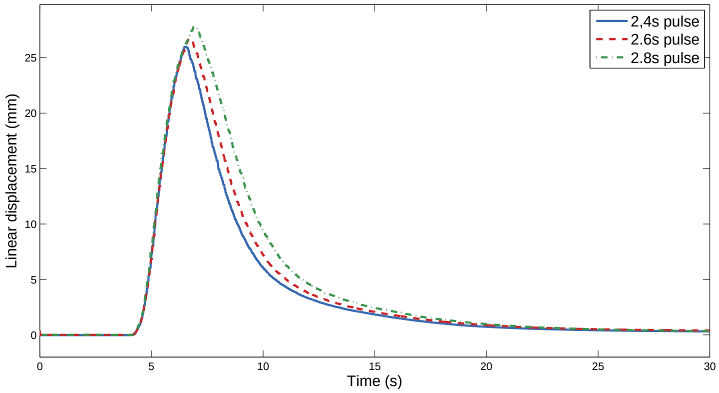

Figure 3.7: Actuator reaching its maximum output displacement.

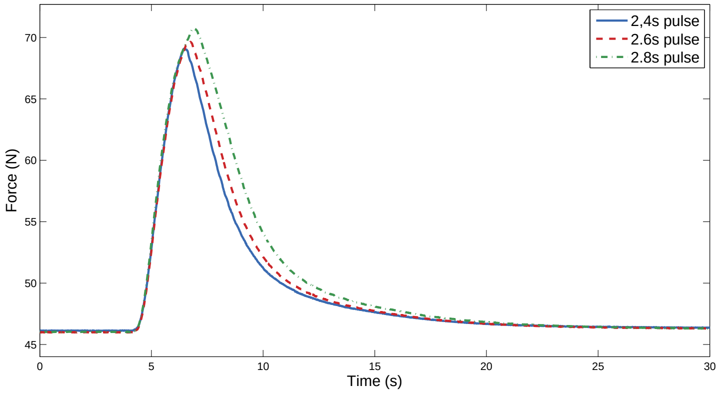

Figure 3.8: Actuator reaching its maximum output force.

As can be seen, beyond the input energy value of 146.85 J, the actuator response begins to saturate, and the increments obtained for variations of 13 J are only about 1 mm in the case of the position and 1 N or less in the case of the force. In addition, the higher the input energy, the longer it will take for the SMA wire to cool as the Bowden sheath will have stored more heat.

Influence of the Bowden sheath on the actuator performance

As already discussed, one of the consequences of using the Bowden sheath is that heat rejection from the SMA transducer to the environment is increased due to the lower thermal resistance of the system. The downside of this is that, to achieve the same level of deformation, more energy has to be applied to the actuator than to an unsheathed wire, as some of that energy is absorbed by the sheath. This can easily be demonstrated by applying the same input energy to the actuator and to its transducer without the sheath, measuring the displacement in both cases. Indeed, as Figure 3.9 shows, for an input energy of 106.8 J (corresponding to a current pulse of 4 A and a duration of 1.6 s) the displacement obtained with the actuator is approximately half of that obtained with the SMA wire without sheath. However, it should be noted that the result shown in Figure 3.9 has been obtained with the sheath at room temperature, which makes energy absorption higher. When the sheath is at operating regime temperature, after a series of actuation cycles, the energy it absorbs is reduced and the power consumption of the actuator is less affected.

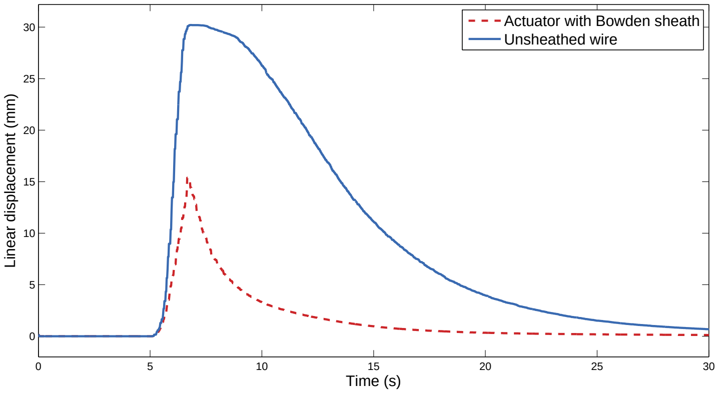

Figure 3.9: Actuator and unsheathed wire output displacement comparison for the same input energy.

Despite the above negative effect, the steel outer sheath of the actuator also has the positive effect of acting as a heat sink, increasing the convection heat transfer rate and thus reducing the cooling time of the SMA wire, as already discussed in Section 3.1. This outcome can be seen in Figure 3.10, which shows the variation of the controlled position of a bare SMA wire and of the same wire inside the multilayer sheath. Both the unsheathed transducer and the actuator have been driven in a controlled manner (using the controller implemented in Chapter 5) to ensure that the displacement is exactly the same in the two cases.

For the data in Figure 3.10 the cooling time has been 4.83 s for the bare SMA wire and 3.33 s for the wire inside the Bowden sheath, which represents a reduction of more than 30 %.

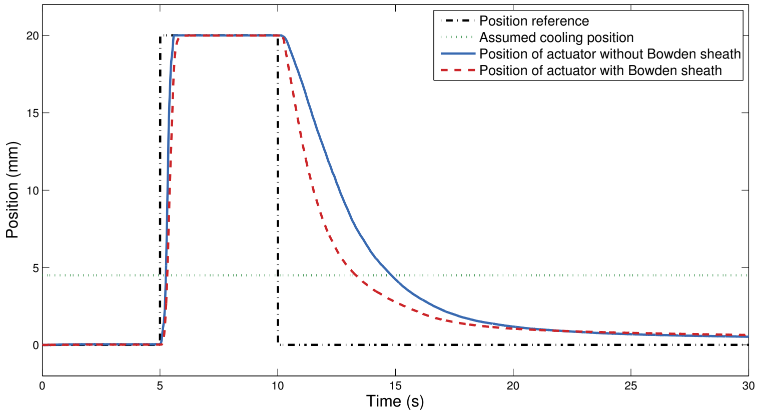

Figure 3.10: Influence of the Bowden sheath on the SMA wire cooling time.

Finally, the effect of the Bowden sheath bending angle on the actuator operation has been analyzed. For this purpose, the bending angle has been increased from 0 to 180 degrees in 10 degree increments while keeping the bending radius at a constant value of 20 mm. For each angle, the actuator has been driven by the same signal, a current pulse with an amplitude of 4 A and a duration of 2.2 s, and the maximum position and force values have been measured for each case.

The results of this test are shown in Figure 3.11, where it can be seen that the relationship between the variation of both measurements is almost linear, which makes sense considering that the variation in the opposing force is due to the displacement of the bias spring.

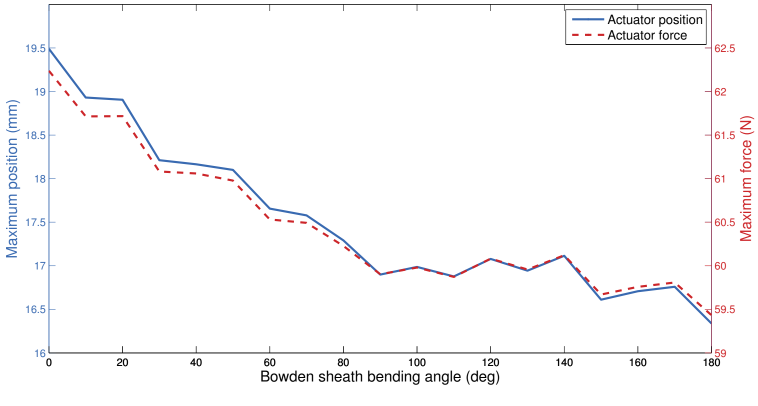

Figure 3.11: Actuator performance depending on the Bowden sheath bending angle.

While the maximum attainable position is reduced by 16.2 %, the maximum force decreases by only 4.5 %. However, it should be noted that force measurements are biased by the preloading force of 50 N. If this value is subtracted from the maximum force measurements to take into account only the force exerted by the SMA wire to displace the bias spring, the force reduction percentage corresponds to that of the displacement. These results are very similar to the theoretical force transmission efficiency in a Bowden cable transmission given by the Capstan equation. Applying Equation 3.1 to our case, with a $\mu_{PTFE} = 0.04$ and a $\Theta = \pi$ rad, the force transmission efficiency is $F_{out}/F_{in} \simeq 0.88$, which is very close to the value of 0.84 that is obtained from the experimental data plotted in Figure 3.11.

3.4 Conclusions

In this chapter we have proposed a solution that addresses one of the limiting factors when designing an actuator that uses a SMA wire as its transducer: the limited linear strain that the SMA element can provide. As the deformation induced by the shape memory effect in a SMA wire is limited to only 3-4 % of its length, it is necessary to use a very long wire to obtain displacements that are in the range of several centimeters.

We have considered that the usual design approach of routing the wire back-and-forth through a pulley array to reduce the size of the actuator has some drawbacks, such as the added weight, frictional losses and increased fatigue of the material, and fails to meet the design premises of soft wearable robots. Instead we propose that, given that some of the most common actuation systems for this type of devices make use of long cables to transmit force and motion from the actuators to the points of actuation, the use of long SMA wires is not a problem when designing actuators for soft wearable robots.

The adopted solution is based on cable-driven actuation systems, which use the principle of Bowden cable actuation to remotely transmit the force and motion of the actuators. The flexible SMA actuator design based on the Bowden transmission system certainly has some features that make it a potential alternative to the use of conventional actuators in soft exoskeletons, as it solves some of the limiting factors of SMA actuators. The possibility of using long SMA wires inside a flexible body makes it feasible to design an actuator that is able to provide the large displacements often required by soft exoskeletons, and that is easy to integrate and adapt into their flexible and dynamic structures. Although the designed actuator is very similar to cable-driven systems, it has a significant improvement that sets it apart from the latter: while cable-driven devices have almost all the weight of the actuation system located at the point where the actuators are installed, the weight of the flexible SMA actuator is distributed along its entire length, making the whole device more comfortable to wear. One can think of the designed actuator as a cable-driven system in which the transmission element is also the active element, unlike conventional cable-driven systems where the active element, the actuator, and the transmission, the cable, are separate entities.

The designed actuator is capable of providing a maximum displacement in its nominal regime of about 24 mm and a maximum force of nearly 64 N which, considering its low volume and weight, clearly outperforms the capabilities of other actuation technologies. Thanks to the low coefficient of friction of the PTFE inner tube of the multilayer Bowden sheath, frictional loses at the bending points are minimized and the impact on the actuator performance is minimal. Moreover, the helical steel outer sheath increases heat rejection from the SMA wire to its surroundings, as the outer surface of the actuator is greatly increased. This results in a 30 % reduction of the cooling time of the SMA wire with respect to a bare wire of the same dimensions and, therefore, a greater actuation frequency. With the passive cooling provided by the heat sink effect of the Bowden sheath, the use of active cooling systems is avoided. This is a highly beneficial feature in general, and particularly desirable in the case of wearable robots, because an increase in the actuation bandwidth is obtained without the added weight of an active system, such as liquid cooling or compressed air refrigeration, that would require additional hardware (fluid reservoir, pumps, valves and filters).

Chapter 4

SMA transducer model

In Chapter 2 we have seen how shape memory alloys are complex materials in which the main properties that define their behavior (strain, stress and temperature) are directly or indirectly interrelated. For example, the strain of the material is related to its temperature and its length. In turn, the temperature depends on the input energy, which, if provided electrically by means of the Joule effect, depends on the electrical current. If the input voltage is kept constant, the current depends on the electrical resistance of the material. As with any material, electrical resistance is affected by the length of the SMA element. Additionally, in the case of these alloys, electrical resistance is also related to the proportion of martensite and austenite crystals, a property that varies with the temperature and the applied stress.

Being a material with such a complex behavior, the development of applications that use SMA components is often a challenging and costly process, both in time and financially. It is therefore important to have models that can simulate simulate the physical processes of these alloys and the interaction between the different properties that define them. From the more general perspective of the product engineering process, before the prototype design and testing phases, a model of the system, developed taking into account the design requirements and specifications of the product, is required. To design commercially viable SMA applications and avoid the possible causes of failure, it is necessary to follow this kind of systematic design process [174] and therefore it is necessary to have models that can be incorporated into such process. For these reasons, a large part of SMA research is devoted to develop models that try to reproduce the behavior of this material as accurately as possible, as we have reviewed in Chapter 2.

Given the above considerations, a thermomechanical model of the SMA transducer of the actuator presented in Chapter 3 has been developed in this thesis. Even though it is not a complete actuator model, due to the complexity of modeling the influence of the Bowden sheath on the transducer thermal processes, this development offers a very powerful tool to better understand the operation of this material and to be able to identify its strengths and weaknesses so that new applications can be designed to exploit the former and solve the latter.

The rest of this chapter is organized as follows. Section 4.1 describes each of the sub-models that constitute the developed model. The validation of the model is carried out in Section 4.2, which includes a list of all the numerical parameters used in the model as well as the presentation and analysis of the obtained results. Finally, the most noteworthy conclusions are discussed in Section 4.3.

4.1 SMA wire model

Considering that the SMA transducer used in the actuator designed in this thesis is a wire under axial stress, the proposed model has been developed based on a one-dimensional phenomenological approach with assumed phase transformation kinetics, as we have seen how this type of models provide accurate results for this particular geometrical configuration. The proposed model has been implemented in MATLAB/Simulink and is composed of several blocks, as shown in Figure 4.1, each of which models an aspect of the transducer:

- Input energy: this block computes the input thermal energy Q_{in} as a function of an input voltage. An important part of this block is the wire electrical resistance model, that considers that resistance is a function of wire length and martensite fraction, and that the resistivity values of the martensite and austenite phases are a function of temperature and stress.
- Heat transfer: the output of this block is the wire temperature, which is obtained from the energy balance equation of the system. The energy variation caused by the latent heat of transformation is taken into account, as this term has a big influence on the heating and cooling times.
- Phase kinetics: this block computes the martensite volume fraction using the Duhem differential model, following Likhachev's approach to modeling minor hysteresis loops using scaling constants.
- Constitutive equation: the Brinson constitutive equation has been used here, considering that the martensite and austenite phases are in series and thus using the Reuss scheme in the Young's modulus expression.
- Dynamics and kinematics: the wire displacement is calculated from the system dynamics. Two different dynamic models can be selected: one in which the wire acts on a hanging mass and another in which it acts on a spring. The kinematic model computes the strain as a function of wire displacement.

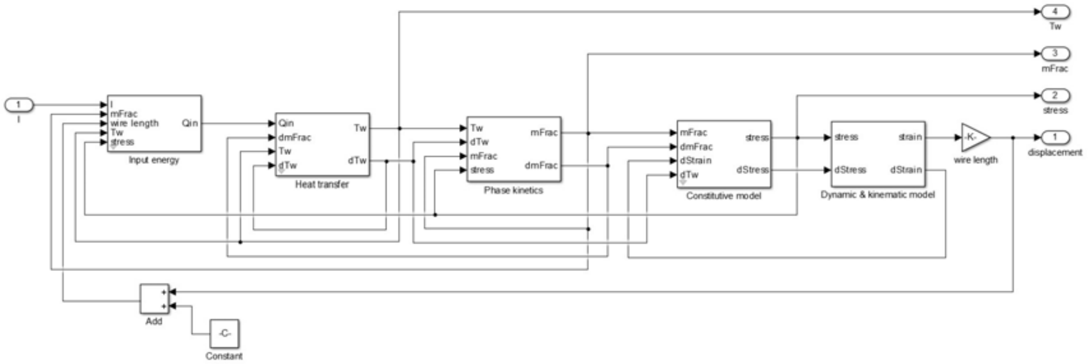

Figure 4.1: Block diagram of the developed SMA wire model.

4.1.1 Input energy

The shape memory effect of an SMA wire is commonly activated by passing an electrical current through it. Due to the electrical resistance of the wire, its temperature rises because of the Joule effect. This current can be directly provided by a current source, or can be the product of applying a differential voltage between both ends of the wire. The former method is used in the experimental tests conducted to validate the model, presented in Section 4.2. Consequently, the input of the developed model is an electrical current, which the first block converts into the input thermal energy of the SMA wire with the following expression:

$$\dot{Q}_{\text{in}} = P_{\text{el}} = I_{\text{in}}^2 * R_{\text{SMA}} \tag{4.1}$$

where $I_{\text{in}}(t)$ is the input current and $R_{\text{SMA}}(t)$ is the electrical resistance of the SMA wire. Unlike some other SMA phenomenological models that assume that the electrical resistance of the wire is constant, here, the block that converts the input voltage into the input energy of the wire takes into account the varying length of the wire, as well as other factors that influence the value of the electrical resistance.

Electrical resistance model

The expression that defines the electrical resistance of a conductor with a cylindrical shape, such as a wire, is:

$$R = \rho \frac{l}{S} \tag{4.2}$$

where ρ is the electrical resistivity of the material, l is the length of the wire and S is its cross sectional area. When modeling an SMA wire in tensile deformation, whose length decreases when it undergoes a transformation from martensite to austenite, it can be seen from Equation 4.2 that, if the deformation is large enough, assuming that the electrical resistance is constant is an oversimplification that can lead to erroneous results. With the presented model, we are precisely interested in modeling the behavior of long SMA wires that produce significant displacements, so the variation of the length of the wire must be taken into account in the equation that computes the value of its electrical resistance. It has to be noted that the cross sectional area of an SMA wire also changes as the wire heats up and shortens. However, the variation is small enough as not to change the electrical resistance value significantly.

Not only the electrical resistance of an SMA wire changes proportionally to its length, but also its resistivity is different depending on whether the material is in the pure austenite phase or in the pure martensite phase. Assuming that these phases are in series (which is supported by experimental data, as will be discussed below), the total resistivity of the wire can be expressed with the following equation:

$$\rho_{el_{\text{SMA}}}(\xi) = \rho_{\text{M}}\xi + \rho_{\text{A}}(1-\xi) \tag{4.3}$$

where ρ_{M} is the resistivity for pure martensite, ρ_{A} is the resistivity for pure austenite and ξ is the martensite fraction.

Moreover, according to Novak *et al.* [175] and Song *et al.* [176], the electrical resistivities of the martensite and austenite phases, ρ_{M} and ρ_{A}, are affected by the temperature and stress of the SMA wire, and have the following formulation:

$$\rho_{\text{M}}(T,\sigma) = \rho_{0\text{M}} + (T_{\text{SMA}} - T_{0\text{M}})\frac{\delta\rho_{\text{M}}}{\delta T} + \sigma_{\text{SMA}}\frac{\delta\rho_{\text{M}}}{\delta\sigma} \tag{4.4a}$$

$$\rho_{\text{A}}(T,\sigma) = \rho_{0\text{A}} + (T_{\text{SMA}} - T_{0\text{A}})\frac{\delta\rho_{\text{A}}}{\delta T} + \sigma_{\text{SMA}}\frac{\delta\rho_{\text{A}}}{\delta\sigma} \tag{4.4b}$$

where $\rho_{0\text{M}}$ and $\rho_{0\text{A}}$ are the martensite and austenite nominal resistivities, $T_{0\text{M}}$ and $T_{0\text{A}}$ are the temperatures at which the nominal resistivities are measured, $\delta\rho_{\text{M}}/\delta T$ and $\delta\rho_{\text{A}}/\delta T$ are the linear temperature dependencies of the martensite and austenite resistivities, $\delta\rho_{\text{M}}/\delta\sigma$ and $\delta\rho_{\text{A}}/\delta\sigma$ are the linear stress dependencies of the martensite and austenite resistivities, T_{SMA} is the SMA wire temperature and σ_{SMA} is the SMA wire stress.

By substituting Equation 4.3 in Equation 4.2, the expression that models the behavior of the electrical resistance of an SMA wire becomes:

$$R_{\text{SMA}}(\xi,T,\sigma) = \frac{(\rho_{\text{M}}(T,\sigma)\xi + \rho_{\text{A}}(T,\sigma)(1-\xi))l_{\text{SMA}}}{S_{\text{SMA}}} \tag{4.5}$$

where $\rho_{\text{M}}(T,\sigma)$ and $\rho_{\text{A}}(T,\sigma)$ are equations 4.4a and 4.4b, respectively.

4.1.2 Heat transfer model

The heat transfer sub-model computes the instantaneous temperature of the electrically heated SMA wire, as well as the rate of change of this temperature, from its energy balance equation. From the first law of thermodynamics, we have:

$$\frac{\text{dE}_{\text{SMA}}}{\text{dt}} = \dot{Q}_{\text{in}} - \dot{Q}_{\text{out}} + \dot{W}_{\text{in}} - \dot{W}_{\text{out}} \tag{4.6}$$

On the left side of the equation we have the internal energy variation of the wire. On the right side of the equation we have the input thermal energy $\dot{Q}_{\text{in}}$, provided by the electrical current passing through the wire, and the output thermal energy $\dot{Q}_{\text{out}}$, which is the sum of the thermal loses due to the processes of convection, conduction and radiation. Besides these heat sources and sinks, the latent heat of transformation has to be quantified to account for the thermal variations caused by the forward and reverse phase transformations. Finally, the work done by the wire $\dot{W}_{\text{out}}$ and done on the wire $\dot{W}_{\text{in}}$ contributes to the variation of the internal energy of the wire. Taking all this into account, for the specific case of an SMA wire heated by the Joule effect, Equation 4.6 can be expanded as follows:

$$\frac{\mathrm{dE}_{\text{SMA}}}{\mathrm{dt}} = P_{\text{el}} - \dot{Q}_{\text{conv}} - \dot{Q}_{\text{cond}} - \dot{Q}_{\text{rad}} + \dot{Q}_{\text{lat}} - \dot{W}_{\text{kin}} - \dot{W}_{\text{pot}} \tag{4.7}$$

Generally, heat is transferred from an electrically heated wire to the environment by three different mechanisms: convection, conduction and radiation. According to Meier and Oelschlaeger [177], heat transfer from an SMA wire in still air to the environment is a 90 % free air convection and a 10 % radiation, neglecting heat conduction from the wire to the clamping elements that fix it to a structure. Velázquez and Pissaloux [178] justify the omission of the heat conduction term assuming that the temperature of an SMA element is uniform at all times because, being a metallic alloy, it has a low internal resistance to heat conduction.

In the present model, heat loses by radiation are also neglected, because of the great influence of the heat convection term on the total thermal loses of the wire. In fact, computing the heat transferred by convection and radiation from an SMA wire with a length of 1 m and a diameter of $0.508 * 10^{-3} m$ at a steady state temperature of 90 °C, to an environment under Earth conditions at an ambient temperature of 22 °C, proves that the energy transferred from the wire to the environment by radiation is only a 0.1 % of the total thermal loses, far from the 10 % value given by Meier. Let:

$$\dot{Q}_{\text{rad}} = \varepsilon_{\text{SMA}} \sigma_{\text{rad}} A_{\text{SMA}} ({T_{\text{SMA}}}^4 - {T_0}^4) = 3.9 * 10^{-3} W \tag{4.8}$$

$$\dot{Q}_{\text{conv}} = h_{\text{SMA}} A_{\text{SMA}} (T_{\text{SMA}} - T_0) = 4.61 W \tag{4.9}$$

where $\varepsilon_{\text{SMA}} = 0.66$ is the emissivity of the SMA (taken from [179]), σ_{rad} is the Stephan-Bolzman constant, $h_{\text{SMA}} = 42.51 W/m^2 {}^\circ C$ is the convection heat transfer coefficient (whose value is calculated in Section 4.4), A_{SMA} is the surface area of the SMA wire, T_{SMA} is the surface temperature of the wire and T_0 the ambient temperature.

According to Jayender *et al.* [149], the convection heat transfer coefficient h_{SMA} in Equation 4.9 can be expressed as a second-order polynomial, to better match experimental observations:

$$h_{\text{SMA}} = h_0 + h_2 T^2 \tag{4.10}$$

where $h_0 = 37.67 W/m^2 {}^\circ C$ so that the value of h_0 is the same that the one computed in Section 4.4 for $h_2 = 0.01$ and $T = 22 {}^\circ C$.

As a consequence of the low energy efficiency of SMAs ($\eta = P_{\mathrm{mech}}/P_{\mathrm{el}} = 1.3\%$) [180], the mechanical power term has little influence on the energy balance and, therefore, kinetic and potential work can also be neglected [181].

Differential scanning calorimetry measurements reveal that the forward and reverse transformations are, respectively, exothermic and endothermic processes during which latent heat is released or absorbed. This has a noticeable effect on the material temperature, which is reflected in the slope changes of the temperature curve that occur in the ranges of transformation temperatures. Except in some cases, such as [177], most models do not include this effect, or do so by using system identification techniques, as in the Dutta and Ghorbel model [107] where this effect is included in the convection heat transfer coefficient through a series of parameters obtained by nonlinear least-squares optimization. We consider more accurate to include this effect as a separate term in the energy balance equation of the system and to express it in terms of measurable physical parameters of the material, because this results in a more general an less dependent model than with identification techniques.

The latent heat flow term $\dot{Q}_{\mathrm{lat}}$ in Equation 4.7 is proportional to the rate of the martensite volume fraction and is expressed as:

$$\dot{Q}_{\mathrm{lat}} = \rho_{\mathrm{SMA}} V_{\mathrm{SMA}} \Delta H \frac{\mathrm{d}\xi}{\mathrm{dt}} \tag{4.11}$$

where ρ_{SMA} is the density of Flexinol, V_{SMA} is the volume of the SMA wire, ΔH is the specific latent heat of transformation of Flexinol and $\mathrm{d}\xi/\mathrm{dt}$ is the rate of change of the martensite volume fraction value. It can be seen how during the heating phase (reverse transformation), when the value of ξ goes from 1 to 0, $\mathrm{d}\xi/\mathrm{dt}$ is negative and $\dot{Q}_{\mathrm{lat}}$ becomes a heat sink in Equation 4.7. This corresponds to an endothermic process in which, if no additional heat power is supplied, the heating rate of the wire is reduced because the system absorbs energy in the form of latent heat, which is consistent with experimental measurements. An analogous rationale can be followed for the cooling phase.

Taking all the above into account, the equation that governs the thermal behavior of the system is as follows:

$$\rho_{\mathrm{SMA}} V_{\mathrm{SMA}} c_{\mathrm{p}} \frac{\mathrm{dT}_{\mathrm{SMA}}}{\mathrm{dt}} = I_{\mathrm{in}}^2 * R_{\mathrm{SMA}} - h_{\mathrm{SMA}} A_{\mathrm{SMA}} (T_{\mathrm{SMA}} - T_0) + \rho_{\mathrm{SMA}} V_{\mathrm{SMA}} \Delta H \frac{\mathrm{d}\xi}{\mathrm{dt}} \tag{4.12}$$

c_{p} is the specific heat capacity of Flexinol, and the rest of the variables have been described above.

4.1.3 Phase kinetics model

To model the phase kinetics of the SMA wire, we have chosen the Duhem differential model along with the scaling coefficients proposed by Likhachev. This model has been chosen over other options such as hysteresis operator models or black box models because it is not necessary to perform a parameter identification for its implementation, as well as because of its ability to depict minor hysteresis loops, which is not possible in some of the aforementioned models. It is important that the proposed model is capable of representing minor hysteresis loops in order to be used in a feedback control system simulation, as it is expected that the controller would command the SMA wire to positions that correspond to partial phase transformations.

According to Likhachev and Koval [110, 111, 112], the main hysteresis loop that relates the martensite volume fraction with the temperature can be represented by two equations, $\xi = z_+(T)$ and $\xi = z_-(T)$, corresponding to the heating and cooling branches of the loop respectively. Moreover, an infinite number of paths corresponding to partial phase transformations exist inside the main loop. The authors propose that each possible trajectory delimited by the heating and cooling branches of the main hysteresis loop must satisfy a differential equation with the following formulation:

$$\frac{\mathrm{d}\xi}{\mathrm{dT}} = S_\pm(\xi, T) \tag{4.13}$$

where $S_\pm(\xi, T)$ are single-valued functions of (ξ, T) belonging to the heating and cooling families of possible trajectories (indicated by the $+$ and $-$ subscripts, respectively). In [110], the authors found a linear relationship between $\mathrm{d}\xi/\mathrm{dT}$ and ξ, which is described by the following expression:

$$S_\pm(\xi, T) = \alpha_\pm(T)\xi + \beta_\pm(T) \tag{4.14}$$

where $\alpha_\pm(T)$ and $\beta_\pm(T)$ are temperature-dependent coefficients that are expressed as a function of the two equations $z_\pm(T)$ that define the main hysteresis loop:

$$\alpha_\pm(T) = \pm\frac{\mathrm{dz}_\pm}{\mathrm{dT}}\frac{1}{z_+ - z_-} \tag{4.15}$$

$$\beta_\pm(T) = \mp\frac{\mathrm{dz}_\pm}{\mathrm{dT}}\frac{z_\mp}{z_+ - z_-} \tag{4.16}$$

Substituting equations 4.15 and 4.16 in Equation 4.14 and rearranging, we finally obtain the differential equations that define all the possible heating and cooling trajectories that conform the main and minor hysteresis loops in the $\xi - T$ plane:

$$\frac{\mathrm{d}\xi}{\mathrm{dT}} = \pm\frac{\mathrm{dz}_\pm}{\mathrm{dT}}\left(\frac{\xi - z_\mp}{z_+ - z_-}\right) \tag{4.17}$$

There are some equations of the proposed SMA model in which the temporal evolution of $\xi(T)$ is needed (e.g. in Equation 4.12). Therefore, we have to compute the time derivative of $\xi(T)$, which is simply:

$$\dot{\xi} = \dot{T}\frac{\mathrm{d}\xi}{\mathrm{dT}} \tag{4.18}$$

Using equations 4.13 and 4.14, the above expression becomes:

$$\dot{\xi} = \dot{T}(\alpha_{\pm}(T)\xi + \beta_{\pm}(T)) \tag{4.19}$$

Developing the above expression for the heating and cooling curves separately, we obtain:

- Heating:

$$\dot{\xi}_{+} = \left[\frac{\mathrm{dz}_{+}}{\mathrm{dT}}\left(\frac{\xi - z_{-}}{z_{+} - z_{-}}\right)\right]\dot{T} \tag{4.20a}$$

- Cooling:

$$\dot{\xi}_{-} = \left[\frac{\mathrm{dz}_{-}}{\mathrm{dT}}\left(\frac{z_{+} - \xi}{z_{+} - z_{-}}\right)\right]\dot{T} \tag{4.20b}$$

For $z_{\pm}(T)$, we can use any expression that describes the hysteresis curve, including the saturated hysteresis that occurs at he maximum and minimum values of the input signal, and that is derivable. For the presented SMA model, we have used the hyperbolic tangent suggested in [172], so the above expressions become:

$$z_{+}(T) = \frac{1}{2}\tanh\left[2\left(\frac{A_{\mathrm{s}} - T}{A_{\mathrm{f}} - A_{\mathrm{s}}} + \frac{1}{2}\right)\right] + \frac{1}{2} \tag{4.21}$$

$$\frac{\mathrm{dz}_{+}(\mathrm{T})}{\mathrm{dT}} = -\frac{1}{A_{\mathrm{f}} - A_{\mathrm{s}}}\mathrm{sech}^2\left[2\left(\frac{\mathrm{A_s - T}}{\mathrm{A_f - A_s}} + \frac{1}{2}\right)\right] \tag{4.22}$$

$$z_{-}(T) = \frac{1}{2}\tanh\left[2\left(\frac{M_{\mathrm{f}} - T}{M_{\mathrm{s}} - M_{\mathrm{f}}} + \frac{1}{2}\right)\right] + \frac{1}{2} \tag{4.23}$$

$$\frac{\mathrm{dz}_{-}(\mathrm{T})}{\mathrm{dT}} = -\frac{1}{M_{\mathrm{s}} - M_{\mathrm{f}}}\mathrm{sech}^2\left[2\left(\frac{\mathrm{M_f - T}}{\mathrm{M_s - M_f}} + \frac{1}{2}\right)\right] \tag{4.24}$$

While the Gaussian probability distribution functions used by Dutta and Ghorbel in [107] depend on four parameters that have to be experimentally obtained (μ_{+}, μ_{-}, σ_{+} and σ_{-}), the hyperbolic tangent functions used here depend on four parameters given by the SMA manufacturer: the four transformation temperatures.

Another factor that has to be taken into account regarding the phase kinetics model is that transformation temperatures are affected by the stress of the wire

[97, 98]. As the stress increases or decreases, the transformation temperatures increase or decrease proportionally. For this reason, as we have seen in Chapter 2, some models include constants that reflect this relationship. In the developed model, the dependence of the transformation temperatures on the applied stress is modeled as follows:

$$M_s = M_{s0} + \frac{\sigma}{C_M} \tag{4.25a}$$

$$M_f = M_{f0} + \frac{\sigma}{C_M} \tag{4.25b}$$

$$A_s = A_{s0} + \frac{\sigma}{C_A} \tag{4.25c}$$

$$A_f = A_{f0} + \frac{\sigma}{C_A} \tag{4.25d}$$

where C_M and C_A are the constants that model the effect of stress on martensite and austenite transformation temperatures, respectively.

4.1.4 Constitutive model

The rate form of the Brinson constitutive equation has been chosen to compute the stress of the SMA wire:

$$\dot{\sigma} = E(\xi)\dot{\varepsilon} + \Omega(\xi)\dot{\xi} + \Theta(\xi)\dot{T} \tag{4.26}$$

The Young's modulus E is expressed as a function of the martensite volume fraction ξ by a rule of mixtures of the moduli of the pure austenite phase and the pure martensite phase. The formulation of $E(\xi)$ proposed by Brinson in [98] considers that the austenite and martensite phases are in parallel and that the transformed martensite is formed in series [182]. This assumption leads to a formulation that is equivalent to the Voigt rule of mixtures:

$$E(\xi) = E_{\mathrm{M}}\xi + E_{\mathrm{A}}(1 - \xi) \tag{4.27}$$

where E_{M} is the Young's modulus for pure martensite and E_{A} is the Young's modulus for pure austenite.

However, according to Auricchio and Sacco [183], experimental data suggest that an SMA rod subjected to uniaxial stress can be considered an austenite-martensite periodic composite and, therefore, the phases are in series. In this case, $E(\xi)$ should be expressed according to the Reuss formulation of the rule of mixtures, which is the formulation used in the present model:

$$\frac{1}{E(\xi)} = \frac{1-\xi}{E_{\mathrm{A}}} + \frac{\xi}{E_{\mathrm{M}}} \tag{4.28a}$$

or equivalently:

$$E(\xi) = \frac{E_{\mathrm{M}} E_{\mathrm{A}}}{E_{\mathrm{M}}(1-\xi) + E_{\mathrm{A}}\xi} \tag{4.28b}$$

The transformation tensor Ω is defined by Liang [184] and Brinson [98] as a function of E, and therefore, its value depends on the martensite volume fraction value. The transformation tensor can be expressed as:

$$\Omega(\xi) = -\overline{\varepsilon}_{\mathrm{L}} E(\xi) \tag{4.29}$$

where $\overline{\varepsilon}_{\mathrm{L}}$ is a material constant called maximum residual strain.

The thermoelastic tensor is often assumed to be constant, because its value is several orders of magnitude smaller than the value of E, having little influence on the stress calculation. Yet, to make the model more accurate, and because this term does not add much complexity, we define the thermoelastic tensor as a function of the thermal expansion coefficient and the Young's modulus:

$$\Theta(\xi) = \alpha(\xi) E(\xi) \tag{4.30}$$

where $\alpha(\xi)$ is the thermal expansion coefficient, which has a different value depending on whether the SMA wire is in a pure martensitic state or whether it is in a pure austenitic state. As with the Young's modulus, we consider that the phases are in series, so by applying the Reuss scheme for the rule of mixtures, the thermal expansion coefficient is expressed as:

$$\alpha(\xi) = \alpha_{\mathrm{M}}\xi + \alpha_{\mathrm{A}}(1-\xi)(1+\nu_{\mathrm{SMA}}) \tag{4.31}$$

where α_{M} is the thermal expansion coefficient for pure martensite, α_{A} is the thermal expansion coefficient for pure austenite and ν_{SMA} is the SMA Poisson's ratio.

4.1.5 Dynamic and kinematic model

The last block of the model corresponds to the element that is actuated by the SMA wire. To validate the model, a real SMA wire is going to be installed in the test bench described in Chapter 3. As explained in Section 3.3.1 of that chapter, the test bench has a sliding element that moves along a linear axis to which the moving end of the SMA wire is attached. Two elements, a suspended mass and a bias spring, can be attached to the sliding part to provide the pulling force needed to restore the initial length of the SMA wire during the cooling phase.

The dynamic model of the system computes the linear displacement of the actuated element from the force applied to it, which is the force exerted by the SMA wire. The force is derived from the stress of the SMA wire obtained from the constitutive model by means of the uniaxial normal stress formula:

$$F_{\text{SMA}} = \sigma * S \tag{4.32}$$

where S is the cross sectional area of the SMA wire.

Two different dynamic models can be selected depending on whether the hanging mass or the spring is used to apply the restoring force. In the first case, the dynamics of the hanging mass system is represented by the following equation [185]:

$$F_{\text{SMA}} = m\ddot{x} + b\dot{x} + mg \tag{4.33}$$

where F_{SMA} is the force exerted by the wire, as defined in Equation 4.32, m is the mass, x is the mass vertical displacement (and hence, the linear displacement of the SMA wire), b is the damping coefficient that accounts for the internal friction of SMA wire as well as other frictional effects of the system and g is Earth's gravitational acceleration.

If the bias spring is used to provide the restoring force, its elongation corresponds to the linear displacement of the actuated element, and the force required to produce this elongation is the force exerted by the SMA wire. Then, the dynamic model is simply:

$$F_{\text{SMA}} = k * x \tag{4.34}$$

where F_{SMA} is the pulling force of the wire as given in Equation 4.32, k is the force constant of the spring and x is the spring elongation (and therefore the linear displacement of the SMA wire).

The kinematic model of the system relates the linear displacement of the actuated element with the SMA wire strain. These two variables form a relationship given by the Cauchy strain formula:

$$\varepsilon = \frac{\Delta x}{L} = \frac{x - L}{L} \tag{4.35}$$

where ε is the SMA wire strain, x is the linear displacement of the actuated element and L is the initial length of the SMA wire.

4.2 Model validation

In order to evaluate the validity of the developed model, a series of tests have been performed with an SMA wire to take displacement, force, voltage and current measurements. From these values, other wire parameters, such as strain, stress, electrical resistance or power consumption, can be derived. These data are compared with those obtained from replicating the same tests with the model, configured with the same parameters as in the real experiments. To perform these tests, we have used the test bench described in Chapter 3, which is equipped with a position sensor and a force sensor with which the displacement and the force exerted by the SMA wire are measured. The voltage drop between the two ends of the wire and the supplied current are registered by the regulated current source. The wire used in the experiments has been the transducer of the actuator presented in Chapter 3, that is, a 900 mm long SMA wire with a diameter of 0.508 mm and an austenite finish temperature of 90 °C.

As mentioned before, both a suspended mass and a spring can be used in the bench to provide the force needed to restore the initial length of the SMA wire during the A-M transformation. The latter case is especially interesting to validate the model since a spring exerts a variable force during the actuation cycle. Regarding modeling, having a variable force is not trivial because, as have been discussed, the transformation temperatures depend on the stress applied to the wire. This means that, as the force exerted by the spring will vary proportionally to the contraction and elongation of the wire, the behavior of the SMA will be altered dynamically, which should be reproduced by the model. On the other hand, using a hanging mass allows to set the force the SMA wire will exert to a desired value and to study the behavior of the real system and of the model under different constant force levels.

4.2.1 Model parameters

Table 4.1 lists the numerical values of all the parameters used in the SMA wire model.

Parameter (units)	**Description**	**Value**
Geometrical parameters		
$\varnothing_{\text{SMA}}(m)$	SMA wire diameter	$0.508 * 10^{-3}$
$l_{\text{SMA}}(m)$	SMA wire length	0.9
$S_{\text{SMA}}(m^2)$	SMA wire cross sectional area	$2.027 * 10^{-7}$
$A_{\text{SMA}}(m^2)$	SMA wire surface area	$1.44 * 10^{-3}$
$V_{\text{SMA}}(m^3)$	SMA wire volume	$1.82 * 10^{-7}$
Electrical parameters		
$\rho_{0\text{M}}(\Omega m)$	Martensite nominal resistivity	$94.585 * 10^{-8}$
$\rho_{0\text{A}}(\Omega m)$	Austenite nominal resistivity	$90.858 * 10^{-8}$
$T_{0\text{M}}(^\circ C)$	Martensite nominal resistivity temperature	0
$T_{0\text{A}}(^\circ C)$	Austenite nominal resistivity temperature	225
$\delta\rho_{\text{M}}/\delta T(\Omega m/^\circ C)$	Martensite resistivity linear temperature dependency	$1.5 * 10^{-9}$
$\delta\rho_{\text{A}}/\delta T(\Omega m/^\circ C)$	Austenite resistivity linear temperature dependency	$0.5 * 10^{-9}$
$\delta\rho_{\text{M}}/\delta\sigma(\Omega m/Pa)$	Martensite resistivity linear stress dependency	$1.5 * 10^{-17}$
$\delta\rho_{\text{A}}/\delta\sigma(\Omega m/Pa)$	Austenite resistivity linear stress dependency	$0.5 * 10^{-17}$
Thermal parameters		
$M_{s_0}(^\circ C)$	Martensite nominal start temperature	72
$M_{f_0}(^\circ C)$	Martensite nominal finish temperature	62
$A_{s_0}(^\circ C)$	Austenite nominal start temperature	88
$A_{f_0}(^\circ C)$	Austenite nominal finish temperature	98
$h_0(W/m^{2\circ}C)$	SMA wire nominal convection heat transfer coefficient	37.67
$\rho_{\text{SMA}}(K/m^3)$	Flexinol density	6450
$c_p(J/Kg^\circ C)$	Flexinol specific heat capacity	837.4
$\delta H(J/Kg)$	Flexinol latent heat of transformation	24183.52
Mechanical parameters		
$C_M(Pa/^\circ C)$	Effect of stress on martensite transformation temperatures	$6.89 * 10^6$
$C_A(Pa/^\circ C)$	Effect of stress on austenite transformation temperatures	$6.89 * 10^6$
$E_M(Pa)$	Martensite Young's modulus	$28 * 10^9$
$E_A(Pa)$	Austenite Young's modulus	$75 * 10^9$
$\alpha_M(^\circ C^{-1})$	Martensite thermal expansion coefficient	6.6^{-6}
$\alpha_A(^\circ C^{-1})$	Austenite thermal expansion coefficient	$11 * 10^{-6}$
$\overline{\varepsilon}_{\text{L}}$	Maximum residual strain	0.038
ν_{SMA}	SMA Poisson's ratio	0.33
Dynamic and kinematic parameters		
$k(N/m)$	Spring force constant	900
b	Damping coefficient	65
$g(m/s^2)$	Gravitational constant	9.81

Table 4.1: Numerical values of the model parameters.

4.2.2 Results

First, we present the results related to the main characteristic that defines the behavior of the SMA: its thermal hysteresis. As there is no experimental temperature data of the real wire, these tests have been limited to perform simulations with the model to demonstrate its ability to reproduce some of the particularities of the material. It will be shown that the model is able to reproduce the effect of the latent heat of transformation, the internal hysteresis loops due to incomplete phase transformations, the displacement of the hysteresis loop due to the variation of the transformation temperatures depending on the stress of the wire and the hysteresis of the electrical resistance.

In the next set of tests, the data generated by the model in terms of displacement, stress and power consumption are compared with the same data obtained from the real wire. To perform these tests, the real wire has been activated using a series of input current pulses and the generated data has been collected. These same tests have been replicated with the model, and the obtained results have been compared with the experimental data for its validation.

SMA hysteresis model results

In the first place, Figure 4.2 shows the temperature curve of the SMA wire corresponding to a current pulse of 4 A with a duration of 1.8 s. In this case, the simulated load has been a mass of 5 Kg.

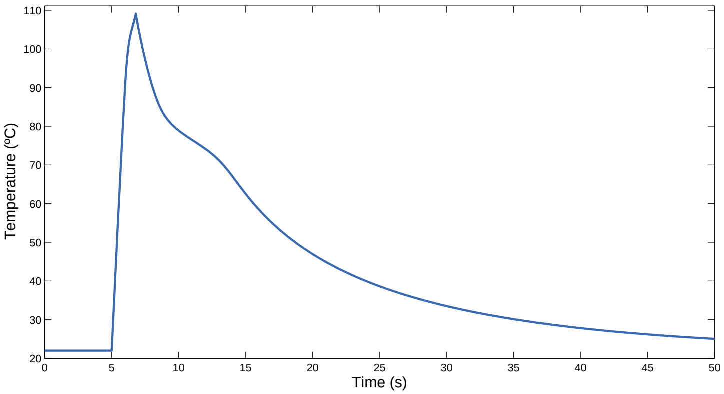

Figure 4.2: SMA wire temperature curve.

The effect of the exothermic reaction that takes place during the forward transformation, modeled by Equation 4.11, is clearly visible during the cooling portion of the temperature curve, in the 10-15 s interval. As the phase transformation generates an additional latent heat that is emitted into the environment, the cooling rate of the wire is reduced until its temperature is below the martensite finish temperature and the transformation is completed. Although the endothermic reaction that takes place during the heating of the wire is also modeled and impacts the performance of the whole model, its effects are not visible in Figure 4.2 because the heating portion of the temperature curve is too steep.

The hysteresis loops of the martensite fraction are shown below. As in the previous test, these data have been obtained by activating the wire with a current pulse of 4 A and a duration of 1.8 s. Two hysteresis loops have been generated, depending on the used load. In Figure 4.3 the model has been configured to use a 3 Kg mass while to obtain the data plotted in Figure 4.4, the load is provided by the bias spring preloaded to 12 N.

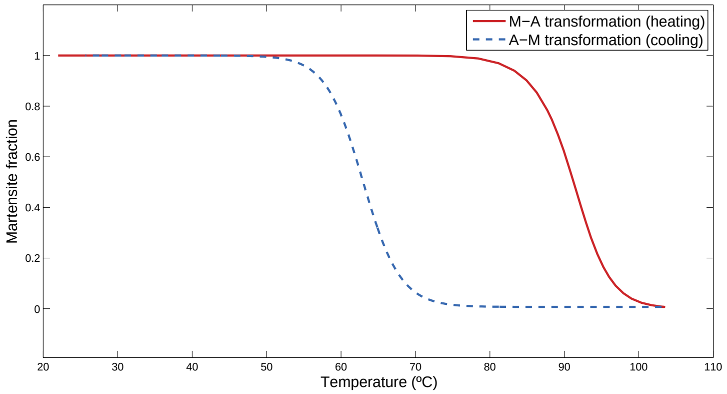

Figure 4.3: Thermal hysteresis of the martensite fraction corresponding to a 3 Kg load.

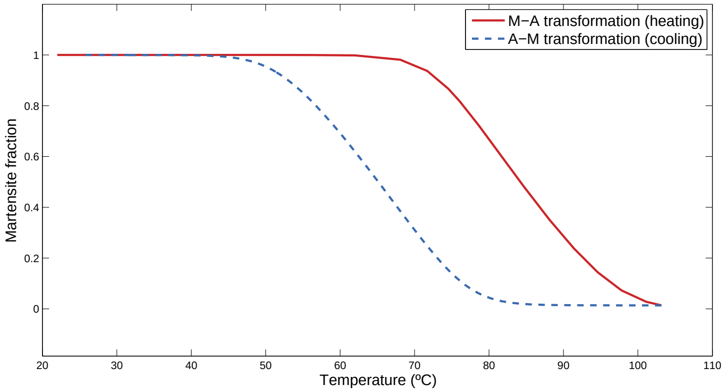

Figure 4.4: Thermal hysteresis of the martensite fraction corresponding to a bias spring load.

The difference in the shape of the hysteresis loops is an evidence of the dependence of the transformation temperatures on the stress of the wire. If the suspended mass is used, the load on the wire is constant and therefore the transformation temperatures do not change during the complete forward and reverse transformation cycle. For this reason, the shape depicted in Figure 4.3 is more “vertical”. On the other hand, the spring exerts a load that increases as it is elongated due to the displacement of the SMA wire. This increasing stress causes the transformation temperatures to rise while the wire is transformed from martensite to austenite. The reverse process occurs when energy is no longer applied to the wire and it begins to cool. This variation of the transformation temperatures explains the “elongated” shape of the hysteresis loop plotted in Figure 4.4.

The influence of stress on transformation temperatures is best seen in the figure below. To obtain it, the hanging mass has been used in order to maintain a constant load during the whole M-A-M transformation cycle. Three different values have been set for the mass (1, 3 and 5 Kg) and the data generated in the three cases have been captured.

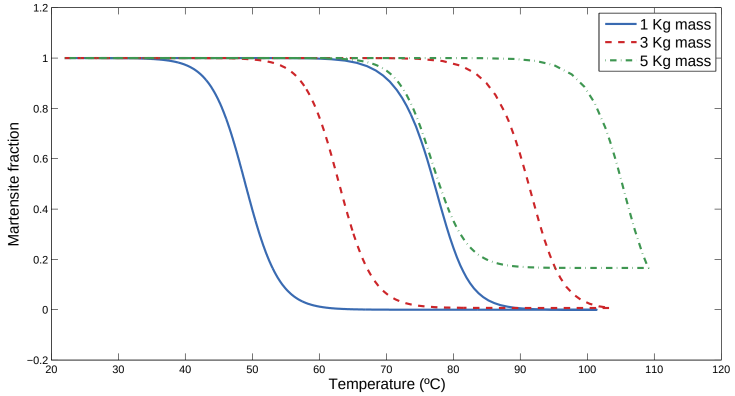

Figure 4.5: Influence of the stress of the wire on transformation temperatures.

As Figure 4.5 shows, the higher the wire load, the greater the martensite and austenite transformation temperatures, shifting the hysteresis loop to the right. This means that, for the same energy input, the phase transformation may not be completed, as occurs in the loop corresponding to the mass of 5 Kg, because the temperature of the wire no longer reaches the austenite finish temperature.

Regarding partial transformation cycles, the model also captures the phenomena of internal hysteresis loops and return-point memory, as depicted in Figure 4.6. To induce these effects, the input signal has been a series of 6 pulses of variable duration, ranging from 0.4 s to 1 s in 0.1 s increments. The time between pulses has not been enough to allow the wire to completely cool, so that both M-A and A-M transformations are partial. For this experiment, the load is provided by the bias spring preloaded to 12 N.

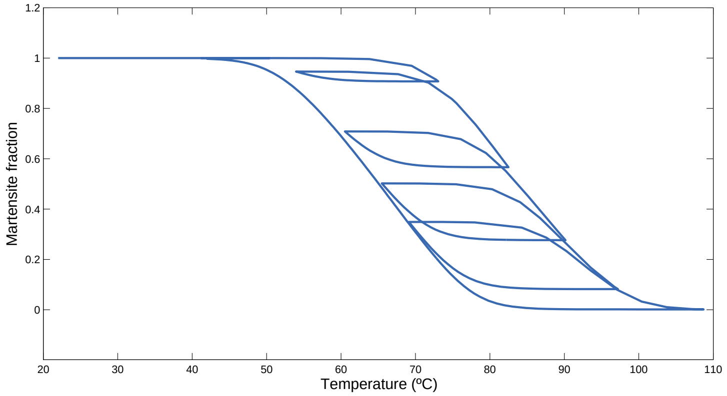

Figure 4.6: Internal hysteresis loops due to incomplete transformations.

The previous figure shows how, if the wire begins to cool before the M-A transformation is completed, the transformation is reverted and a new minor branch is formed in the hysteresis loop. Moreover, if the M-A transformation is resumed from this minor branch by heating the wire again before it completes the partial A-M transformation, it starts to follow the same the same major branch it was following before the first M-A transformation was interrupted. If the branch of the hysteresis loop is resumed at the same state in which it was left, the material exhibits the return-point memory effect. This phenomenon can be clearly seen in the two lower inner loops of Figure 4.6.

Finally, the value of the electrical resistance of the SMA wire with respect to its temperature is shown in Figure 4.7. These data have been acquired applying a current pulse of 4 A and a duration of 1.8 s, using the bias spring set to a preload force of 12 N.

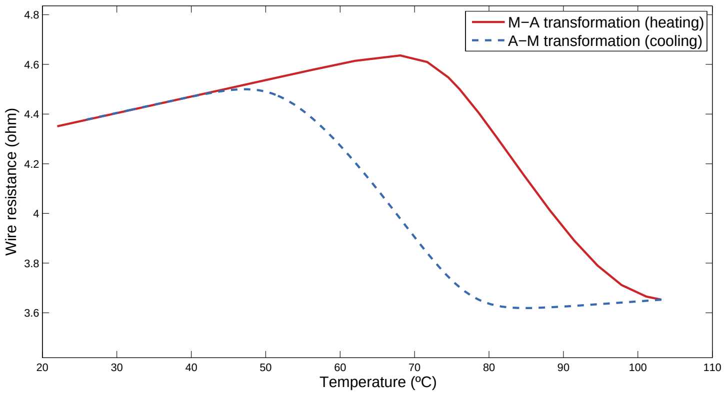

Figure 4.7: Thermal hysteresis of the electrical resistance.

From the data plotted in Figure 4.7 we can state that assuming that the resistance of an SMA wire is constant, as many models existing in the literature do, is not accurate, since it exhibits a significant thermal hysteresis. This variation in resistance as a function of temperature has a noticeable effect on the overall performance of the model. As will be discussed later, the resistance value computed by this model is very similar to the resistance value of the real wire.

Comparison between real and modeled SMA wire

For the following experiments, three different input current pulses with a duration of 1.4 s, 1.6 s and 1.8 s and an amplitude of 4 A have been used. In all three cases, the load applied to the SMA wire has been provided by the bias spring, preloaded with a force of about 12 N.

First, the position, stress and power consumption obtained by applying a pulse of 1.4 s to the real wire and to the model are plotted together in figures 4.8-4.10, respectively.

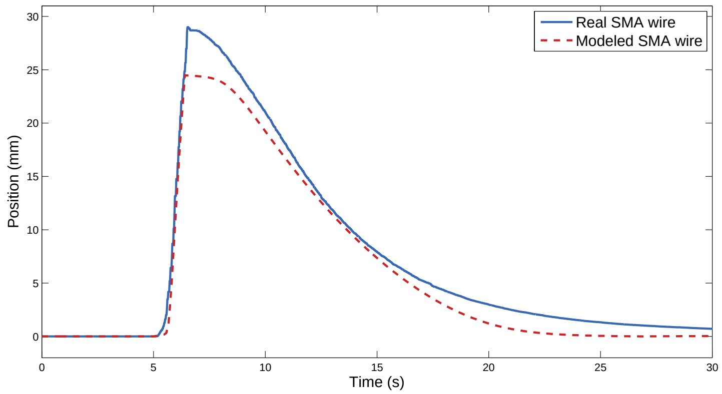

Figure 4.8: Real and modeled displacement for a 1.4 s input pulse.

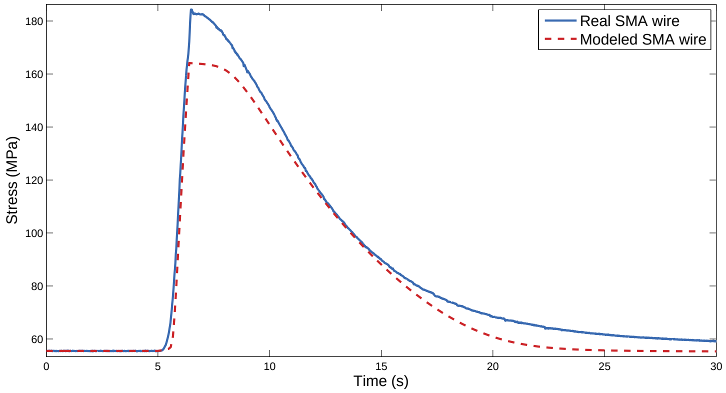

Figure 4.9: Real and modeled stress for a 1.4 s input pulse.

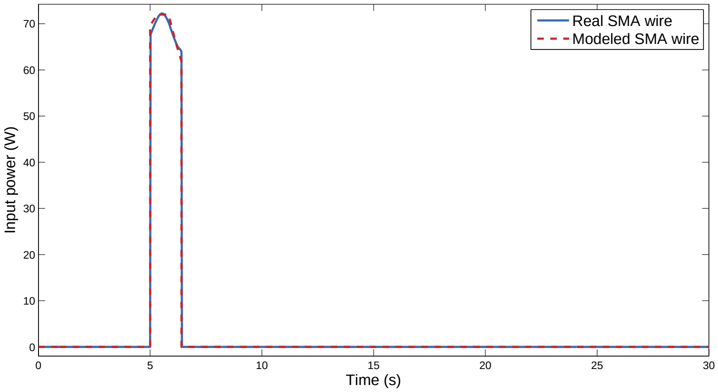

Figure 4.10: Real and modeled input power for a 1.4 s input pulse.

In this first case, the behavior of the model is quite similar to that of the real SMA wire. The heating curves are nearly identical, having the same slope (same heating rate). From the cooling curve it can be seen that, although at first the cooling rate of the model is lower than in the real case, in the last segment, the modeled rate of cooling is higher. The maximum displacement obtained with the model is less than in the case of the real wire, with an error of 4.5 mm. The same happens in the case of the stress, with an error of 20.16 MPa.

The power consumption curve deserves a closer analysis, as it is related to the electrical resistance of the SMA wire. Since the amplitude of the input current is constant, the variation of power consumption is caused by the change of the voltage drop in the wire ends, which in turn varies according to its resistance. As it can be seen in Figure 4.10, the modeled power consumption closely matches that of the real wire, which is an indication that the model accurately computes the electrical resistance value.

The plots obtained from the position, stress and power consumption data generated when a pulse of 1.6 s is applied to both the model and the real wire are shown in figures 4.11-4.13.

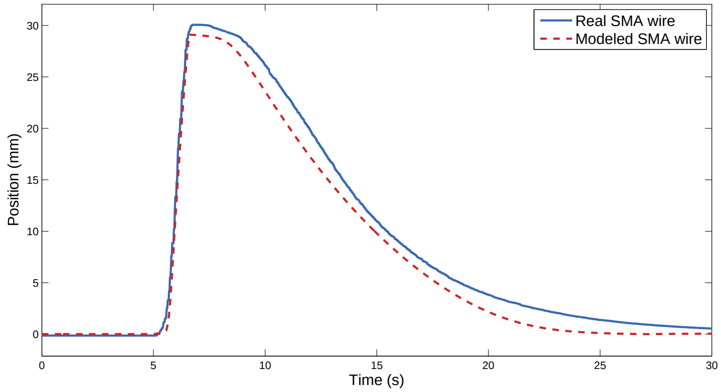

Figure 4.11: Real and modeled displacement for a 1.6 s input pulse.

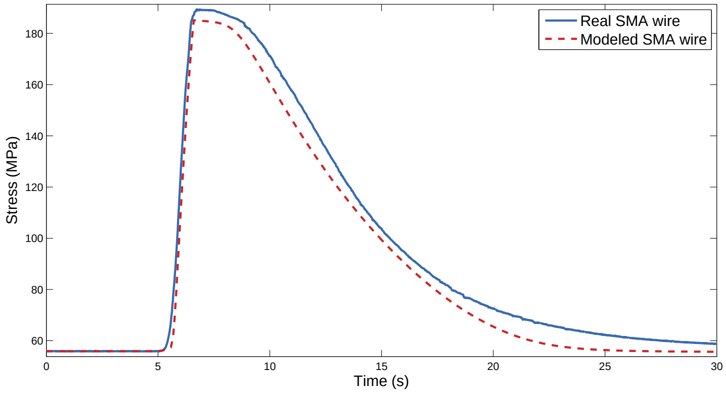

Figure 4.12: Real and modeled stress for a 1.6 s input pulse.

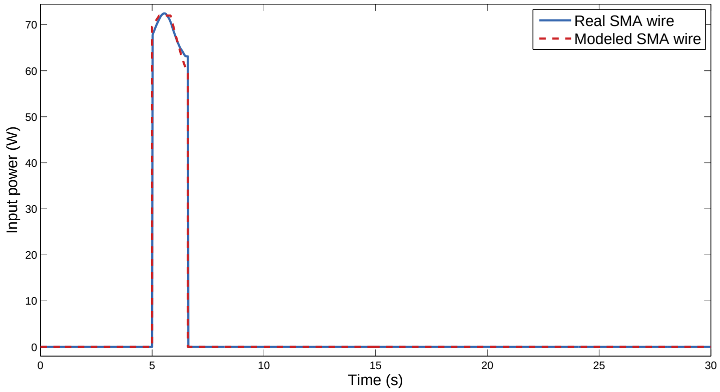

Figure 4.13: Real and modeled input power for a 1.6 s input pulse.

Compared to the previous experiment, the differences between the model and the real wire has been greatly reduced, obtaining very similar curves compared to the experimental ones. Again, the same heating rate is observed in both cases. The cooling curves are more similar in this experiment, although there are still some discrepancies, especially in the final portion of the curve in which the modeled wire is cooled faster than the real one. With respect to the maximum values, the errors between the model and the real system are very small, only 0.95 mm for the displacement and 4.2 MPa for the stress. As in the previous experiment, the power consumption curves are almost identical.

Lastly, we will analyze the performance of the real SMA wire and the model when an input pulse of 1.8 s is applied. The results of this last experiment can be seen in figures 4.14-4.16.

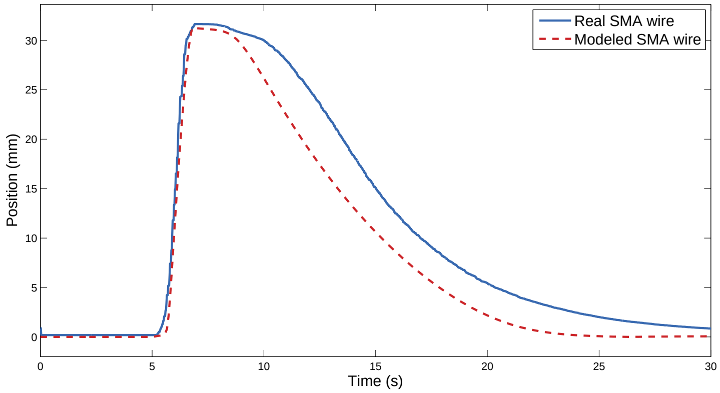

Figure 4.14: Real and modeled displacement for a 1.8 s input pulse.

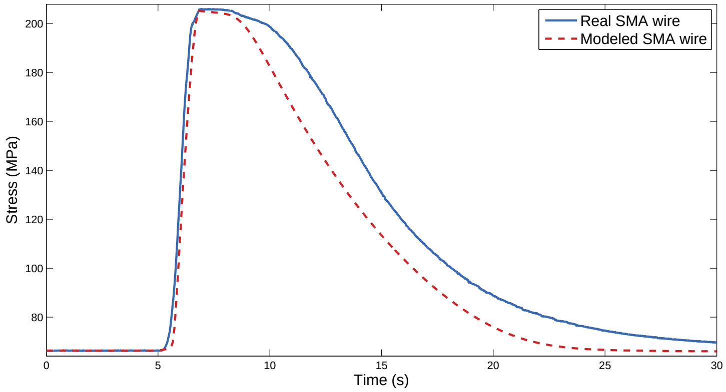

Figure 4.15: Real and modeled stress for a 1.8 s input pulse.

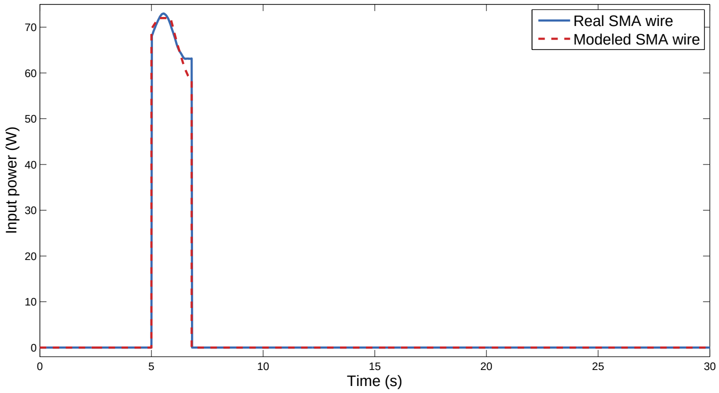

Figure 4.16: Real and modeled input power for a 1.8 s input pulse.

The behavior during heating is again very similar, but the difference between the modeled and the real cooling curves is more noticeable than in the previous experiments. The error between the maximum position and stress is the lowest of the three cases, with values of 0.38 mm and 0.73 MPa, respectively. The power consumption curves, and hence the resistance values, are still very similar, although the curve corresponding to the real wire abruptly changes to a constant value near the end of the pulse, which is possibly due to an error in the measurement system.

4.3 Conclusions

In this chapter we have presented the development of a model of the SMA wire used as the transducer of the actuator designed in this thesis. Due to the complexity and interconnection between the variables that define the behavior of these alloys, the model consists of several sub-models, each of which reproduces an aspect of the material.

In the case of the input energy model, we have considered the electrical resistance of the material as a variable that is affected by the temperature and stress and that, being dependent on the length of the wire, is also affected by its thermal hysteresis. As shown in the results, the modeled resistance accurately reproduces the response of the real resistance.

Unlike most models found in the literature, we have decided to include the effects of the latent heat of transformation in the heat transfer model. Considering that the M-A phase transformation is an endothermic process in which heat is absorbed and the A-M transformation is an exothermic process in which heat is released, we have judged that these processes can have a noticeable effect on the heating and cooling rates of the material and that they should be included for the sake of accuracy.

The phase kinetics model which computes the hysteresis loop of the SMA wire has been implemented using the Duhem differential model combined with Likhachev's scaling coefficients. As a result, the model is able to reproduce the minor hysteresis loops that occur during partial phase transformations, as well as the return-point memory effect.

The stress generated by the SMA wire has been computed using the Brinson constitutive equation in view of the good results reported in other publications. Regarding the dynamics and kinematics of the system, the models of a suspended mass and a spring have been implemented, given that these are the elements that can be attached to the SMA wire in the test bench used for the validation of the model.

The results have shown how the model is capable of reproducing many of the aspects that define SMAs, and that its behavior regarding the generated displacement and stress and its power consumption is very similar to that of a real wire.

4.4 Appendix: Convective heat transfer coefficient calculation

Assuming the SMA wire as a horizontal cylinder, its convective heat transfer coefficient is computed as follows. Let

$T_{\text{air}} = 22°C$ (air temperature)

$\rho_{\text{air}} = 1.205\frac{Kg}{m^3}$ (air density)

$\mu_{\text{air}} = 15.11 * 10^{-6}\frac{m^2}{s}$ (air viscosity)

$C_{P_{\text{air}}} = 1005\frac{J}{Kg^\circ K}$ (air specific heat capacity)

$k_{\text{air}} = 0.0257\frac{J}{smK}$ (air thermal conductivity)

$\beta_{\text{air}} = 3.047 * 10^{-3\circ}K^{-1}$ (air thermal expansion coefficient)

$T_{\text{SMA}} = 90^\circ C$ (SMA wire surface temperature in fully austenite phase)

$\varnothing_{\text{SMA}} = 0.508 * 10^{-3}m$ (SMA wire diameter)

First, the Grashof number (4.37) and the Prandtl number (4.37) are computed as:

$$\begin{aligned} Gr_{\text{SMA}} &= \tfrac{\varnothing_{\text{SMA}}^3 \rho_{\text{air}}^2 g(T_{\text{SMA}} - T_{\text{air}})\beta_{\text{air}}}{\mu_{\text{air}}^2} \\ &= 1.6947 \end{aligned} \tag{4.36}$$

$$Pr_{\text{SMA}} = \frac{\mu_{\text{air}} C_{P_{\text{air}}}}{k_{\text{air}}} = 0.591 \tag{4.37}$$

With the results from equations 4.37 and 4.37, the Rayleigh number is computed:

$$Ra_{\text{SMA}} = Gr_{\text{SMA}} Pr_{\text{SMA}} = 1.0013 \tag{4.38}$$

From this result, the Nusselt number, and hence the convective heat transfer coefficient of the SMA wire, are computed:

$$\begin{aligned} Nu_{\text{SMA}} &= (0.60 + \tfrac{0.387 * Ra_{\text{SMA}}^{1/6}}{(1 + (0.559/Pr_{\text{SMA}})^{9/16})^{8/27}})^2 \\ &= 0.8403 \end{aligned} \tag{4.39}$$

$$Nu_{\text{SMA}} = \frac{h_{\text{SMA}} \varnothing_{\text{SMA}}}{k_{\text{air}}} \Rightarrow$$

$$h_{\text{SMA}} = \frac{Nu_{\text{SMA}} k_{\text{air}}}{\varnothing_{\text{SMA}}} = 42.51\frac{W}{m^2K} \tag{4.40}$$

Chapter 5

Actuator control

In Chapter 2 we have discussed how, due to the saturated thermal hysteresis that characterizes SMAs, precise position and force control of the actuators using these alloys as transducers is difficult to achieve due to their inherent nonlinearities. As we have reviewed in Section 2.5, in the last few decades, several different control techniques have been proposed to compensate for this nonlinear behavior and ensure a robust, fast and precise position or force tracking.

In this chapter, we propose a nonlinear control technique that, to the best of our knowledge, has never been applied to control SMA actuators before. The proposed controller, called bilinear proportional-integral-derivative (BPID), belongs to the family of bilinear controllers and consists of a conventional proportional-integral-derivative (PID) controller cascaded with a bilinear compensator. Compared to most of the reviewed nonlinear control techniques, the BPID controller is simpler and easier to implement in embedded systems. This makes it especially attractive for controlling SMA-based actuation systems for wearable robots, in which the portability of their subsystems is of great importance.

The performance of the proposed BPID controller has been compared with two other controllers, a conventional PID and a commuted feedforward PI-PD, controlling the SMA actuator presented in Chapter 3. To this end, a set of five tests has been defined, in which the controlled actuator, whose output has been attached to a suspended mass, has to track a series of position references. From these tests, the position, error and control signal have been measured. From these values, a series of metrics has been computed to have quantitative measurements of the performance of each controller, in addition to plotting the position and tracking error to also have a visual assessment of their performance.

The rest of the chapter is organized as follows. The proposed control strategy along with the two control methods with which its performance is compared are detailed in Section 5.1. The experimental setup used to carry out the experiments is described in Section 5.2. The obtained results are presented in Section 5.3 and discussed in Section 5.4. Finally, the most relevant conclusions are summarized in Section 5.5.

5.1 Implemented control strategies

The control strategies that have been tested to control SMA wires are presented in this section. First, the linear PID control method from which the other two implemented controllers are derived is described. Next, the PI-PD controller, the other control technique with which the proposed BPID controller is evaluated, is also explained. Finally, the BPID control approach we propose in this thesis as a valid alternative to SMA control is introduced.

5.1.1 Linear PID control

This control strategy is the basis of the design of the other two tested controllers. In Section 5.1.2, we will see how the PI-PD controller consists of two linear controllers whose output is switched according to the value of the input position reference, whereas the proposed BPID controller is a conventional PID whose output is multiplied by an additional bilinear compensator term.

Since the design of the previous controllers derives from the basic PID, this controller has also been implemented to evaluate and compare its performance with the BPID and PI-PD. We will therefore determine whether the above controllers, especially the BPID strategy proposed in this thesis, constitute an improvement over the method on which they are based.

The PID controller in the parallel form is defined as:

$$u(t) = K_p e(t) + K_i \int_0^t e(\tau) d\tau + K_d \frac{de(t)}{dt}, \tag{5.1}$$

where the error value $e(t)$ is the difference between the desired setpoint $r(t)$ and the measured value of the controlled variable $y(t)$, K_p is the proportional gain, K_i is the integral gain and K_d is the derivative gain. To be implemented in an embedded system such as the microcontroller integrated in the control electronics described in Chapter 3, Equation 5.1 needs to be transformed into its discrete form. First, we write the PID transfer function $G(s)$ by taking the Laplace transform of Equation 5.1:

$$G(s) = K_p + \frac{K_i}{s} + K_d s \tag{5.2}$$

A well known problem of PID controllers is that, if the reference input has sharp corners (as is the case with square wave references) or there is high frequency noise in the measurements of the controlled variable caused by the sensor, the derivative term will yield large values, affecting the performance of the controller. Sometimes, this is solved by simply nullifying this term by making $K_d = 0$. However, canceling the derivative term will also cancel the “predictive” capability of the controller, which will lead to overshoot and, again, to a reduced performance. A common approach to deal with high frequency noise in the controlled variable is to add a first order low-pass filter to the derivative term, which now becomes:

$$K_d s \Rightarrow \frac{N K_d s}{s + N}, \tag{5.3}$$

where N is the location of the root of the derivative filter. Equation 5.2 then becomes:

$$G(s) = K_p + \frac{K_i}{s} + \frac{N K_d s}{s + N} \tag{5.4}$$

To obtain the discrete form of the previous transfer function, we apply the Z-transform using the backward Euler method for the integral and filtered derivative terms:

$$U(z) = \left[K_p + \frac{K_i T_s z}{z-1} + \frac{K_d N(z-1)}{(1+NT_s)z-1}\right]E(z), \tag{5.5}$$

or, equivalently,

$$U(z) = \left[K_p + \frac{K_i T_s}{1-z^{-1}} + \frac{K_d N(1-z^{-1})}{1-z^{-1}+NT_s}\right]E(z), \tag{5.6}$$

where T_s is the sampling period of the controller, in seconds. By expanding and rearranging the previous expression, Equation 5.6 can be rewritten as:

$$U(z) = \frac{b_0 + b_1 z^{-1} + b_2 z^{-2}}{a_0 + a_1 z^{-1} + a_2 z^{-2}} E(z), \tag{5.7}$$

where

$$\begin{aligned}
a_0 &= 1 + NT_s \\
a_1 &= -(2 + NT_s) \\
a_2 &= 1 \\
b_0 &= K_p(1 + NT_s) + K_i T_s(1 + NT_s) + K_d N \\
b_1 &= -[K_p(2 + NT_s) + K_i T_s + 2K_d N] \\
b_2 &= K_p + K_d N
\end{aligned} \tag{5.8}$$

Reordering Equation 5.7 we have:

$$U(z) = -\frac{a_1}{a_0} z^{-1} U(z) - \frac{a_2}{a_0} z^{-2} U(z) + \frac{b_0}{a_0} E(z) + \frac{b_1}{a_0} z^{-1} E(z) + \frac{b_2}{a_0} z^{-2} E(z), \tag{5.9}$$

which finally leads to the difference equation of the PID controller:

$$u(k) = -\frac{a_1}{a_0} u(k-1) - \frac{a_2}{a_0} u(k-2) + \frac{b_0}{a_0} e(k) + \frac{b_1}{a_0} e(k-1) + \frac{b_2}{a_0} e(k-2), \tag{5.10}$$

where k is the discrete time index, $u(k)$, $u(k-1)$ and $u(k-2)$ are the current, last and second to last samples of the control command, and $e(k)$, $e(k-1)$ and $e(k-2)$ are the current, last and second to last samples of the error.

5.1.2 Commuted feedforward PI-PD control

This control strategy, named PI-PD for simplicity, was first presented in [186] as a solution to achieve an accurate tracking of both stationary and continuously varying setpoints, such as sinusoidal and ramp position references, with an SMA-based actuator. The PI-PD controller comprises two different controllers: a PD controller and a feedforward PI controller. A commuting strategy switches between the two controllers depending on the actual and previous value of the setpoint. The output of the controller is converted to a PWM signal that regulates the current passing through the SMA wire.

The general premise of the PI-PD controller is to use one controller during the heating and cooling phases and the other one to maintain the position. If the actuator has to maintain a fixed position given by the input position reference, the PD controller (Equation 5.16) is active. When a new setpoint is given to the controller and the SMA transducer has to contract or elongate to reach this new position, the feedforward-PI controller (Equation 5.11) is automatically selected. The feedforward term of the PI controller (Equation 5.20) provides a small current to preheat the SMA wire in order to achieve a faster response. This current is only applied during the heating phase of the SMA transducer, when it has to contract to reach a new position given by the input position reference. When, to reach the commanded position, the wire has to elongate, the preheating current given by the feedforward term is not supplied.

This control architecture is shown in Figure 5.1. The PI controller is C_{PI} and the PD regulator is given by C_{PD}. The PI controller is given by the following expression:

$$u_{PI}(t) = K_{p_{PI}} e(t) + K_{i_{PI}} \int_0^t e(\tau) d\tau, \tag{5.11}$$

where $K_{p_{PI}}$ and $K_{i_{PI}}$ are the proportional and integral gains of the PI controller, respectively. The discrete form of the previous expression in the Z-domain is defined as:

$$U_{PI}(z) = \left(K_{p_{PI}} + \frac{K_{i_{PI}} T_s}{1 - z^{-1}} \right) E(z), \tag{5.12}$$

which, similarly to the discrete PID equation in Section 5.1.1, can be rewritten as:

$$U_{PI}(z) = -\frac{a_{1_{PI}}}{a_{0_{PI}}} z^{-1} U_{PI}(z) + \frac{b_{0_{PI}}}{a_{0_{PI}}} E(z) + \frac{b_{1_{PI}}}{a_{0_{PI}}} z^{-1} E(z), \tag{5.13}$$

or, alternatively,

$$u_{PI}(k) = -\frac{a_{1_{PI}}}{a_{0_{PI}}} u_{PI}(k-1) + \frac{b_{0_{PI}}}{a_{0_{PI}}} e(k) + \frac{b_{1_{PI}}}{a_{0_{PI}}} e(k-1), \tag{5.14}$$

where

$$\begin{aligned} a_{0_{PI}} &= 1 \\ a_{1_{PI}} &= -1 \\ b_{0_{PI}} &= K_{p_{PI}} + K_{i_{PI}} T_s \\ b_{1_{PI}} &= -K_{p_{PI}} \end{aligned} \tag{5.15}$$

The PD controller is defined as:

$$u_{PD}(t) = K_{p_{PD}} e(t) + K_{d_{PD}} \frac{de(t)}{dt}, \tag{5.16}$$

where $K_{p_{PD}}$ and $K_{d_{PD}}$ are the proportional and derivative gains of the PD controller, respectively. In the same fashion as the PID controller described in section 1, the PD control block includes a filtered derivative term, so the equation in the Z-domain becomes:

$$U_{PD}(z) = \left[K_{p_{PD}} + \frac{K_{d_{PD}} N(1 - z^{-1})}{1 - z^{-1} + NT_s} \right] E(z), \tag{5.17}$$

which, after expanding and rearranging the terms, has the same form as Equation 5.14:

$$u_{PD}(k) = -\frac{a_{1_{PD}}}{a_{0_{PD}}} u_{PD}(k-1) + \frac{b_{0_{PD}}}{a_{0_{PD}}} e(k) + \frac{b_{1_{PD}}}{a_{0_{PD}}} e(k-1), \tag{5.18}$$

with the following coefficients:

$$\begin{aligned} a_{0_{PD}} &= 1 + NT_s \\ a_{1_{PD}} &= -1 \\ b_{0_{PD}} &= K_{p_{PD}}(1 + NT_s) + K_{d_{PD}} N \\ b_{1_{PD}} &= -(K_{p_{PD}} + K_{d_{PD}} N) \end{aligned} \tag{5.19}$$

C_{FF} represents the offset introduced by the feedforward block. This term is ruled by the following condition:

$$u_{FF}(k) = \begin{cases} 0; & \text{if } r(k) \leq r(k-1), \\ I_{FF}; & \text{otherwise,} \end{cases} \tag{5.20}$$

where I_{FF} is a constant value that corresponds to the small current supplied to the actuator when the above condition is met.

Finally, the selector block Sel commutes the output of the controller according to the following condition:

$$u(k) = \begin{cases} u_1(k); & \text{if } r(k) \neq r(k-1) \\ u_2(k); & \text{if } r(k) = r(k-1) \end{cases} \tag{5.21}$$

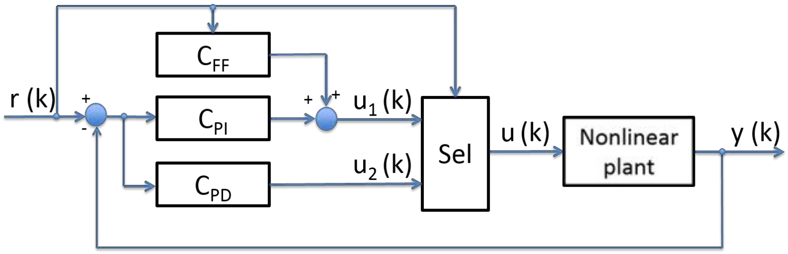

Figure 5.1: PI-PD control scheme.

5.1.3 Four term bilinear PID control

Bilinear systems are a specific type of nonlinear systems which present some interesting characteristics. The type of equation that defines these systems is simple and similar to a linear one; Bruni *et al.* defined bilinear systems as a class of "nearly linear" systems [187]. This similarity with linear systems means that many different techniques and analytical procedures already applied to the latter are also valid for bilinear systems. In addition, the nonlinear structure presents some important advantages regarding controllability, optimization and modeling. Bilinear controllers, and more specifically, the one implemented in this thesis, are a good choice to control nonlinear systems with hysteresis because of their simplicity and ease of implementation, compared with more complex strategies.

The controller implemented in this thesis is based on the research done by the Control Theory and Applications Centre at Coventry University, UK. Through several papers [188, 189, 190], the researchers develop the theory of the four-term bilinear PID (BPID) controller and its application to control the temperature of industrial furnaces. The application is completely different here, but it will be demonstrated that the same controller can be used for SMA-based actuators, yielding good results in terms of control accuracy and robustness.

The rationale behind the development of the BPID controller is that all real systems have a nonlinear behavior, which implies a reduced system performance when they are controlled with a PID controller with fixed gains. This fact is further aggravated when controlling a process over a wide operating region, which is what happens with SMA actuators. Solutions to this problem include using nonlinear control methods like gain scheduling, a technique that continuously tunes the controller gains depending on the point of operation, or the more common use of detuned PID controllers that operate over a wider range of setpoints at the cost of a sub-optimal performance [189]. The BPID controller combines the benefits of these solutions, being as simple to implement as the latter but delivering a more robust performance over a wider operating range.

For the above reasons, a BPID controller is proposed here to control SMA actuators. Specifically, this controller has been developed to control the position of the SMA linear actuator presented in Chapter 3. In this chapter, the actuator has been used to drive the linear motion of a suspended mass in a purely experimental setting, with the aim of evaluating the performance of the BPID control approach. In Chapter 6, we will further assess whether this control scheme can be used to control a real wearable device: a soft hand exoskeleton powered by an actuation system based on the actuator described in Chapter 3.

Bilinear systems can be considered as a specific type of nonlinear systems characterized by the following dynamic equation [191]:

$$\begin{cases} \dot{x}(t) = \mathbf{A}\mathbf{x}(t) + \mathbf{b}u(t) + u(t)\mathbf{N}\mathbf{x}(t), \\ y(t) = \mathbf{c}^{\mathrm{T}}\mathbf{x}(t), \end{cases} \tag{5.22}$$

where $\mathbf{x} \in \Re^n$ is the state vector, $u, y \in \Re$ are the control input and process output variables, respectively, $\mathbf{A}$ is a $n \times n$ matrix of real constants, $\mathbf{b}$ is a $n \times 1$ vector of real constants, $\mathbf{N}$ is a $n \times n$ matrix of real constants that contains the bilinear coefficients, and $\mathbf{c}$ is a $n \times 1$ output vector of real constants. These matrices are defined as [192]:

$$\begin{gathered} \mathbf{A} = \begin{bmatrix} 0 & 1 & \dots & \dots & 0 & 0 \\ 0 & 0 & \dots & \dots & 0 & 0 \\ \dots & \dots & \dots & \dots & \dots & \dots \\ \dots & \dots & \dots & \dots & 1 & 0 \\ 0 & 0 & \dots & \dots & 0 & 1 \\ -\alpha_0 & -\alpha_1 & \dots & \dots & -\alpha_{n-2} & -\alpha_{n-1} \end{bmatrix} \quad \mathbf{b} = \begin{bmatrix} 0 \\ 0 \\ \dots \\ \dots \\ 0 \\ 1 \end{bmatrix} \\ \mathbf{N} = \begin{bmatrix} 0 & 0 & \dots & \dots & 0 & 0 \\ 0 & 0 & \dots & \dots & 0 & 0 \\ \dots & \dots & \dots & \dots & \dots & \dots \\ \dots & \dots & \dots & \dots & 0 & 0 \\ 0 & 0 & \dots & \dots & 0 & 0 \\ \rho_0 & \rho_1 & \dots & \dots & \rho_{n-2} & \rho_{n-1} \end{bmatrix} \qquad \mathbf{c}^{\mathrm{T}} = \begin{bmatrix} \beta_0 & \dots & \beta_m & \dots & 0 \end{bmatrix} \end{gathered} \tag{5.23}$$

If we rearrange the terms in Equation 5.22, we have that a single-input single-output (SISO) bilinear system can be defined as:

$$\dot{x} = [\mathbf{A} + u(t)\mathbf{N}]\mathbf{x}(t) + \mathbf{b}u(t), \tag{5.24}$$

which clearly shows that the dynamic and steady-state response of a bilinear system are input dependent. When controllability is analyzed, the input controls the state evolution not only additively by means of the term $\mathbf{b}u(t)$, but also in a multiplicative way by means of the term $u(t)\mathbf{N}\mathbf{x}(t)$. This combination of control approaches can result in a more effective control action in some cases. For example, some researchers have concluded that a linear system with input amplitude constraints is, in general, not controllable. However, such a system can be controlled by adding a multiplicative control law [191, 193]. This class of systems presents interesting properties; the type of nonlinearity shown in Equation 5.24 is simple and close to a linear system. This fact allows the application of many techniques and analytical procedures already available for linear systems.

In [188], a first order bilinear model is given in the following continuous representation form:

$$\dot{y} = -\alpha_0 y + \beta_0 u + \rho_0 u y, \tag{5.25}$$

that can be rearranged as:

$$\dot{y} = (-\alpha_0 + \rho_0 u) y + \beta_0 u, \tag{5.26}$$

which can be regarded as a system with an operating point dependent pole $-(\alpha_0 - \rho_0 u)$ and a steady-state gain [188, 189]. From this equation, it can be deduced that, for a given input u, the steady-state output Y_{SS} of a SISO bilinear system of any order is given by the following nonlinear relationship [194]:

$$Y_{\mathrm{SS}} = \frac{\beta_0 u}{\alpha_0 - \rho_0 u} \tag{5.27}$$

In Figure 5.2, the steady-state input/output relationship defined by Equation 5.27 is represented graphically depending on the value of ρ_0.

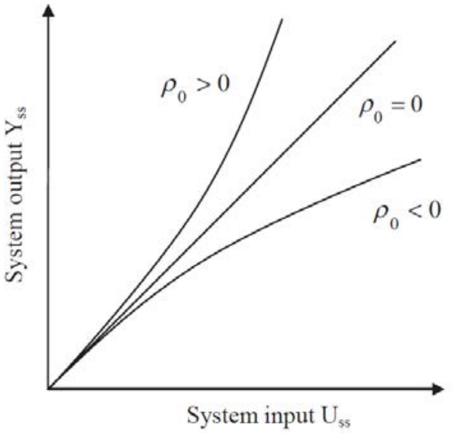

Figure 5.2: Steady-state input/output relationship of a bilinear system [190] (reproduced with the permission of the authors).

As has been stated above, bilinear systems of the form of Equation 5.24 are very close to linear ones, which can be observed in Figure 5.2; when the bilinear term ρ_0 is zero, the steady-state input/output relationship corresponds to that of a linear system, so it can be said that linear systems are a special subclass of bilinear systems. The curve corresponding to positive values of ρ_0 represents those systems in which the gain increases as the input increases, such as exothermic processes. On the other hand, negative values of the bilinear term lead to systems in which an increase of the input produces a decrease of the gain, eventually resulting in a saturated output. This type of response can be found in many industrial processes, and corresponds to the behavior of an SMA-based actuator, in which an increase of the input energy will not further produce an output deformation or force after reaching the maximum strain of the SMA element. For this reason, we have considered that a bilinear control approach would be appropriate to control actuators that use an SMA component as the transducing element.

As we have done with the PID and PI-PD controllers, Equation 5.24 needs to be discretized. According to [195], a first order SISO bilinear system can be discretized as:

$$y(k) = -\alpha_{0_d} y(k-1) + \beta_{0_d} u(k-1) + \rho_{0_d} u(k-1) y(k-1), \tag{5.28}$$

where $y(k)$ represents the current state in the discrete-time domain, $y(k-1)$ and $u(k-1)$ are the previous samples of the output and input, respectively, and α_{0_d}, β_{0_d}, and ρ_{0_d} are the discrete model parameters, defined as:

$$\begin{aligned} \alpha_{0_d} &= -e^{-\alpha_0 T_s h}, & \beta_{0_d} &= \frac{\beta_0}{\alpha_0}\left[1 - e^{-\alpha_0 T_s h}\right], \\ \rho_{0_d} &= \frac{\rho_0}{\alpha_0}\left[1 - e^{-\alpha_0 T_s h}\right], \end{aligned} \tag{5.29}$$

where T_s is the sampling time in seconds and h is an input dependent correction coefficient given by:

$$h = -\frac{1}{\alpha_0 T_s} \ln\left[\frac{\alpha_0 e^{-\alpha_0 T_s h} - \rho_0 u}{\alpha_0 - \rho_0}\right], \tag{5.30}$$

or equivalently,

$$h \approx 1 + \frac{\rho_0 T_s u}{2} \tag{5.31}$$

As mentioned before, the BPID controller consists of a linear PID controller whose output is connected to a bilinear compensator, as Figure 5.3 illustrates. The addition of the bilinear compensator results in a certain linearization of the nonlinear plant, making it possible to apply a standard linear controller without decreasing the control performance. To find an expression for the input u that cancels the bilinear term, thus linearizing the system, Equation 5.28 is first rearranged as follows:

$$y(k) = -\alpha_{0_d} y(k-1) + \beta_{0_d}\left[1 + \frac{\rho_{0_d}}{\beta_{0_d}} y(k-1)\right] u(k-1) \tag{5.32}$$

To linearize the above expression, we can apply the feedback linearization method by defining a compensated control input v that cancels the bilinear term. Equation 5.32 is then reformulated as:

$$y(k) = -\alpha_{0_d} y(k-1) + \beta_{0_d}\left[1 + \frac{\rho_{0_d}}{\beta_{0_d}} y(k-1)\right] v(k-1), \tag{5.33}$$

and the bilinear compensator that linearizes Equation 5.32 is defined as:

$$v(k-1) = \frac{1}{1 + K_b y(k-1)} u(k-1), \tag{5.34}$$

where $K_b = \rho_{0_d}/\beta_{0_d}$ is the tuning parameter.

By substituting Equation 5.34 in Equation 5.33, it can be observed that the system dynamics is now linear:

$$y(k) = -\alpha_{0_d} y(k-1) + \beta_{0_d} u(k-1) \tag{5.35}$$

After that, the linearized system can be controlled by a traditional linear technique such as a PID controller. To ensure the operation of the controller at the setpoint $r(k)$, the bilinear compensator in Equation 5.34 is modified to include a numerator term that cancels the compensation effect effect when the controlled variable is at the desired reference. The final form of the bilinear compensator is therefore:

$$\frac{1 + K_b r(k)}{1 + K_b y(k-1)}, \tag{5.36}$$

where $r(k)$ is the setpoint at which the PID controller was tuned, which in this case is the target position of the SMA actuator.

As said before, the final structure of the BPID approach is a four-term controller comprising the three-term PID controller (as defined in Equation 5.10) whose output is multiplied by the additional bilinear term given by Equation 5.36. This simple architecture is displayed in Figure 5.3. The bilinear term of Equation 5.36 is introduced in the bilinear compensator block. As in the previous cases, the output of the controller is limited to a range between 0 and 100, so it can be used as the duty cycle of a PWM signal that adjusts the current flowing through the actuator.

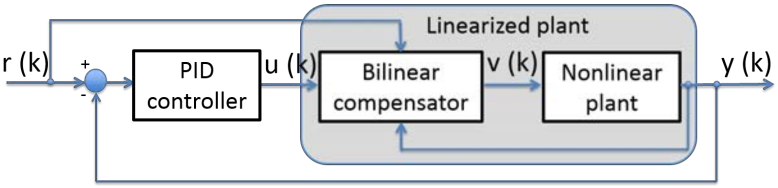

Figure 5.3: BPID control scheme.

5.2 Experimental setup

A set of five tests has been designed to compare the performance of the proposed BPID controller with that of the other two controllers described above. The aim of these experiments is to evaluate the suitability of the BPID technique in controlling the displacement of SMA-based actuators, more specifically, the flexible SMA actuator presented in Chapter 3. The tests are designed to study the behavior of the controllers in different situations: performing smooth and continuous motions at different speeds, undergoing small position variations as well as abrupt position changes, and maintaining a constant position. These behaviors are given by five position references, one for each test, that the actuator has to track as accurately as possible. For each controller, a total of fifteen experiments, three repetitions of each defined test, have been conducted.

The physical setup used to perform the experiments is the same than the one used to characterize the actuator, described in Section 3.3.1. To power the actuator, it has been connected to one of the channels of the driver described in Section 3.2.1. The three control algorithms that are going to be evaluated have been implemented in the control electronics featured in Section 3.2.2, which is also in charge of sending all data related to the performance of the controllers to a PC for further analysis.

In this case, the mechanism of the test bench that allows bending the actuator has not been used, keeping it straight during all the control tests. The linear position sensor installed in the test bench has been used to obtain the position feedback for the control algorithms. For the aforementioned actuator characterization tests, the bias force of the SMA transducer was provided by a suspended mass and by an additional spring acting as an interface between the output of the actuator and a load cell. During the control experiments, no force measurement has been taken, so the output of the actuator is only connected to a suspended mass exerting an axial static load of 40 N on the SMA wire. The general scheme of the experimental setup is shown in Figure 5.4, where the blue lines correspond to data connections, the red lines represent electrical connections and the black lines are mechanical connections.

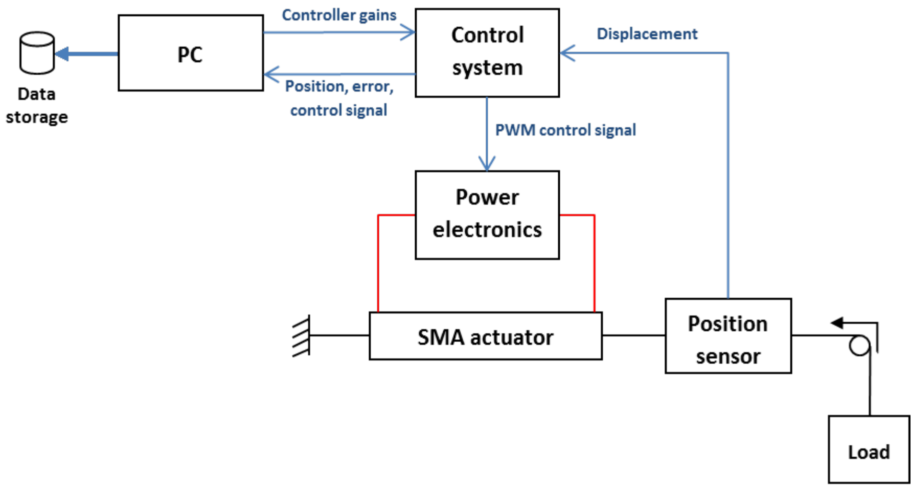

Figure 5.4: Experimental setup scheme

The following position references have been used to test and compare the performance of the three controllers:

- Sinusoidal reference: three sinusoidal signals with an amplitude of 20 mm peak-to-peak at three different frequencies (0.125 Hz, 0.25 Hz and 0.5 Hz) are applied during 20 s to test the performance of the controllers when following a continuously varying reference at different speeds. For the sake of brevity, only the results of the tests performed with the 0.125 Hz sinusoidal references will be plotted. Numerical results of the tests performed with the three sinusoidal references are summarized in subsection 5.3.4.

- Step reference: two step signals with an amplitude of 20 mm, a pulse width of 5 s and separated by a 30 s interval, are applied to test the behavior of the controlled actuator when it is subjected to a sudden and large position variation and to study its operation in the stationary portion of the reference.

- Incremental step reference: the position reference is increased in steps with an amplitude 5 mm, from 0 to 20 mm. From this position, the actuator is returned to the starting position in decrements of 5 mm. This test is intended to check the performance of the controlled actuator when it is subjected to small position changes, as well as its stationary behavior at different amplitudes.

The values of the gains of the controllers, adjusted for the completion of the tests described above, are shown in Table 5.1. These gains have been obtained experimentally by a trial and error process, tuning the values and observing the response of the actuator in real time. According to Lan *et al.* [196], the nonlinear behavior of SMAs requires different PID gain values to obtain the best controller response in the different thermal paths of the material. This means that a controller adjusted with established gain-tuning rules, such as the Ziegler-Nichols method, may not deliver the most optimal performance in a wide range of operation. Gédouin *et al.* [152] also consider that PID tuning algorithms cannot be applied in the case of SMA control, due to the slow dynamics of the plant as well as the lack of control during the elongation of the transducer (when caused by a passive bias force and free air convection). For these reasons, we have considered that manually tuning the gains will result in a better controller performance, despite being a more time-consuming method.

Strategy	K_p	K_i	K_d	K_b
BPID	0.8	0	0.05	1

Strategy	$K_{p_{PI}}$	$K_{i_{PI}}$	$K_{p_{PD}}$	$K_{d_{PD}}$	u_{FF}
PI-PD	0.8	0.25	0.08	0.003	3

Strategy	K_p	K_i	K_d
PID	0.8	0	0.05

Table 5.1: Controller gains

For each performed test, data provided by the position sensor of the test bench along with data generated by the control electronics have been captured for further analysis. In terms of controlling SMA actuators, some parameters are especially important to study the performance of an algorithm. Focusing on the most relevant information, the following graphical data will be shown as the results of every experiment, as well as some figures of merit processed from the recorded data:

- Position - time plot.
- Error - time plot.
- Root Mean Squared Error (RMSE).
- Integrated Absolute value of the Error (IAE).
- Mean Absolute Control Signal Increment (MACSI).
- Average power consumption (APC).

5.3 Results

5.3.1 PID

Figures 5.5, 5.6 and 5.7 show the results of the PID controller tracking the sinusoidal, step and incremental step references, respectively.

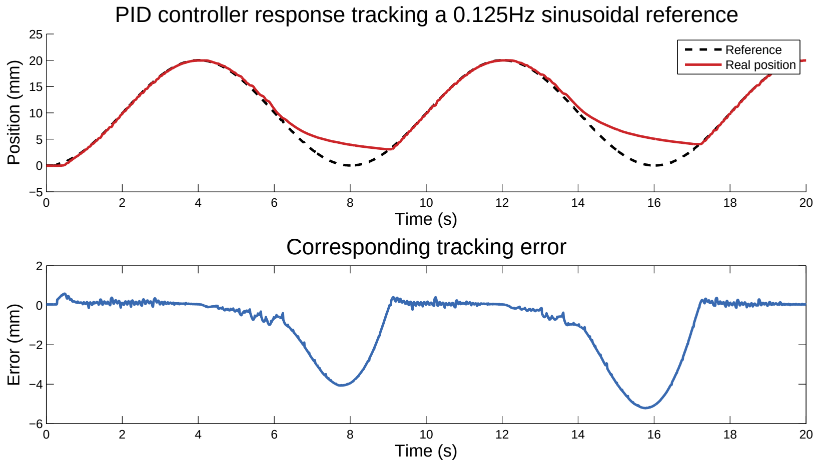

Figure 5.5: Actuator position and error for the PID controller tracking a 0.125 Hz sinusoidal reference

The response of the controller is not bad, taking into account that this is a linear controller driving a nonlinear actuator. The tracking performance during the ascending parts of the reference is good, with only a small overshoot of 0.3 mm and close to the reference. There is a point during the descending parts of the actuation cycle beyond which the actuator is not able to follow the reference, due to the cooling time of the SMA wire.

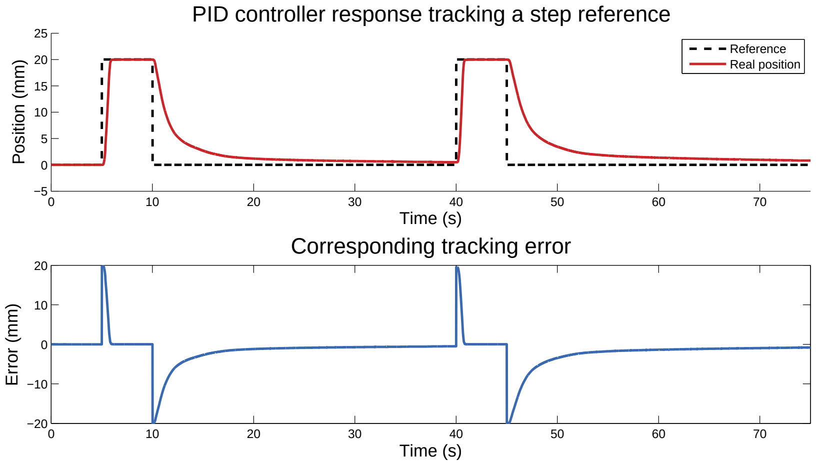

Figure 5.6: Actuator position and error for the PID controller tracking a step reference

Regarding the performance of the PID controller tracking a step reference (Figure 5.6), a surprisingly good behavior is observed again. The response of the controller is fast (it takes 1.2 s to reach the desired position) and there is no overshoot when reaching the reference. Also, the steady-state error is small, about 0.02 mm, which is a 0.1 % of the total commanded displacement.

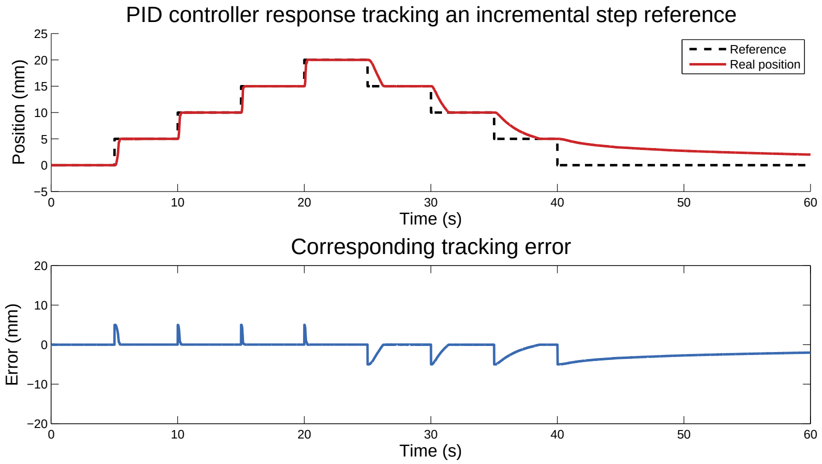

Figure 5.7: Actuator position and error for the PID controller tracking an incremental step reference

In the case of the incremental step reference (Figure 5.7), the controller shows a performance very similar to the one of the previous test. There is an almost imperceptible overshoot in some of the ascending steps of the reference, but the overall behavior is good, with steady-state errors of about 5 μm, a 0.1 % of the position increments.

5.3.2 PI-PD

Figures 5.8, 5.9 and 5.10 show the results of the PI-PD controller tracking the sinusoidal, step and incremental step references, respectively.

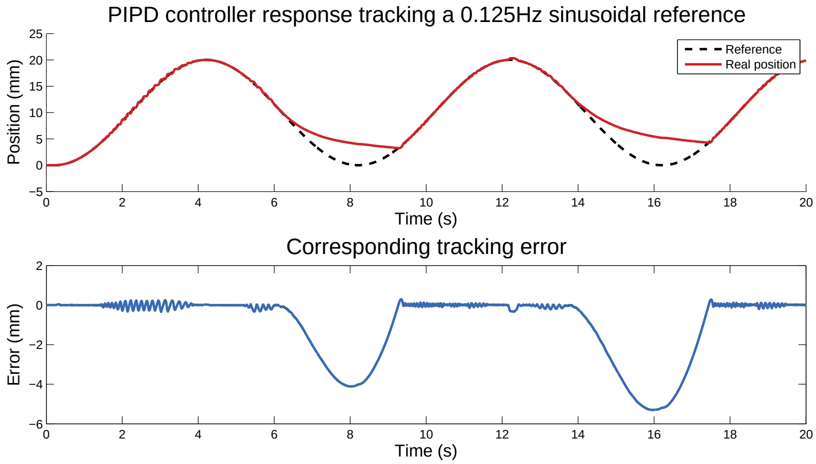

Figure 5.8: Actuator position and error for the PI-PD controller tracking a 0.125 Hz sinusoidal reference

The controller exhibits noticeable oscillations around the reference during the ascending parts; the amplitude of the error is about 0.5 mm. These results are slightly worse than the ones obtained in [186], where this controller was first presented. These worse results are due to some differences between the experiments conducted in that previous work and the ones described here. In the first place, the SMA wires used in the cited paper were shorter and with a smaller diameter, all of which result in a smaller thermal inertia. In addition, the suspended mass actuated by the the SMA wire was lighter, which implies, among other things, that the transformation temperatures of the material were lower than in the present experiments. But the main reason lies on one of the disadvantages of the PI-PD controller. Being a combination of two different controllers, one for the transient part of the actuation and the other one for the stationary part, different gains can be adjusted to obtain an optimal performance for each of these cases. That is, one set of gains can be used to optimize the behavior of the actuator for sinusoidal references, eminently transient, and a different set of gains can be tuned for step references, where the stationary behavior predominates. In order not to give this controller an advantage over the other two during the experiments, the same set of gains has been used for all five tests. It is for this reason that the obtained results are not as good as the ones shown in the referenced work.

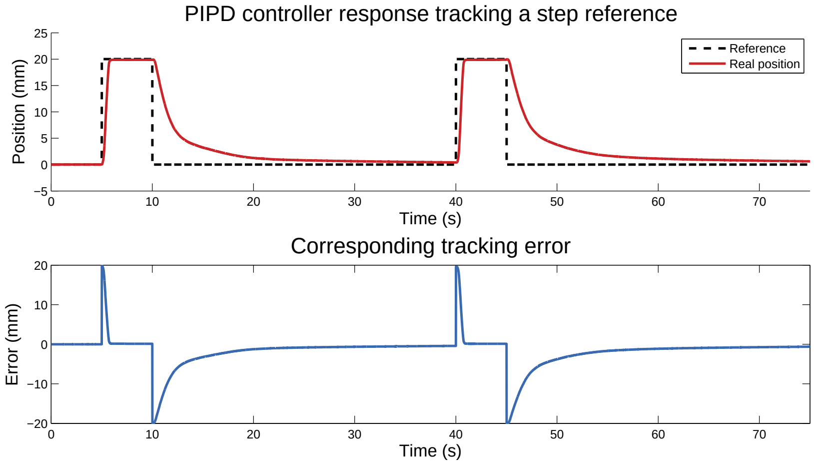

Figure 5.9: Actuator position and error for the PI-PD controller tracking a step reference

The PI-PD controller performs well on the step reference (Figure 5.9). It shows no overshoot, despite the fact that its response is fast (1.1 s to reach the reference), and the steady-state error has a value of about 0.12 mm, which is a 0.6 % of the total actuator displacement.

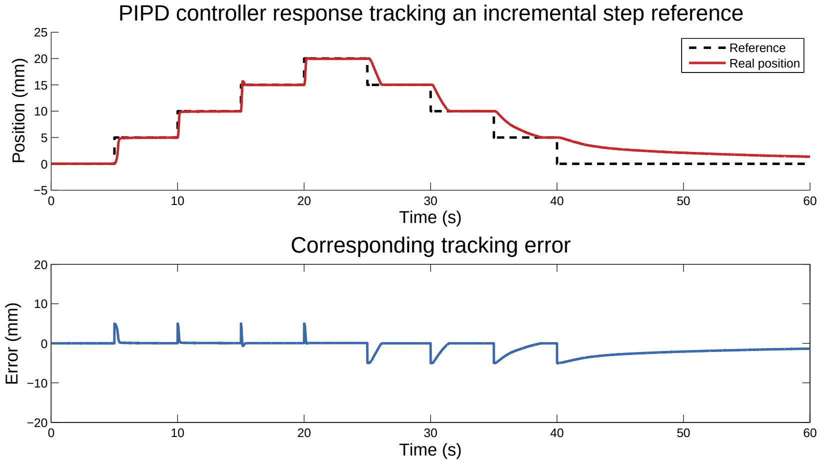

Figure 5.10: Actuator position and error for the PI-PD controller tracking an incremental step reference

Tracking the incremental step reference (Figure 5.10), the controlled actuator shows a similar behavior to the one obtained tracking the step reference. However, in this case there are some steps where there is overshoot, with an amplitude reaching a value of 0.7 mm (a 14 % of the position variations). The steady-state error has a mean value of 0.05 mm, a 1 % of the amplitude of the steps.

5.3.3 BPID

Figures 5.11, 5.12 and 5.13 show the results of the BPID controller tracking the sinusoidal, step and incremental step references, respectively.

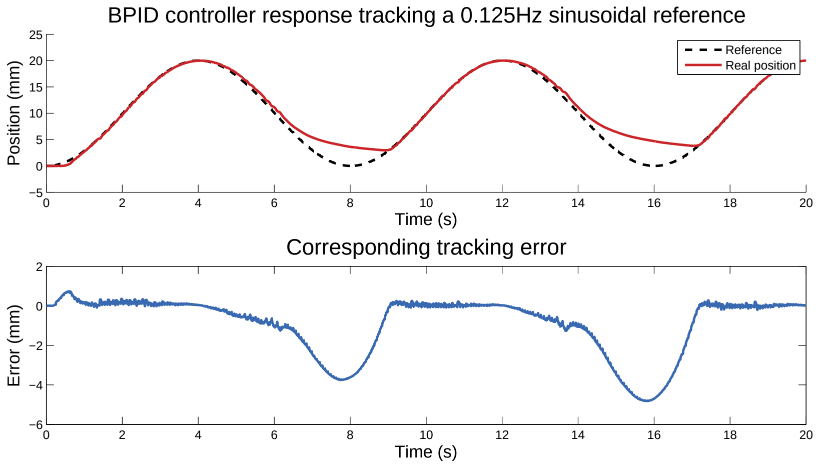

Figure 5.11: Actuator position and error for the BPID controller tracking a 0.125 Hz sinusoidal reference

The behavior of the BPID controller tracking sinusoidal references is very similar to the one observed using the PID controller. The position of the actuator oscillates around the reference during the ascending parts, with an amplitude of 0.2 mm. Again, due to the thermal nature of the actuator, there is a final portion of the descending parts of the actuation cycle that the controller is not able to track.

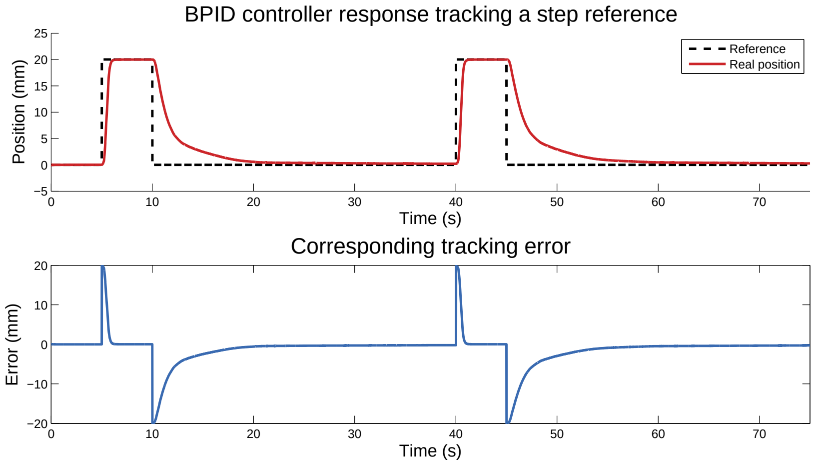

Figure 5.12: Actuator position and error for the BPID controller tracking a step reference

It can be seen that the controller performs very well when tracking step references (Figure 5.12), although it is the slowest of the three controllers, taking 1.4 s to reach the desired position. The response is very smooth when reaching the reference, with no overshoot. The steady-state error is about 0.02 mm, a 0.1 % of the displacement.

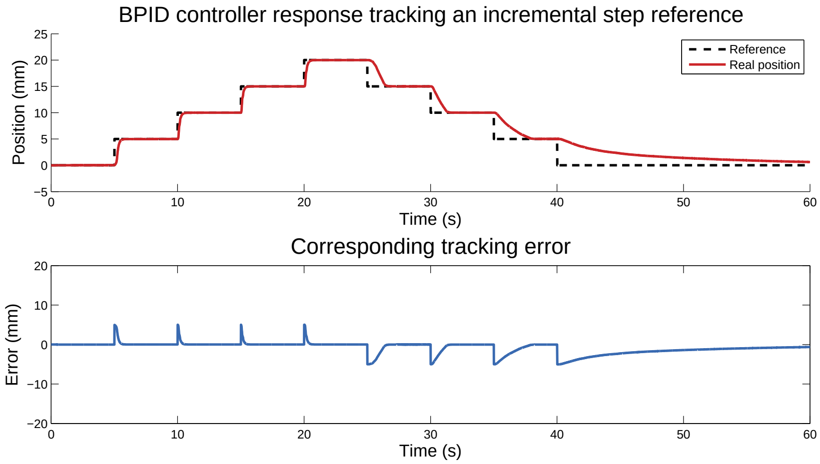

Figure 5.13: Actuator position and error for the BPID controller tracking an incremental step reference

With respect to the case of the controlled actuator tracking the incremental step reference (Figure 5.13), the performance is very good. In fact, it is the best of the three controllers for this case. Unlike the PID and the PI-PD controllers, the BPID shows no overshoot in any of the steps of the reference. The value of the steady-state error is about 0.01 mm, which is a 0.2 % of the position increments.

5.3.4 Figures of merit

In this section, the different metrics used to quantitatively compare the performance of the three implemented controllers during the completion of the different tests, will be shown. These metrics will help assessing if the proposed BPID controller has some advantages when compared with the other two tested controllers.

Root mean squared error (RMSE)

RMSE is a very common value to assess the performance of a controller. It measures the square root of the average of the square of all the errors over the duration of the control test. Compared with the similar Mean Absolute Error, the RMSE amplifies and severely punishes large errors. The RMSE is computed as:

$$RMSE = \sqrt{\frac{1}{n}\sum_{i=1}^{n}[y_{ref}(i) - y(i)]^2} \tag{5.37}$$

Controller	**Reference type**				
	0.125 Hz sine	**0.250 Hz sine**	**0.500 Hz sine**	**Step**	**Incremental step**
PID	1.71 mm	4.25 mm	7.66 mm	4.40 mm	1.96 mm
PI-PD	1.95 mm	3.87 mm	6.50 mm	4.27 mm	1.75 mm
BPID	1.72 mm	3.51 mm	7.08 mm	4.10 mm	1.58 mm

Table 5.2: Root mean squared error

Integrated absolute value of the error (IAE)

The IAE gives a measure of the cumulative error over the duration of the control test. In this way, both large and small errors are taken into account. The IAE is computed as:

$$IAE = \int_{t=0}^{t=T} |y_{ref}(t) - y(t)|dt \tag{5.38}$$

Controller	**Reference type**				
	0.125 Hz sine	**0.250 Hz sine**	**0.500 Hz sine**	**Step**	**Incremental step**
PID	$1.95 * 10^3$ mm	$5.85 * 10^3$ mm	$11.79 * 10^3$ mm	$1.81 * 10^4$ mm	$7.33 * 10^3$ mm
PI-PD	$2.05 * 10^3$ mm	$5.01 * 10^3$ mm	$9.44 * 10^3$ mm	$1.62 * 10^4$ mm	$6.41 * 10^3$ mm
BPID	$2.06 * 10^3$ mm	$4.79 * 10^3$ mm	$10.72 * 10^3$ mm	$1.30 * 10^4$ mm	$5.42 * 10^3$ mm

Table 5.3: Integrated absolute value of the error

Mean absolute control signal increment (MACSI)

The MACSI provides a measurement of how abrupt is the control signal that commutes the power of the SMA actuators. A more abrupt control signal (a control signal that has greater increments from one sample to the next) will impose greater variations of electrical power on the SMA actuator, which might shorten its service life. The MACSI is computed as:

$$MACSI = \frac{1}{n-1}\sum_{i=1}^{n-1} |u(i+1) - u(i)| \tag{5.39}$$

Controller	**Reference type**				
	0.125 Hz sine	**0.250 Hz sine**	**0.500 Hz sine**	**Step**	**Incremental step**
PID	14.13	8.81	6.24	0.71	1.92
PI-PD	9.73	4.88	2.89	0.24	0.68
BPID	21.69	8.37	5.44	1.87	5.83

Table 5.4: Mean Absolute Control Signal Increment

Average power consumption (APC)

The average power consumed by the actuator for each controller during the different tests has been measured. To compute it, the RMS value of the control signal (which is the duty cycle of a PWM signal) has been multiplied by the maximum squared current to which the power supply of the SMA actuator has been limited (4 A) and by the resistance of the SMA wire (4.2 Ω):

$$APC = \frac{\sqrt{\frac{1}{n}\sum_{i=1}^{n} u(i)^2}}{100} * I^2 * R_{SMA} \tag{5.40}$$

Controller	**Reference type**				
	0.125 Hz sine	**0.250 Hz sine**	**0.500 Hz sine**	**Step**	**Incremental step**
PID	30.62 W	31.54 W	33.64 W	10.87 W	9.04 W
PI-PD	25.23 W	29.83 W	32.04 W	10.56 W	8.23 W
BPID	32.56 W	33.62 W	35.41 W	11.46 W	10.99 W

Table 5.5: Average power consumption

5.4 Discussion

Once the results of every controller have been presented, the performance of every one must be analyzed in order to determine if the BPID controller is a viable alternative to control SMA actuators. In this section, the results of the three controllers are analyzed and compared. This comparative study will help to draw a conclusion on the validity of the control method proposed in this thesis.

Regarding the sinusoidal references, the performance of each controller is very similar. However, the PI-PD controller has a greater overshoot around the reference than the other two controllers, especially when tracking 0.125 Hz and 0.25 Hz sinusoidal signals. In contrast, this controller is able to track the reference during the descending part of the sine more accurately than the other two controllers (Figure 5.14). The PID and BPID controllers have some delay at the start of the tests performed with the 0.25 Hz and 0.5 Hz references. In the three cases, the actuator is not able to track the final portion of the sinusoidal reference due to its cooling time, which is more noticeable in the case of the 0.5 Hz reference.

The RMSE and IAE values suggest that the BPID is slightly better than the other two controllers tracking sinusoidal references. The greatest difference is observed in the case of the 0.25 Hz reference, in which the BPID controller achieves the best performance. For the 0.5 Hz reference, the PI-PD controller has better RMSE and IAE values than the PID and BPID because the latter follow the ascending part of the reference with some delay, whereas the greater response speed of the PI-PD controller allows a more accurate tracking at this higher actuation frequency.

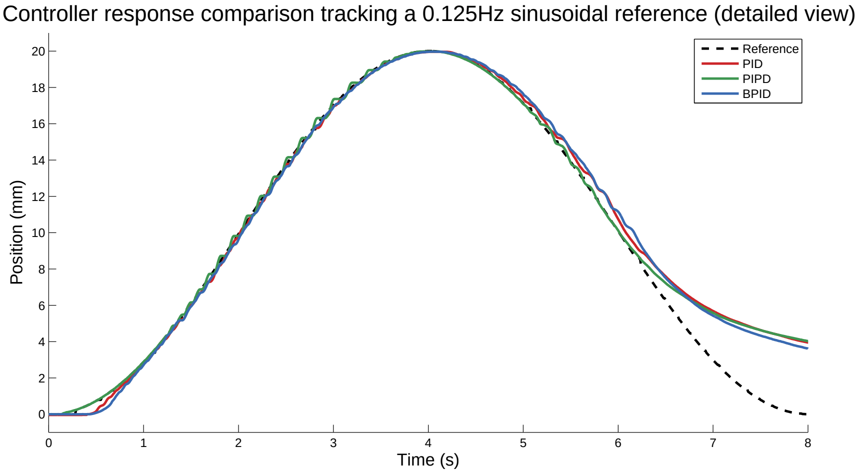

Figure 5.14: Detailed view of the PID, PI-PD and BPID tracking a 0.125 Hz sinusoidal reference

Comparing the results of the step reference, the performance of the three controllers is apparently the same, with no overshoot when reaching the reference. The steady-state error of the PID and BPID is practically the same, and smaller than the one of the PI-PD. The fastest controller reaching the reference is the PI-PD, although, during the descending part of the actuation, the BPID controller is faster than the other two, because it stops delivering power to the actuator earlier that the other two controllers. When looking at a detailed view of the ascending part of the actuation, some more differences can be seen (Figure 5.15).

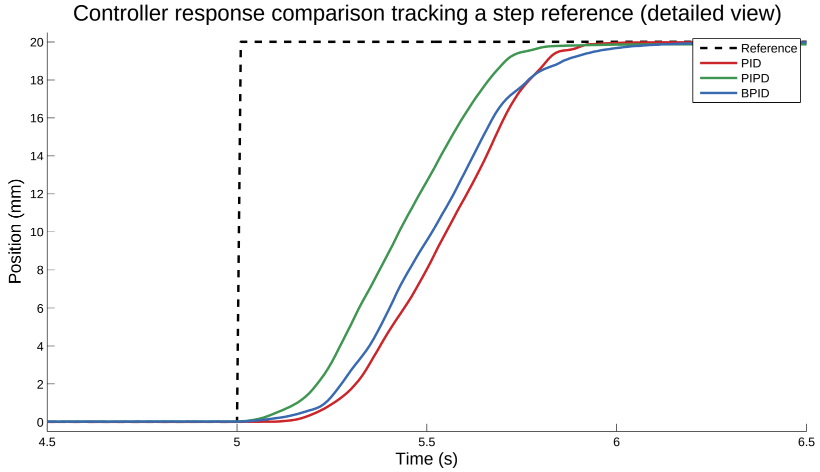

Figure 5.15: Detailed view of the PID, PI-PD and BPID tracking a step reference

The response of the PI-PD controller is faster than the other two controllers, reaching the reference earlier than the PID and the BPID. Due to the effect of the bilinear compensator, whose value becomes smaller as the position of the actuator approaches the reference, the speed of the SMA actuator when reaching the reference starts to decrease earlier than in the case of other two controllers, and it does so in a more gradual way. This effect of the bilinear term is very advantageous in cases like this, in which there is a sudden change of position, since it prevents overshoot.

With regard to the tests performed with the incremental step reference, the response of the three controllers is very similar. The BPID controller is again the fastest during the descending part of the actuation. A detailed view of the response of the controllers reveals more differences (Figure 5.16).

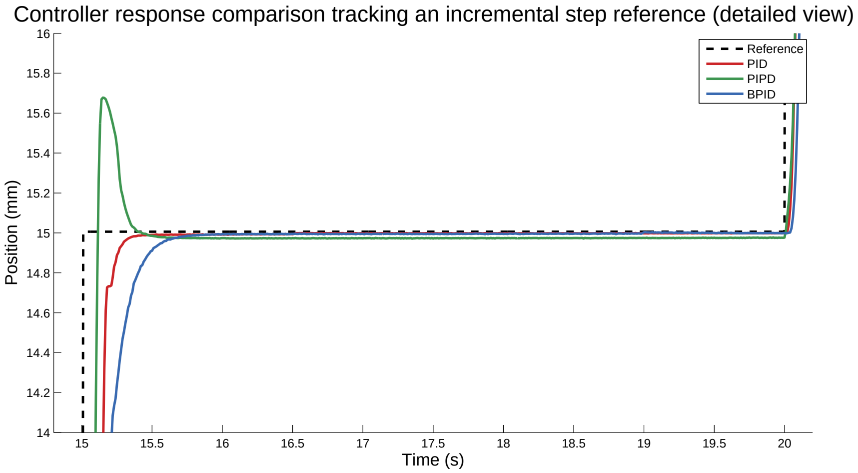

Figure 5.16: Detailed view of the PID, PI-PD and BPID tracking the third step of the incremental step reference

The PI-PD controller is the fastest of the three, but it has some overshoot (0.7 mm) when reaching the reference. The PID controller is faster than the BPID, although, just as in the previous test, the latter reaches the reference in a smoother and more regular way, preventing overshoot.

In relation to the RMSE values for these two tests, it can be said that the best performance is achieved by the BPID controller, followed by the PI-PD and the PID controllers. Actually, although according to the RMSE values the PI-PD controller performs better than the PID controller, by looking in detail at the response of the three controllers when tracking the step and the incremental step references, the PID controller performs slightly better that the PI-PD controller, as can be seen in Figure 5.16.

As with the RMSE, the measured IAE values imply that the best controller in terms of accuracy is the BPID, followed by the PI-PD and the PID. But, as stated above, the PID controller is slightly better than the PI-PD, especially when tracking step references. This can be seen in Figure 5.17, which shows a detailed view of the actuator reaching the maximum step of the incremental step reference. Although both the PID and the PI-PD controller overshoot when reaching the reference, the overshoot of the PID is smaller than the one of the PI-PD. Also the steady-state error of the PID is smaller than the one of the PI-PD, and also than the one of the BPID.

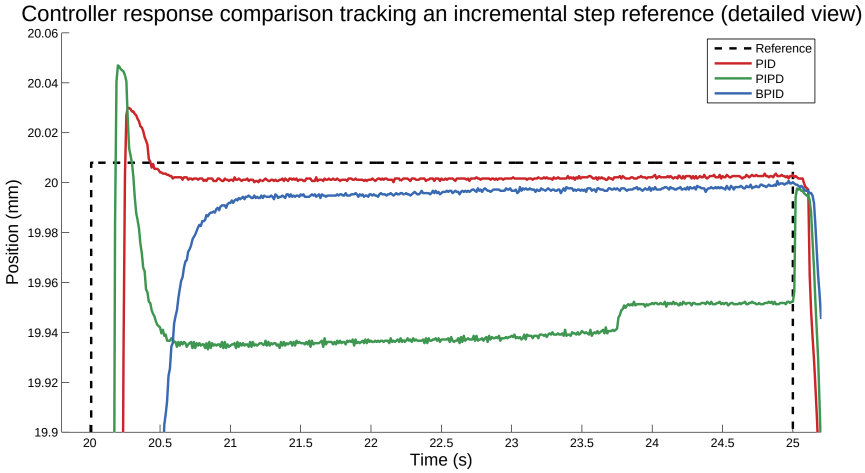

Figure 5.17: Detailed view of the PID, PI-PD and BPID tracking the fourth step of the incremental step reference

The overall performance of the PID controller is better than the performance of the PI-PD controller, as shown in the previous figures. However, both the RMSE and IAE values, which measure the accuracy of the controllers, are bigger for the PID than for the PI-PD. This contradiction can be explained by two reasons. First, the PI-PD controller is the fastest of the three during the ascending part of the actuation, so its error while reaching the steady part of the reference has a shorter duration than the error of the other two controllers. This implies a smaller value of IAE, which accumulates error over time, for that portion of the actuation. The second reason has to do with the descending parts of the actuation. If we think of the IAE value as the area between the reference and the real position, it is clear from Figure 5.18 that during the descending parts of the actuation, the PID controller has the greatest error, followed by the PI-PD and the BPID controllers. This could explain why, although the performance of the PID controller is better than the one of the PI-PD in the steady portions of the reference, the measured RMSE and IAE values are greater for this controller than for the PI-PD.

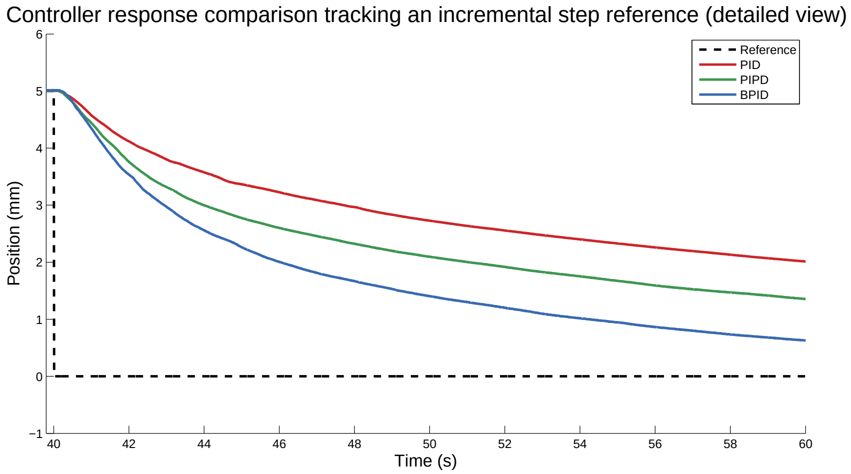

Figure 5.18: Detailed view of the PID, PI-PD and BPID tracking the last portion of the incremental step reference

As explained before, the MACSI value is a measurement of the "abruptness" of the control signal and therefore, a measurement of how large are the variations of the electrical power delivered to the SMA actuator. The amplitude of these energy fluctuations might affect the service life of the actuator. The processes of atomic rearrangement, which ultimately produce the shape memory effect, are triggered by a change in the temperature of the alloy, and this temperature variation is caused by the change of the electrical power fed into the SMA. The reorganization of the crystal structure of the material causes internal stresses that, after a number of transformation cycles, produce microcracks that start to degrade the alloy. Because of this, it might be assumed that, if the control signal generated by the controller has great variations, which result in large fluctuations of the input power of the actuator, the SMA would undergo greater partial phase transformations. In other words, the crystal structure would be greatly modified, causing larger internal stresses and accelerating the appearance of microcracks which ultimately might lead to the breakage of the SMA transducer.

From the MACSI measurements, it is clear that the controller that applies greater energy variations to the SMA actuator is the BPID, as can be seen in Figure 5.19. The PI-PD controller is the one of the three tested controllers which might increase the service life of the actuator. Still, the real effect of these differences on the abruptness of the control signal in the service life of the actuator should be studied to validate this hypothesis.

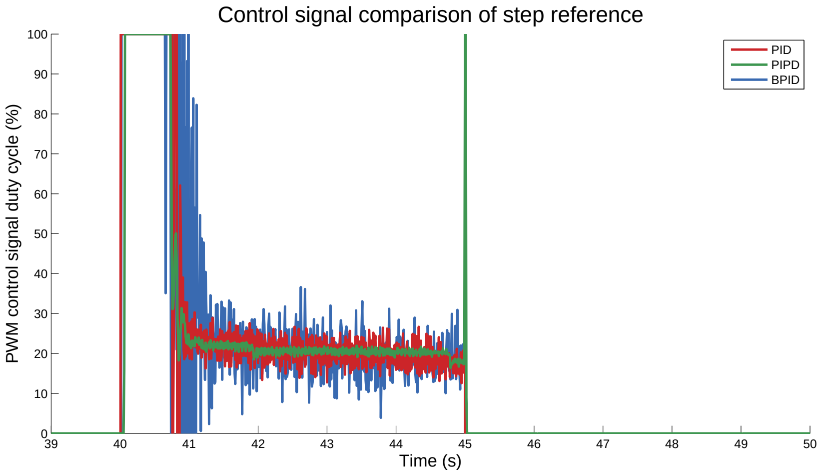

Figure 5.19: Control signal of the PID, PI-PD and BPID tracking the first step of the step reference

Finally, regarding power consumption, the average power consumed by the SMA actuator during each of the performed tests is very similar regardless of the selected controller. Both the PID and the BPID have a slightly greater power consumption when compared with the PI-PD, which is consistent with their greater MACSI values.

An interesting conclusion can be drawn from the fact that the BPID controller has a slightly greater energy consumption than the other two controllers. The power consumption of the actuator is related to its input current, which is regulated by the controller output. Taking this into account, the slightly higher power consumption of the BPID controller means that it is more active than the other two controllers. The fact that the BPID controller is more active leads to the smoother actuator output with respect to the other two controllers.

5.5 Conclusions

In the light of the presented results, it can be stated that the BPID controller proposed in this chapter is a viable alternative to control the position of SMA actuators. As an SMA is a material with a nonlinear behavior, it is assumed that the most appropriate control techniques for those actuators based on this type of alloy are nonlinear controllers. Among the many existing controllers in the field of nonlinear control, we have considered bilinear controllers, and more specifically the four-term bilinear PID controller presented here, as a promising alternative. Although there are many other options to control this kind of actuators with hysteresis, the proposed BPID controller has the advantage of being simpler to implement than other control strategies such as inverse hysteresis model controllers that, besides having a greater complexity, require the application of a series of model identification techniques which extend the implementation process and make the controller operate optimally only under those conditions in which the actuator has been identified. Besides, since the bilinear term linearizes the dynamic behavior of the plant, the well known analytical techniques existing for linear systems can be applied to this type of nonlinear controller.

The conducted tests and the different metrics that have been computed from these tests allow to draw some conclusions. When subjected to sinusoidal references, there is little difference between the three strategies. At low actuation frequencies, the PID and BPID controllers perform better than the PI-PD, which oscillates noticeably around the reference during its ascending portions. However, the latter controller performs better than the former ones during the descending parts of the reference. Also, at the highest tested frequency, 0.5 Hz, the performance of the PI-PD controller is better than the one of the other two. The behavior of the PID and BPID controllers is very similar at low frequencies, but as the actuation frequency increases, the results obtained with the BPID improve with respect to the ones obtained with the PID strategy.

The greatest differences in the performance of the three controllers have been observed in the experiments in which the actuator tracks step references, both for great position variations and for small position increments. In none of the many tests performed, the BPID controller has produced overshoot, unlike the other two tested controllers. This good results are due to the additional gain introduced by the bilinear compensator, which increases the control action when the position of the actuator is far from the reference, and gradually decreases it as the actuator approaches the commanded position. For step references, the only disadvantage of the bilinear term is that it slightly reduces the speed of the controller, but compared with the PID and PI-PD strategies, the difference is only 0.2 s and 0.3 s, respectively.

Although the SMA actuator has a slightly greater power consumption and its service life might be shorter when controlled with the BPID strategy, regarding its accuracy when tracking a given position reference, the BPID controller outperforms the other two tested strategies. Further experiments have to be conducted to study how the use of different gains in the bilinear compensator affects the performance of the controller, since one of the alleged advantages of the BPID strategy is that the bilinear compensator allows increasing the PID gains to improve the speed of the controller without degrading its performance. Also, the proposed control strategy should be compared with other nonlinear control techniques.

Chapter 6

Application to the HEMS exoskeleton

In the preceding chapters, we have presented an SMA-based actuator designed to be used in the field of soft wearable robotics, a thermomechanical model of its SMA transducer and the bilinear controller implemented to compensate the nonlinear behavior of the transducing alloy. Being designed to be used in soft wearable devices and taking into account the physical properties of the SMA wire used as its transducer, the actuator has been conceived considering two fundamental design constraints. On the one hand, the soft robotics design philosophy imposes a preference for the use of flexible and deformable elements. For this reason, the actuator has been designed with a flexible and low profile body, so that in can be easily integrated into textiles or other deformable materials from which the structure of the wearable robot is made. On the other hand, the limited maximum strain produced by an SMA wire implies the use of very long wires to obtain displacements in the range of several centimeters, as is usually required to actuate wearable devices.

The combination of the above requirements has resulted in a design based on the Bowden cable transmission system similar to the motor-tendon systems commonly used in soft robotics, except that, in this case, the transducer of the actuator is also the transmission cable that is routed inside the Bowden sheath, constituting what could be described as an *active tendon*. The resulting device is a lightweight actuator with a long and flexible body, designed to be worn over the body without causing discomfort or hindering the user's mobility. However, all the tests conducted so far (the actuator characterization and controller performance tests) have been completed using a test bench. By doing so, we have been able to study the operation of the actuator and its controller under very specific conditions, dependent on adjustable physical parameters such as the mechanical load applied to the output of the actuator or its bending angle. To fully validate the designed actuator along with its controller, they should be integrated and tested in a real soft wearable robot. This chapter describes the design and preliminary assessment of a device of this kind, more specifically, an SMA-actuated soft hand exoskeleton designed to address one of the problems that astronauts face during spacewalks: hand fatigue caused by the gloves of the pressurized spacesuit. Rather than as an exoskeleton, this device can be defined as an *exomusculature*. Designed according to the soft robotics design paradigm, there is no external rigid structure, and the actuation system, consisting of a set of linear actuators connected to the fingers through a series of artificial tendons, somehow mimics the musculotendinous system of the human hand.

This chapter extends the research on the design and control of soft SMA actuators presented in chapters 3 and 5 and shows how the concepts developed in those preceding chapters can be applied in the design of a real device. Building on the flexible SMA actuator design proposed in Chapter 3, we present a more polished actuation device that can be potentially deployed on different types of soft wearable robots. This improved design integrates position and force sensing and includes an output mechanism that allows reducing the length of the SMA element by multiplying its output displacement. We have also extended the application of the BPID controller presented in Chapter 5, using it to control the force exerted by an SMA actuator.

The rest of the chapter is organized as follows. In Section 6.1, the context of the development of this exoskeleton is outlined, clarifying why such a device is needed and briefly reviewing the literature related to the problem it addresses. The design of the soft hand exoskeleton and its subsystems is detailed in Section 6.2. Section 6.3 describes the tests that have been conducted to characterize the nominal operation of the device and its actuation system, as well as the position and force control tests performed to study its controllability using the BPID controller presented in Chapter 5 and to evaluate its suitability as a force assistive device. The conclusions drawn from the development and testing of the soft exoskeleton featured in this chapter are summarized in Section 6.4.

6.1 Context

Since the beginning of the space race in the mid-50s, space exploration has been a subject of increasing importance for governments and agencies worldwide, because of different scientific, technological and economical reasons. Although in the last two decades manned missions have been progressively replaced by robotic missions thanks to the technological advances in this field, human presence still is of great importance in those tasks where robotics is not yet ready to replace human skills. For instance, astronauts in the International Space Station (ISS) are responsible for the installation of new equipment and modules, repairs and maintenance, and the setting and monitoring of experiments, that is, tasks that require dexterous manipulation. During these extravehicular activities (EVA), astronauts wear a full-body protective suit that provides environmental protection, mobility, life support and communications. The spacesuit is a semi-rigid equipment made of multiple layers to protect the user from the vacuum of space, radiation, extreme temperatures and micrometeoroids. To prevent the expansion of the gases and processes of the body that would be caused by the absence of pressure, an EVA suit is internally pressurized to simulate Earth conditions (normally less than one atmosphere). This internal pressure also exerts mechanical compression to avoid the expansion of the astronaut's skin and flesh.

Despite the advances that have taken place over the last decades in spacesuit technology, factors such as suit induced trauma, fatigue or reduced mobility/dexterity still limit the duration of spacewalks during EVA. These problems especially arise in the case of the hands. A study conducted by NASA with 86 astronauts during 770 sessions showed that the subjects suffered injuries in 45.7 % of the sessions, and that 47 % of those injuries involved the hands [197]. Other studies found that, when using EVA gloves, the astronaut's grip strength was decreased up to 50 % of the force exerted with bare hands [198, 199]. The decrease in hand strength when performing different tasks with a pressurized glove reported in [200] is more dramatic, being a 80 % to 90 % of the bare hand force.

Hand-related injuries and fatigue are caused by the great stiffness of the spacesuit gloves. Like the rest of the suit, EVA gloves are internally pressurized. The pressure inside the gloves, combined with the multiple layers of which they are composed, increase the stiffness of each of their joints, making the astronaut exert great forces to overcome this rigidity and mobilize the fingers. Some studies have quantified the opposing forces exerted by the EVA glove on the hand, measured as the integral of all pressures on the whole hand surface, obtaining a mean force of 32 N and peak values of 38 N for power grip [201, 202]. The stiffness of EVA gloves leads to problems other than hand fatigue, such as damages in the nails, difficulties to move with dexterity and lack of control of the applied force on the objects. With NASA, as well as other space agencies, planning to dramatically increase the number of EVA hours during future manned missions [203], a problem known as "the mountain of EVA" (Figure 6.1), there is a need for solutions that minimize the negative effects derived from the use of an EVA suit.

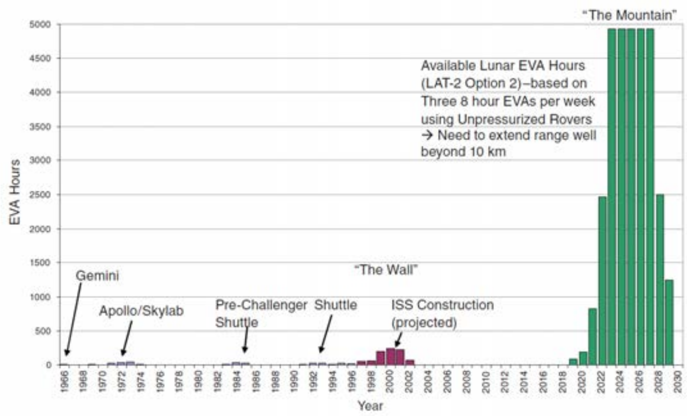

Figure 6.1: The mountain of EVA [203] (reproduced with the permission of the authors).

With the aim of reducing hand fatigue during EVA missions, several authors have proposed the integration of external actuators, such as gas filled bladders [204, 205], geared DC motors [206, 207], ultrasonic motors [208] or pneumatic artificial muscles (PAM) [209], into the EVA glove, to apply an additional torque at the metacarpophalangeal (MCP) joint of the spacesuit glove and reduce the effort required to move the fingers.

A different approach to overcome the rigidity of EVA gloves is to augment the astronauts' force by means of a hand exoskeleton worn over the glove. Favetto *et* *al.* have devoted several papers to study what features such devices should have, in terms of structure and kinematics, actuators, sensors and control [210, 211, 212]. The most noteworthy examples within this approach are the exoskeletons based on four-bar linkages implemented by Shields *et al.* [213] and Favetto [214], the flexible fiberglass shell actuated by a single PAM designed by Matheson *et al.* [215] and the low profile cable-driven finger exoskeleton proposed by Favetto [214].

Although conventional exoskeletons are an effective solution to overcome the stiffness of EVA gloves, they have some problems that may prevent their use in a real spacesuit. These devices are usually bulky, which would make the spacesuit gloves even more cumbersome. In addition, NASA limits the working envelope of the glove to specific dimensions, in order to use the different tools and interfaces required on EVA missions, so any device attached to the glove can not exceed these dimensions[1]. Another problem is the added weight when wearing the exoskeleton, which increases the inertia in the astronaut's limbs. In Chapter 1, we have seen how conventional exoskeletons have some problems regarding joint misalignment and motion restrictions, and have to be carefully designed, usually using complex kinematic chains, in order not to cause the wearer discomfort and difficulties in controlling the device. These problems are further exacerbated when an exoskeleton is integrated into a spacesuit, which already limits mobility and impedes natural limb control.

The design framework of this thesis, the field of soft robotics, has some significant benefits regarding the integration of a wearable robot into a spacesuit. Being flexible, a soft exoskeleton will not make the spacesuit stiffer. Unlike rigid exoskeletons that usually hinder the natural motions of the user's limbs, soft exoskeletons are more compliant from a kinematic point of view, reducing the restrictions to the wearer's movement. Since the stiff nature of spacesuits already obstructs the astronaut's normal range of motion, this feature of soft exoskeletons is an additional advantage regarding their use in EVA activities. Finally, the lower bulkiness of soft exoskeletons with respect to their rigid counterparts implies an easier integration into existing spacesuits.

Being a relatively new field, there are very few examples of the soft robotics approach applied to the design of power-assisted EVA gloves. Freni *et al.* carried out a preliminary study of possible actuation and sensing technologies that could be used in the design of a soft hand exoskeleton intended to be integrated into a spacesuit glove [216]. Electroactive polymers, and more specifically dielectric elastomers, are proposed as the transducer element of a new soft actuator that complies with the project requirements. The resulting bending actuator, which is only theoretically studied but not implemented, consists of several stacked dielectric elastomer layers. With this configuration, the amount of bending of the actuator can be controlled by applying different voltages to the different layers. To control the device, some tests

---

[1] NASA-STD-3000/T

are performed to study the suitability of electromyography and mechanomyography as methods to detect user's motion intention.

NASA along with General Motors have designed the RoboGlove, a force augmentation glove based on the actuation system of the Robonaut humanoid robot, to be used in heavy-duty and repetitive assembly tasks, as well as in augmented spacesuit gloves [217]. The device is operated by a cable-driven actuation system consisting of three linear DC actuators located on the forearm of the glove and a series of flexible Bowden sheaths to guide the tendons from the output of the actuators to a rigid piece on the palmar side of the glove. To control the additional force provided by the actuation system, five pressure sensors embedded in the fingertips of the glove measure the contact forces with the environment, which are compared with a predefined activation threshold. With this configuration, the RoboGlove is able to exert a peak grasp force of about 220 N and a continuous grasp force of 67-89 N.

Continuing with this line of work, Rogers *et al.* have developed the Space Suit RoboGlove (SSRG) as a result of integrating the RoboGlove technology into a Phase VI EVA glove [218]. The SSRG uses the same cable-driven actuation system as the RoboGlove but instead of using and additional rigid piece to fix the Bowden sheaths of the actuators to the palm of the glove, the standard palm bar of the Phase VI EVA glove has been modified to this end. The artificial tendons are attached to the fingers by means of low profile polycarbonate bands fixed to the restraint layer of the EVA glove. Regarding the pressure sensors used to control the device, the commercial sensors used in the RoboGlove have been modified to suit the particularities of an EVA glove. In addition to the fingertip sensors, the SSRG includes pressure sensors in the middle part of the proximal and medial phalanxes of the index, middle and ring fingers, to investigate optimal sensor placement in order to maximize the response when manipulating different objects. The SSRG has been tested inside a depressurized glove box that simulates the operating pressure of a real spacesuit, to study the ability of the actuation system in providing the required force to assist astronauts in real working conditions. The tests reveal that the SSRG is able to provide a grasping force of approximately 45 N additional to that exerted by the test subjects, and that the average grip strength is higher and more consistent as the subjects become fatigued when compared with the results obtained with the assistive system turned off.

6.2 Design

This chapter presents the Hand Exo-Muscular System (HEMS), a soft hand exoskeleton designed to prevent astronauts from exerting all the force needed to mobilize the fingers when wearing an EVA glove, in order to mitigate hand fatigue and the other hand-related problems that arise during EVA missions. The HEMS, shown in Figure

6.2, is intended to be embedded into the spacesuit glove, so it should not add any additional volume or stiffness. For this reason, the exoskeleton has been designed following the soft robotics approach.

Figure 6.2: HEMS overview.

Given the cost per kilogram sent to space, weight reduction is a major design factor when developing a device to be used in this environment. Jones [219] lists launch costs to low Earth orbit for different systems, including those currently in use such as the ESA's Ariane 5G ($13,100/kg), Roscosmos' Soyuz ($7,600/kg) and SpaceX' Falcon 9 ($2,700/kg, which is increased to $25,000/kg when used along with the Dragon capsule to send cargo to the ISS). The importance of weight reduction has been taken into account during the development of the HEMS, being one of the main reasons for choosing the SMA-based actuator designed in this thesis to implement the exoskeleton actuation system. This actuator will allow us to design a lightweight and compact actuation system capable of delivering the required assistive forces. This, together with the lack of a rigid structure, a consequence of having designed the HEMS according to the soft robotics approach, will make the device much lighter than an exoskeleton with the same functional characteristics but with a rigid structure and a conventional actuation system.

Besides the SMA-based actuation system, the HEMS is composed of the suit structure, which is the physical layer into which the actuation and sensory systems are integrated and which transmits the forces generated by the actuators to the user's fingers, and the sensory system, a set of force and position sensors for the actuators and pressure sensors located on the fingertips of the glove. The control hardware uses the information provided by the sensory system to control the actuation system in such a way that the adequate assistive forces are provided. A power supply unit provides the required power to the actuators, sensors and control electronics.

6.2.1 Suit structure

In the case of a conventional exoskeleton, the rigid structure of the device provides the mechanical support and anchoring points for the actuators, sensors, control hardware, batteries... Although in a soft exoskeleton there is no rigid structure, some kind of support element is also required to attach all the hardware to the wearer's body, as well as some kind of mechanical interface to transmit the displacements and forces generated by the actuators to those parts of the body upon which the device acts. In the case of the HEMS, the suit structure is composed of a body harness, a forearm elastic sleeve and a glove, as can be seen in Figure 6.2.

The glove is the most important element of the suit structure: it is the mechanical interface that transmits the forces generated by the actuators to the user's fingers. The actuators are connected to the glove through a series of inextensible cords attached to the fingertips and routed through the underside of the fingers and the palm of the glove, mimicking the tendon system of a human hand. The function of this artificial tendon system is to transmit the force and linear motion of the actuators to the fingertips of the glove, causing the user's fingers to flex. The index, middle, ring and little fingers have only one tendon each, while the thumb has two tendons: one attached to the tip to perform the flexion movement, and a second one attached to the base of the thumb to perform the abduction movement. This arrangement makes a total of six actuated degrees of freedom. While the flexion of the fingers is active, the extension movement does not need to be actuated, as the opposing force exerted by the internal pressure of the EVA glove causes the hand to tend to be open.

(a) (b)

Figure 6.3: HEMS glove: (a) internal glove with the tendon and actuation systems and (b) external glove.

Figure 6.3a shows the arrangement of the HEMS tendon-based transmission system. Each artificial tendon is routed from the output of an actuator to the base of its corresponding finger through a flexible nylon tube with one end fixed to the actuator and the other end sewed to the palm of the glove. From this point, the tendon is guided over the underside of the finger up to the fingertip of the glove, where it is fixed. Two plastic rings located on the proximal and medial phalanxes keep the tendon in place, close to the finger, and transmit the force generated by the actuator to the dorsal side of the phalanxes. To fix the tendon to the fingertip, it forms a loop over the dorsal side of the distal phalanx so that, when a tensile force is applied to the tendon, a normal force is applied to this side of the finger, leading to its flexion and reducing the deformation of the glove.

Due to the impossibility of using a real EVA glove, for testing purposes the HEMS external glove is a heavy-duty rubber glove (Figure 6.3b). A heavy-duty glove has been chosen because, due to its thickness, it impedes the natural motion of the wearer's fingers in a somehow similar manner than a pressurized EVA glove.

6.2.2 HEMS actuation system

To establish the amount of assistive force the HEMS actuators should deliver, lets first consider the maximum force exerted by the human fingers at the tip, which, according to Sutter *et al.* [220], is 49 N. If, as stated before, the EVA glove reduces the astronaut's grip strength a 50 % of the force exerted with bare hands, this means that a normal force of 24,5 N have to be applied at the fingertips to flex the fingers. According to Hadi *et al.* [221], the normal force at the fingertips in a tendon-driven robotic glove similar to the HEMS is a 35 % of the pulling force applied to the tendon. This means that, in order for the device to exert all the force necessary to counteract the rigidity of the glove, the actuators should be able to provide 70 N of pulling force.

The envisaged application of the HEMS in the context of space exploration makes it a device that can greatly benefit from the use of an actuation system based on the flexible SMA actuator concept presented in Chapter 3. On the one hand, given the above force requirement and the volume and weight constraints imposed by the integration of the HEMS into an EVA glove, the actuators should use a high force density transducer such as an SMA wire which, as we have seen throughout this thesis, has a performance equivalent to that of electric motors and also have the highest force density within the category of lightweight actuators (below 100 g). On the other hand, the developed actuator has been designed to be used in soft wearable robots so that it can be integrated into textiles and clothing, making it specially suited to be embedded into a spacesuit without further interfering with the astronaut's movements.

To avoid using a large diameter wire with a high force output but a very low actuation bandwidth as the actuator transducer, the HEMS assistive force will be defined as a 50 % of the force required to fully overcome the opposing force of an EVA glove, that is, 35 N. With this force requirement, the actuators of the HEMS actuation system will use the same SMA transducer used in chapters 3 and 5: a Flexinol HT wire, with an austenite start temperature of 90 °C, a diameter of 0.5 mm and a pull force of about 35 N [86]. The multilayer sheath that constitutes the flexible body of the actuator will also have the same configuration as in the preceding chapters: it will comprise a PTFE internal tube with an inner diameter of 0.66 mm and an outer diameter of 1.168 mm and an external stainless steel helical sheath with an inner diameter of 1.4 and an outer diameter of 3.

Once we have established the amount of force the SMA wire has to exert, and therefore its diameter, we have to define its length, which will depend on the expected output displacement. To fully flex the index finger of a person wearing the HEMS, its corresponding artificial tendon has to be linearly displaced 5-6 cm. If the contraction of the SMA wire is limited to a 3 % of its total length in order not to degrade the service life of the actuator, such displacement requirement would imply the use of a 2 m long SMA wire. Although the flexible body of the actuator would allow routing this long wire along the user's arm and back, a greater length also would imply a higher mass. The higher the mass, the more energy would have to be supplied to heat the SMA and trigger its phase transformation, and also the cooling time would increase because more energy would be stored in the transducer.

To reduce the length of the transducer while maintaining the required displacement at the actuator output, the strain of the SMA wire will be multiplied. To this end, its moving end is not directly attached to the tendon that connects it to a HEMS finger, but rather each actuator has an additional interface, an actuation unit, shown in Figure 6.4, which includes the displacement multiplier and also integrates a linear position sensor. The displacement multiplication is achieved by means of a pulley that connects the moving end of the SMA wire to its corresponding artificial tendon of the transmission system. The pulley doubles the displacement of the SMA transducer but has the drawback of reducing the pulling force generated at the output of the actuator to half the force exerted by the wire. Using this displacement multiplier mechanism, the length of the wire used in the actuator has been reduced to 90 cm.

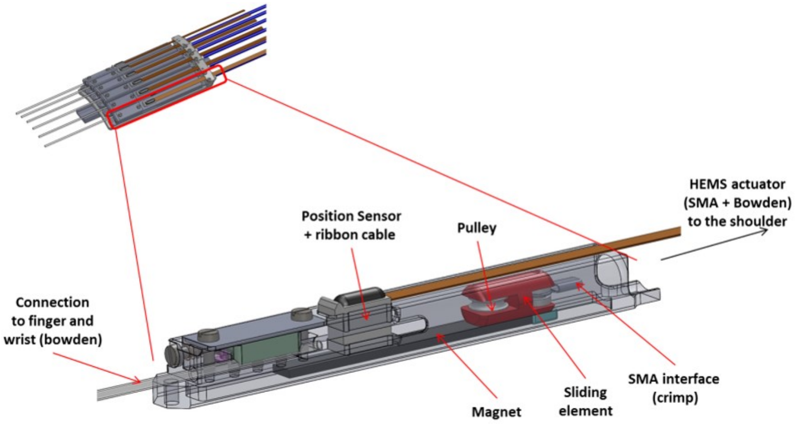

Figure 6.4: Elements of the SMA actuation unit.

The pulley is installed at one end of a sliding element guided inside the enclosure of the actuation unit. The moving end of the SMA wire is attached to the other end of the sliding element so that it is displaced by the motion generated by the wire. The artificial tendon that connects the output of the actuator with the finger it actuates runs over the pulley, having one end attached to the fingertip and the other end fixed to the enclosure of the actuation unit, which is an equivalent assembly to a block and tackle mechanism. In this way, when the sliding element of the actuation unit is displaced by the SMA wire, the displacement of the tendon is twice that of the sliding element.

The displacement of the sliding element, and therefore of the SMA wire, is measured by a RoLin linear incremental quadrature encoder[2] integrated in the enclosure of the actuation unit. The sensor measures the displacement of a multipole magnetic strip installed on top of the sliding element. The actuation unit also provides a fixing point for the multilayer Bowden sheath, as well as a fixing point for the nylon Bowden sheath that routes the artificial tendon from the output of the actuator to the base of its corresponding finger.

To ensure the proper operation of the actuators, the distance between their output and the actuation points (the fingertips of the HEMS internal glove) must be kept constant. If the actuators were fixed to the user's forearm, this condition would not be

---

[2] `https://www.rls.si/en/rolin-linear-incremental-magnetic-encoder-system`

met if, for example, the user flexed the wrist, in which case the transmission tendons would be slack and the force and displacement generated by the actuators would not be properly transmitted to the fingers.

In order to avoid the influence of the position of the hand on the operation of the actuators, the six actuation units are installed on a mobile platform which slides over a rail sewed to the forearm elastic sleeve, parallel to the user's forearm. The displacement of the mobile platform is coupled to the angular motion of the wrist on the sagittal plane so that when the wrist is flexed, the platform slides backwards, and when the wrist is extended, the platform moves forwards, as Figure 6.5. As detailed in Section 6.2.1, six nylon sheaths connect the base of the fingers of the HEMS internal glove to the output of the actuators, as shown in Figure 6.3a. In addition to guiding the tendons, they also serve to keep the distance between these points constant, regardless of the position of the hand. Also, this set of nylon sheaths is the mechanical interface that transmits the angular motion of the wrist to the moving platform.

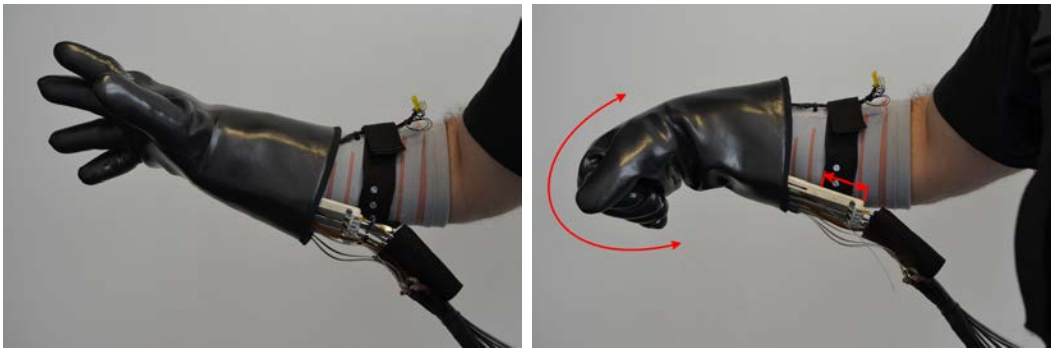
(a) (b)

Figure 6.5: Displacement of the mobile platform: (a) initial position with extended wrist and (b) position after wrist flexion.

The other attachment point of the HEMS actuation system consists of three plastic modules located on the back of the user's right shoulder, sewn to the body harness, as shown in Figure 6.6b. Each shoulder module serves as the fixing point for two SMA actuators, providing a constant mechanical reference point for both the Bowden sheath and the SMA wire that compose each actuator. Also, each shoulder module houses two force sensors, specifically developed for this application by SENSODRIVE[3], to measure the stress of the two SMA transducers of the actuators fixed to the module. These sensors can measure forces up to 50 N and their application is twofold: the measured force is used as the feedback signal by the force controller and

---

[3] `https://www.sensodrive.de/EN/`

also as a safety measure to prevent the SMA transducer from reaching values that could harm the user or damage the actuator.

A shoulder module is composed of three elements, displayed in Figure 6.6a: a coupling interface, which is is the part of the module that is sewn to the body harness, and two mechanical interfaces, each of which houses a force sensor and provides the attachment point for the Bowden sheath of one actuator. The SMA wire is fixed to the measuring part of its corresponding force sensor, so that the pulling force exerted by the actuator can be measured. Thanks to the arrangement of the shoulder modules, the HEMS actuation system can be easily attached to and detached from the suit structure, making the donning and doffing of the exoskeleton easier.

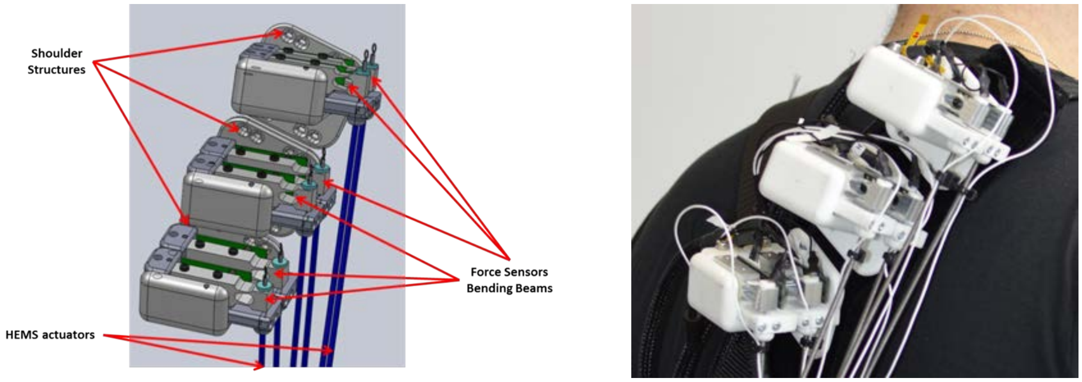

(a) (b)

Figure 6.6: (a) Elements of a shoulder module and (b) location of the shoulder modules on the suit structure.

The total weight of the HEMS is less than 1.5 Kg and, with the exception of the shoulder modules, has a very low volume, which was one of the design objectives. Each of the HEMS actuators weights approximately 150 g, a substantial reduction compared to the 268 g of the SSRG actuators [218, 222], which is the most similar device to the HEMS in terms of its intended use and design philosophy. This is the major advantage of using SMAs over conventional actuation technologies. Thanks to their high force density, it is possible to design actuators with a performance comparable to that of DC motors or pneumatic actuators, but with a fraction of their volume and weight.

6.2.3 Control hardware

To control the HEMS, the same hardware setup (power and control electronics) used in chapters 3 and 5 has been used. To regulate the current applied to heat the SMA wires in the HEMS actuation system, we have used the 16 channel power driver described in Section 3.2.1 since it has proved to be a valid solution that can provide the required power to several actuators simultaneously and that allows to control the amount of delivered current with a PWM signal. To drive the HEMS actuators, the voltage has been fixed at 20 V and the current has been limited to 4 A, making the maximum input power of each actuator 80 W.

On the other hand, the low-level control of the HEMS actuation system has been implemented in the STM32F407VG high-performance MCU presented in Section 3.2.2. The control hardware is in charge of reading and processing the force and position measurements from the corresponding sensors in the actuation system, running the control loops using this information as the feedback signals and generating the PWM control signals to operate the actuator drivers. The control hardware also handles the communication with a host PC over a serial USB connection. Through this data link, the microcontroller receives manual control commands and sends all the relevant information for a real-time monitoring of the system status and performance, information that can be stored for further analysis.

6.2.4 Actuator control

Given the effectiveness of the BPID control approach presented in Chapter 5 in controlling the displacement of SMA-based actuators and considering the simplicity of its implementation in embedded systems, the low-level control of the HEMS actuation system is based on this technique.

The BPID control scheme has been used to implement a position controller using the HEMS linear position sensors as the source of the feedback signal, as well as to conduct preliminary force control tests using the HEMS force sensors as the feedback devices.

6.3 Results

Several tests have been carried out to characterize the HEMS and to evaluate the performance of the actuator position and force controllers. However, the device has not been tested with human subjects and all the experiments have been performed on the test bench described in Section 3.3.1. To be able to test the functionality and controllability of the complete device without a real user, the HEMS glove has been fitted on a 3D printed human hand dummy installed in the test bench. Since the HEMS actuators have integrated position and force sensors, the test bench has been used only as a structural element to which the exoskeleton parts have been fixed. To complete these tests, the device has been manually controlled from a host PC, either by sending activation pulses directly to the power electronics in the case of the characterization tests, or by sending position and force references during the control tests.

Only one actuator, the one corresponding to the index finger of the HEMS, has been used for both the characterization and the control tests. To simulate the stiffness of an EVA glove and to provide the pulling force needed to restore the initial length of the SMA wire during the cooling phase, a bias spring has been used. The spring is connected to the fingertip of the index finger by means of an inextensible cord routed through the dorsal side of the internal glove in an antagonistic configuration relative to the actuator. In these tests, the stiffness of the EVA glove has been simulated with this bias spring instead of with the heavy-duty external glove shown in Figure 6.3b because the characteristics of the spring are readily available, while those of the heavy-duty glove are unknown, which implies a greater control over the performed experiments.

Since the position sensor measures the displacement of the SMA wire and the force sensor measures its stress, it must be noted that all the measurements presented here refer to the wire and not to the actuator output. As explained in Section 6.2.2, the position is doubled while the force is reduced by half at the actuator output, due to the multiplying pulley.

In the first place, the actuation system has been subjected to characterization tests with the purpose of evaluating its performance in terms of nominal and maximum displacement and nominal and maximum force. The other set of tests is designed to assess the performance of the actuator position and force controllers in different situations for a given position or force reference.

6.3.1 Characterization

To ensure a proper operation of the SMA wire during the characterization tests, the actuator has been preloaded with a constant force of 30 N, provided by a hanging mass, and a bias spring pretension force of 20 N, making a total preloading force of 50 N. To characterize the nominal operation of the actuator, the input signals have been different current pulses with a fixed amplitude of 4 A and a variable duration ranging from 1 s to 3 s, in 0.2 s increments. As the measured wire resistance is 3.6 Ω, the input power has been 57.6 W. The most stable behavior has been obtained with a pulse of 1.6 s. From 1 s to 1.6 s, there is a 5 mm increment in the actuator output displacement, while from 1.6 s to 3 s, this difference is only 1 mm. The problem of using longer pulses is that, as more energy is used to drive the actuator, the cooling time can be up to three times longer than when using shorter pulses, as can be seen in Figure 6.7. For the 1.6 s pulse, the input energy has been $57.6W * 1.6s = 92.16J$ per contraction, the maximum displacement has been 29 mm (3.22 % strain) and the cooling time has been 4.5 s.

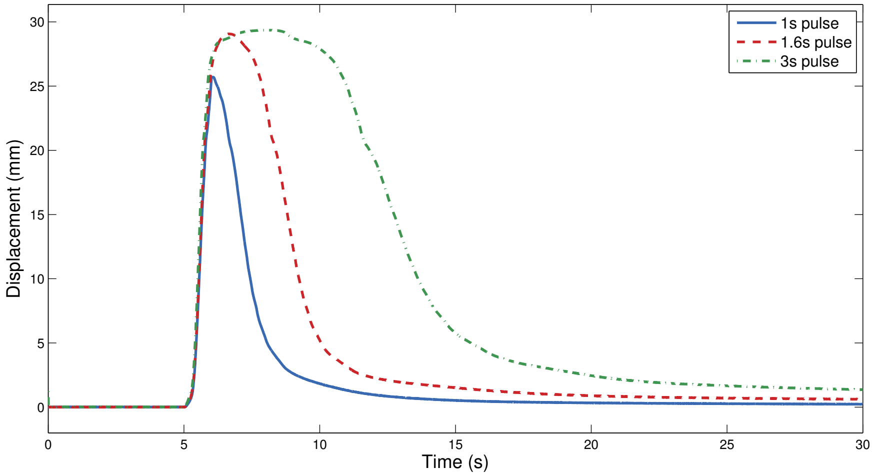

Figure 6.7: HEMS actuator output displacement depending on input pulse duration.

Along with the displacement, the force exerted by the actuator has been measured during the characterization tests, as shown in Figure 6.8. For a 1.6 s pulse, the exerted force has a peak value of approximately 63 N, while the SMA wire can produce a maximum pulling force of 70 N for pulses of 2.2 s or longer. Considering that, because of the pulley of the actuation mechanism, the output force is half this force, the actuator is capable of providing 50 % of the force required to move the fingers in an EVA glove as stipulated.

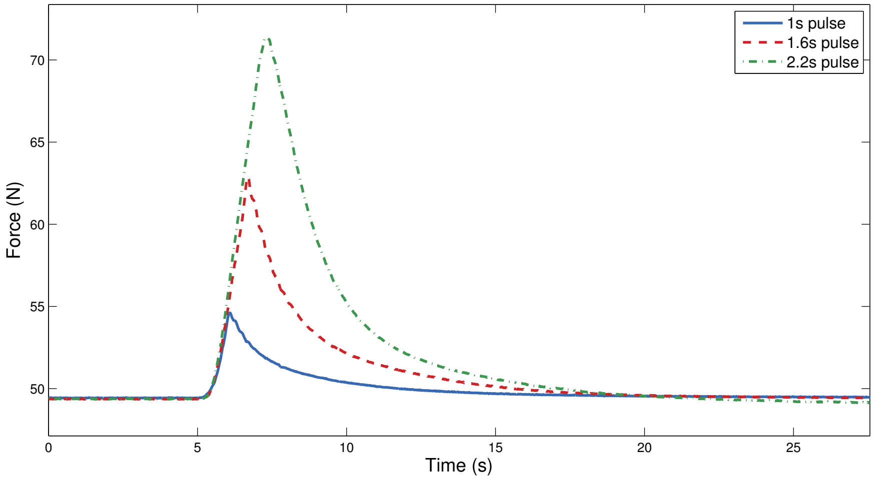

Figure 6.8: HEMS actuator output force depending on input pulse duration.

Force measurements have also shown that, in addition to the inherent hysteresis of the SMA wire, the HEMS also presents a hysteretic behavior in the force-displacement plane. Figure 6.9 shows the force-displacement relationship resulting from driving the actuator with five consecutive current pulses, with an amplitude of 1.6 A and a duration of 1 s each. This hysteresis is caused by the friction between the glove and the artificial tendon that connects the SMA actuator to the fingertip, some additional friction of some of the elements of the test bench, as well as the nonlinear force-displacement behavior of the bias spring.

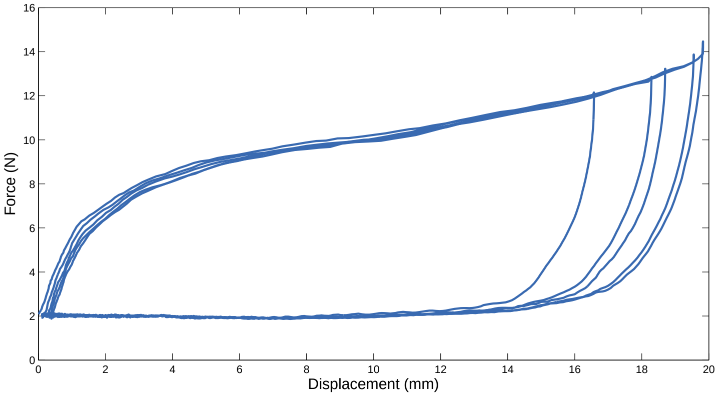

Figure 6.9: Force-displacement hysteretic behavior of the HEMS.

6.3.2 Position control

To evaluate the performance of the BPID control loop in controlling the output position of the HEMS actuator, a set of four different position references have been used:

- Sinusoidal reference with an amplitude of 27 mm peak-to-peak at a frequency of 0.125 Hz, to test the performance of the controller when following a continuously varying reference.
- Ramp reference with an amplitude of 27 mm and a slope of 1 mm/s, to examine the operation of the controller when tracking a slowly changing reference.
- Step reference consisting of two step signals lasting 5 s each, with an amplitude of 27 mm and a 30 s interval between them, to test the behavior of the controlled actuator when it is subjected to a sudden and large position variation and to study its operation in the stationary portion of the reference.
- Incremental step reference in which the position is first increased in four steps of 6.75 mm, from 0 to 27 mm and then returned to the starting position in four

decrements of 6.75 mm, to check the performance of the controlled actuator when it is subjected to small position changes, as well as its stationary behavior at different amplitudes.

Along with the position-time and error-time data graphically shown in Figures 6.10-6.13, three different metrics have been computed to have a quantitative measure of the controller performance. The root-mean-square error (RMSE) has been computed for the ascending parts of the sinusoidal and ramp references and for the stationary portions of the step and incremental step references. In addition, for the latter two references, the rise time to the stationary part of the reference has been calculated. Finally, the average power consumption for the entire actuation cycle has been determined in all four cases. These values can be found in Table 6.1.

The preloading force of the actuator has been modified for both the position and the force control tests. The hanging mass has been removed and the bias spring has been pretensioned to an opposing force of only 2 N.

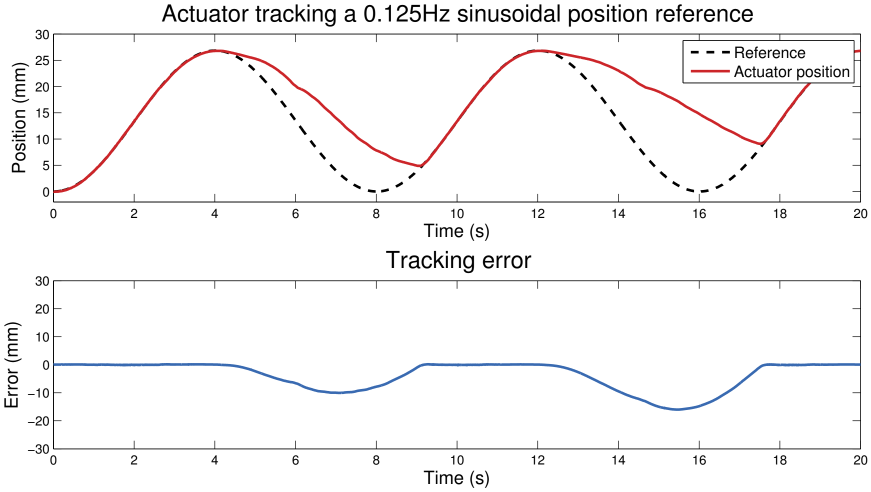

Figure 6.10: Actuator position and error tracking a 0.125 Hz sinusoidal reference.

For the 0.125 Hz reference, the actuator is able to accurately track the ascending part of the actuation, with just a small oscillation around the setpoint of about 0.06 mm. During the descending parts, the actuator is unable to follow the reference for two reasons. The main one is due to the thermal nature of the actuator: the cooling time of the SMA wire is greater than the reference descending time. The second reason is mechanical: there is friction between the tendon and the glove and between the tendon and the test bench, which restrains the response of the actuator during the descending parts of the actuation cycle.

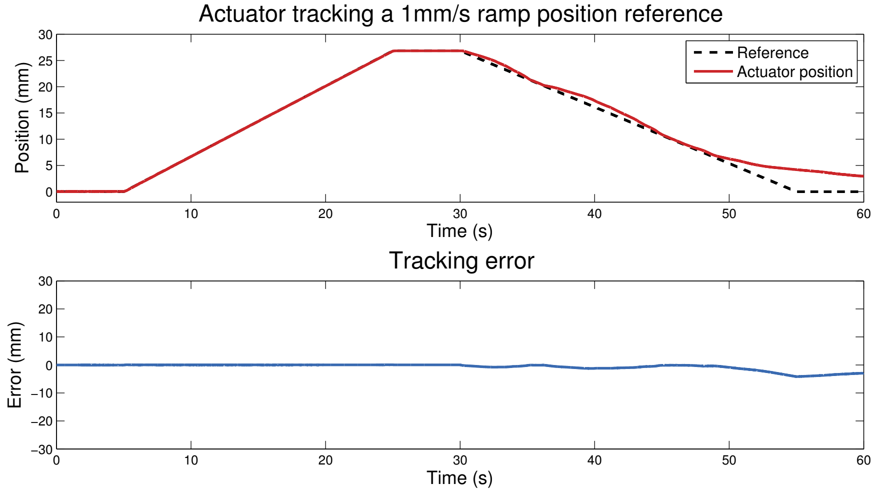

Figure 6.11: Actuator position and error tracking a ramp reference.

Regarding the ramp reference, the accuracy of the controller is also very good. The actuator tracks the ascending ramp with little error, with a maximum oscillation around the setpoint of about 0.02 mm. During the stationary segment of the reference, it is able to accurately maintain the position with a mean steady-state error of 0.01 mm. As in the previous cases, because of the cooling time of the SMA element and the friction of the tendon, the actuator cannot track some portions of the descending ramp.

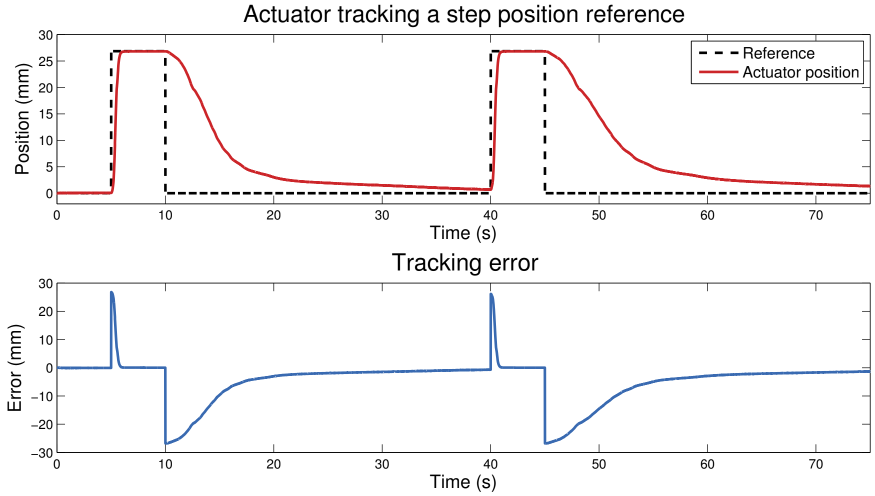

Figure 6.12: Actuator position and error tracking a step reference.

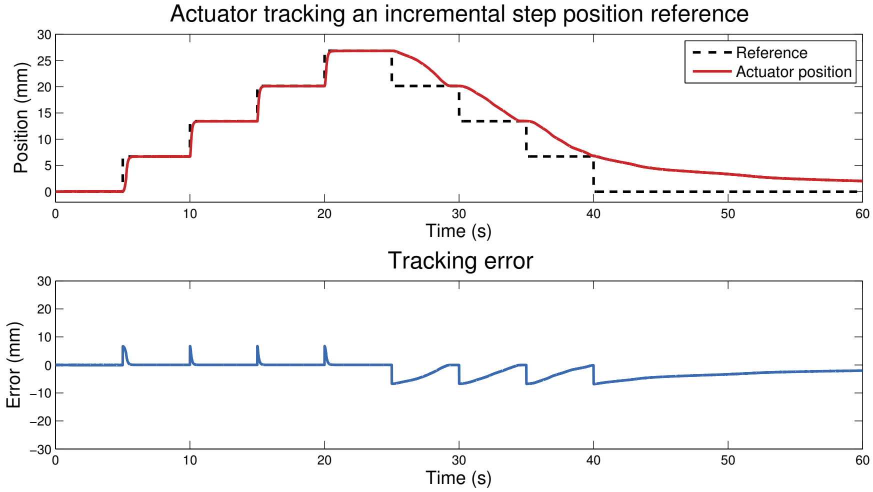

Figure 6.13: Actuator position and error tracking an incremental step reference.

As for the step and incremental step references, the performance of the controller is also very good. In both cases, there is no overshoot when reaching the reference and the actuator is able to accurately maintain the position during the stationary parts of the actuation, with a mean steady-state error of 0.03 mm in the fist case and of 0.01 mm in the case of the incremental step reference. As with the sinusoidal references, the response of the actuator is slow when reaching its initial position, due to the cooling time of the SMA wire and the friction of the tendon.

Reference type	**0.125 Hz sine**	**Ramp**	**Step**	**Incremental step**
RMSE	0.083 mm	0.019 mm	0.072 mm	0.038 mm
Average power	27.14 W	9.98 W	10.63 W	9.15 W
Rise time	n/a	n/a	0.84 s	0.31 s

Table 6.1: Position control performance metrics.

6.3.3 Force control

The behavior of the BPID control loop in controlling the output force of the HEMS actuator has also been analyzed. A set of force references similar to those defined for the position control tests has been used. In this case, the maximum amplitude for all references has been 20 N and, after observing that the actuator has a faster response when force controlled than when position controlled, the ramp reference has been replaced by an additional sinusoidal reference at a frequency of 0.25 Hz. The force-time and error-time graphs are shown in Figures 6.14-6.17 and the RMSE, rise time and average power consumption measurements are summarized in Table 6.2.

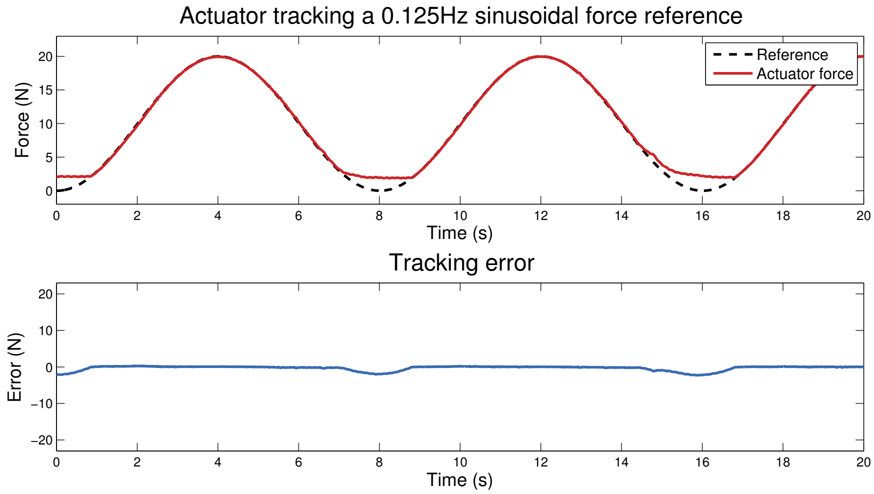

Figure 6.14: Actuator force and error tracking a 0.125 Hz sinusoidal reference.

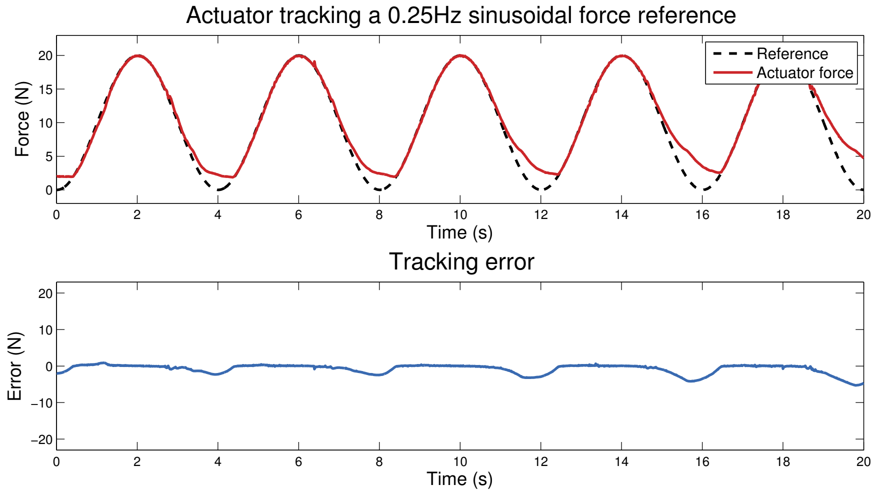

Figure 6.15: Actuator force and error tracking a 0.25 Hz sinusoidal reference.

For both references, the actuator tracks the ascending part of the actuation pretty accurately. However, the noise of the force sensor has a negative impact on the performance of the controller, an issue that has been common to all force control tests. Unlike in position control tests, the force-controlled actuator is able to follow most of the descending part of the sinusoidal references, but in those parts closest to the initial value, the actuator response is still slower than the reference. In those parts where the actuator is able to track the desired reference, it oscillates around the setpoint with an amplitude of 0.1 N in both cases.

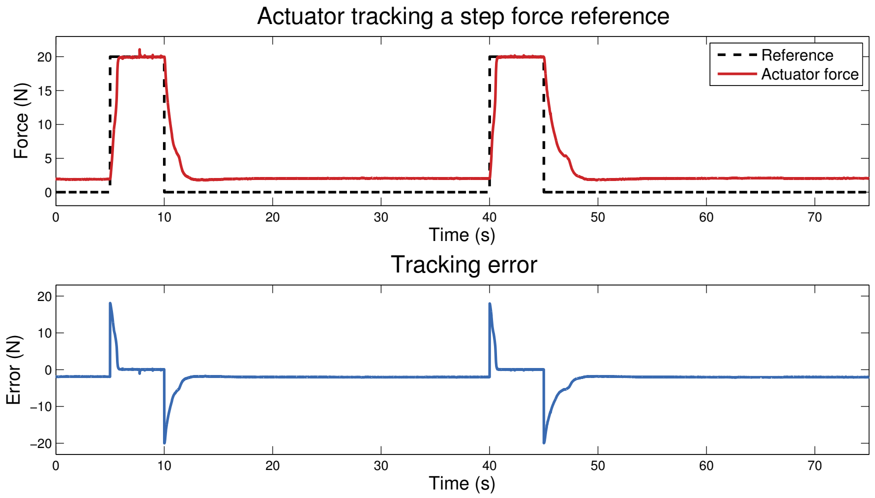

Figure 6.16: Actuator force and error tracking a step reference.

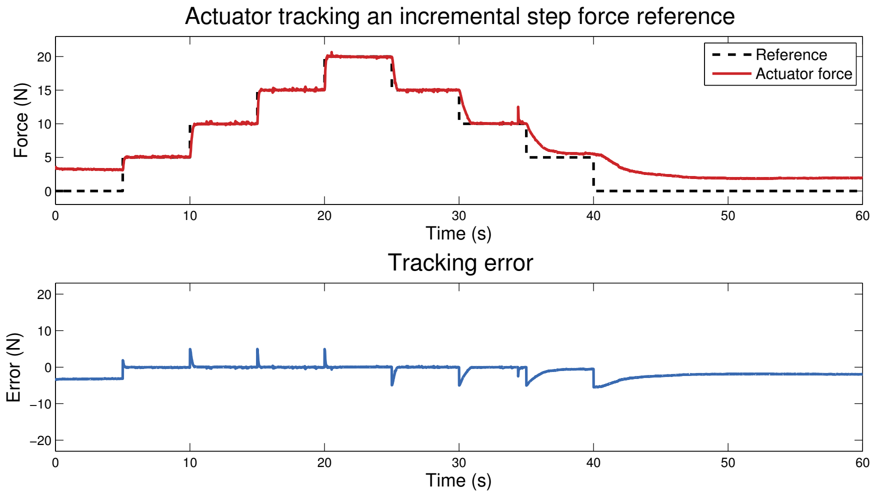

Figure 6.17: Actuator force and error tracking an incremental step reference.

The controller also shows a good performance for the step and incremental step references, although there are some peaks in the measured force due to noise from the sensor. In both cases, the controller shows no overshoot when reaching the setpoint and the actuator stably exerts a constant force during the stationary parts of the actuation. The steady-state error has a mean value of 0.05 N for the step reference and 0.04 N for the incremental step reference. As with the sinusoidal references, the response of the actuator slows down in the last portions of the reference.

Reference type	**0.125 Hz sine**	**0.25 Hz sine**	**Step**	**Incremental step**
RMSE	0.1 N	0.18 N	0.12 N	0.11 N
Average power	19.83 W	24.13 W	13.03 W	13.14 W
Rise time	n/a	n/a	0.77 s	0.22 s

Table 6.2: Force control performance metrics.

6.4 Conclusions

In this chapter, we have presented the Hand Exo-Muscular System (HEMS), a soft hand exoskeleton designed to provide force and motion assistance to astronauts performing extravehicular activities by reducing the stiffness of the pressurized spacesuit glove. Designed as a soft exoskeleton because of the advantageous features these devices have for the intended application, the main element of the HEMS is the shape memory alloy actuator specifically designed for soft wearable robotic applications, based on the flexible design concept featured in Chapter 3. The results obtained in the characterization tests of the HEMS actuation system suggest that the designed device is capable of providing at least 50 % of the force needed to overcome the opposing forces of a spacesuit glove.

The low profile and flexible body of the actuator allow for an easy integration into the structure of the designed soft wearable robot, made of textiles and other compliant materials. The basic design proposed in Chapter 3 has been refined to suit the requirements of the HEMS. A displacement multiplier mechanism has been included to double the displacement provided by the SMA wire at the expense of reducing its pulling force by half, resulting in a nominal displacement of 54 mm and a nominal force of 31 N at the output of the actuator. The HEMS actuator also integrates a position sensor at its moving end and a force sensor at its fixed end in order to be controlled both in position and in force.

Regarding the control strategy, the conducted tests show very positive results. After proving in Chapter 5 how the BPID control strategy is a potential alternative for controlling SMA actuators, in this chapter we have demonstrated that it can also be used to control a device that makes use of such actuators. Moreover, the BPID control strategy has been successfully applied for the first time to implement a force controller for the SMA actuators. The obtained results are very good; the behavior of the actuator is very similar to the one observed when controlled in position, with a high degree of accuracy and stability. Despite the inherent nonlinear behavior of the SMA actuator and the added hysteresis introduced by some of the mechanical elements of the the exoskeleton, the actuator shows no overshoot nor limit cycles in the case of stationary references and the oscillation around the setpoint when following continuously varying references is minimal, in both position and force control. The only limitation lies on its actuation speed imposed by the cooling time of the SMA wire.

One of the main contributions of this work with respect to previous developments in the field is that, to the best of our knowledge, this is the first controlled SMA-actuated hand exoskeleton. There are very few examples of SMA-actuated hand exoskeletons in the literature [223, 224, 225, 221] and none of them are able to control the amount of assistive force they provide nor the position of the user's fingers. In those works, the authors only carried out characterization tests or open-loop control tests using simple on-off controllers.

This is also the first SMA-actuated hand exoskeleton to apply the soft robotics approach to both the structure of the device and to its actuation system. The wrist orthesis presented in [223] is a completely rigid device and the mechanical structure of the exoskeleton in [224] is based on rigid linkages. While the devices presented in [225, 221] use a glove as the interface to transmit the force and motion of the device to the user's fingers, their actuation systems consist of rigid structures that do not exploit the deformable nature of SMAs.

Chapter 7

Discussion and Conclusions

This chapter discusses the results obtained throughout the development of this thesis. The most relevant conclusions derived from each of the developed works, actuator design, transducer model, control and application in a soft hand exoskeleton, are summarized and analyzed. Furthermore, the main contributions to each of these lines of research are highlighted and those aspects susceptible of being further developed are identified in order to suggest possible future lines of work.

Throughout this thesis, the advantages of applying the principles of soft robotics to the design of wearable robots and their actuation systems have been emphasized. We have seen that many of the problems associated with the design of conventional rigid exoskeletons can be solved by applying the soft robotics design approach. The most obvious is the weight reduction that comes with the design of one of these devices according to these principles; while a conventional exoskeleton uses a rigid and usually heavy structure to transmit the forces generated by the actuation system to the wearer, a soft exoskeleton uses textiles and other lightweight and deformable materials for this purpose. In addition, rigid exoskeletons usually use conventional actuation systems, such as geared DC motors, integrated into their structure, which further increases the weight and volume of these devices. On the other hand, the actuation systems of soft exoskeletons also follow this design philosophy so, in addition to being more adaptable and compliant, they can also be more lightweight than their conventional counterparts. However, this is not always the case, as these actuation systems are often based on conventional technologies such as DC motors or pneumatic devices.

However, the main advantage of designing a wearable robot according to the soft robotics design guidelines is that it solves one of the biggest problems of conventional exoskeletons: joint misalignment and motion restrictions. While in a conventional exoskeleton, the kinematic chain of the structure must correspond as closely as possible with that of the wearer to avoid causing discomfort and difficulties in controlling the device, soft wearable robots do not present this problem. As soft robots theoretically have an infinite number of degrees of freedom, there is no kinematic chain in the strict sense of the word, meaning that there are no joints that must be aligned with those of user, avoiding kinematic incompatibility.

Considering the above facts and given that there is still a need for an actuator for soft wearable robots that completely fulfills the requirements of flexibility, weight, size and power, in this thesis we have proposed what we believe can be an alternative to the efforts developed so far. Our proposal is founded on the design of a flexible actuator based on the material with the highest force density among the so-called new actuation technologies: shape memory alloys.

The proposed actuator, presented in Chapter 3, has been designed in such a way that some of those limitations of SMAs that are often considered as a reason to exclude them from the available actuation technologies are mitigated. Faced with the need of using a long SMA wire to be able to generate displacements of several centimeters, we have opted for a mechanical design similar to cable-driven systems, often used in soft wearable robots, which use very long cables routed inside Bowden sheaths to transmit the motion and force of the actuators to the actuation points. In our design, the SMA wire is routed inside a Bowden sheath composed of an internal PTFE tube to reduce frictional losses and an external steel helical tube that acts as a heat sink. This configuration reduces the cooling time of the SMA wire, increasing its actuating bandwidth. In addition, it greatly reduces the thermal runaway effect that affects the controllability of SMA actuators. The actuator has been characterized through a series of tests in which a nominal displacement of 24 mm and a nominal force of 64 N have been obtained.

In addition to the actuator, a thermomechanical model of its SMA wire transducer has also been developed. This model is capable of simulating the complex behavior of these materials and the interdependence of the variables that define their operation. In the experimental tests conducted in Chapter 4 we have seen how the model reproduces several of the particular effects displayed by these alloys such as the endothermic and exothermic processes caused by the latent heat of transformation, the variation of the electrical resistance depending on the temperature and the length of the wire, the internal hysteresis loops and the return-point memory. The comparison of the modeled SMA wire with its real counterpart has yielded very positive results, showing great similarities between the responses obtained in both cases.

To control the designed actuator, we have implemented a non-linear control technique called four-term bilinear PID controller. This technique consists of a modification of a conventional PID controller whose output is multiplied by an additional term. This term linearizes the plant allowing the use of linear control techniques on a non-linear system such as an SMA wire. In Chapter 5 the validity of this control technique has been demonstrated through a series of tests in which its performance has been compared to that of two other controllers. Although the BPID controller makes the power consumption of the SMA actuator slightly higher, this technique outperforms the other two tested strategies in terms of accuracy and stability.

Finally, since the scope of the proposed actuator is the field of soft wearable robotics, in Chapter 6 it has been used to implement the actuation system of the HEMS, a hand exoskeleton designed to assist astronauts during EVA missions. The actuator has been improved by including a displacement multiplication mechanism that allows the SMA wire length to be reduced by half, with the downside of also reducing the force generated by half. A force sensor has also been integrated, allowing the BPID controller to be applied to the control of the force generated by the actuator. The results obtained with respect to the control of the exoskeleton, both in position and in force, have been very satisfactory. Finally, regarding the performance of the SMA actuator with respect to the requirements of the exoskeleton, the results obtained in the characterization tests of the HEMS actuation system suggest that the designed device is capable of providing at least 50 % of the force needed to overcome the opposing forces of a spacesuit glove.

7.1 Future works

Actuator design

Despite the improvement in the actuation bandwidth thanks to the heat sink effect of the Bowden sheath, the actuator speed during the cooling phase of the SMA transducer is still somewhat reduced. Also, during the integration tests with the HEMS exoskeleton, an effect has been observed which has a negative impact on the operation of the actuator. After several continuous actuation cycles, some of the heat from the SMA wire accumulates in the multilayer sheath, causing the cooling time to slightly increase.

We believe that this flexible SMA actuator concept has opened a design space that has to be further explored to solve some of the limiting factors of SMA actuators still present in the current design. The cooling time could be greatly improved with a new actuator design consisting of several thinner wires mechanically arranged in parallel, each of them routed inside an individual small diameter multilayer Bowden sheath. The combination of the lower cooling time of thinner wires with the improved heat rejection provided by the sheath would significantly increase the actuation bandwidth and, as they would be arranged in parallel, the combined forces of each wire would equal the force of a single larger diameter wire.

SMA wire model

As we already mentioned in Chapter 4, due to the complexity of modeling the influence of the Bowden sheath on the transducer thermal processes, this effect has not been included in the developed model and only the SMA transducer of the designed actuator has been modeled. Therefore, a possible future line of work would be the development of a model of the complete actuator, including the thermal effects (increased heat rejection and heat build-up over the course of several actuation cycles) as well as the mechanical effects (frictional losses depending on the bending angle of the sheath).

Actuator control

One of the downsides of the BPID controller is that, among the three tested controllers in Chapter 5, it is the one which produces the greatest variations in the input power of the actuator, which might affect its service life. The mean absolute control signal increment (MACSI) value of the BPID controller is the greatest of the three controllers in all the performed experiments. As defined above, the MACSI value measures the amplitude of the variations of the control signal which are directly related to the fluctuations of the electrical power delivered to the SMA actuator. It might be assumed that the higher the variation of the input power, the shorter the service life of the actuator, since the thermal cycles to which it is subjected have a greater temperature difference. This entails a bigger change in the martensite fraction of the material, that is, a greater change in the crystal structure of the material, that eventually would lead to the emergence of microcracks that would permanently damage the actuator. Still, it has to be assessed to what extent the fluctuations of the control signal have an impact on the service life of the SMA actuator. In addition, the fact that the control signal computed by the BPID controller has a greater variation and that, consequently, the actuator has a higher energy consumption, has a positive impact in the controller performance, since it means that it is the most active of the three, which leads to a smoother and more accurate response.

HEMS exoskeleton

Additional experiments should be performed with the HEMS, ideally using a real EVA glove, to assess the extent to which its the stiffness is reduced and to experimentally obtain the amount of assistive force provided by the exoskeleton. In addition, in order for the HEMS to fulfill its intended purpose, a high-level controller should be implemented to allow the user to operate it. In order to provide an assistive force proportional to that exerted by the user, the interaction forces between the wearer and the glove should be measured using, for example, fingertip pressure sensors. This information would be processed by the high-level controller that would generate the necessary commands for the low-level controllers of the actuators so that they exert the required force.

Although the HEMS has been designed according to the soft exoskeleton design paradigm, there are still some rigid and bulky elements that should be redesigned in order to integrate the device into an EVA spacesuit. For example, the shoulder modules that serve as the attachment point of the fixed end of the actuators have a rather high volume, mainly because of the size of the force sensors they house. This could be easily solved by using a small compression load cell and redesigning the fixed end of the actuators to integrate it. The other element that must be redesigned in order for the HEMS to better comply with the design principles of soft exoskeletons is the sliding platform mechanism that keeps the distance between the base of the fingers and the output of the actuators constant regardless of the position of the hand. Not only this mechanism is rigid, but also adds some complexity to the device and increases the risk of mechanical failure. One possible solution would be to apply the same design concept as in the actuator design, connecting the output of the actuators with the base of the fingers by means of small diameter flexible sheaths fixed to a compliant piece sewn to the palm of the HEMS internal glove.

As a final note, this device, with some modifications, could be used for tasks other than assisting astronauts on EVA missions. For example, its application as a rehabilitation soft exoskeleton is pretty straightforward. The restoring force needed by the SMA actuators to recover their initial length could be provided by set of antagonistic springs, similarly to the configuration used in the test bench employed in the experiments. Also, six additional actuators in antagonistic configuration could be used so that the finger extension movement would also be active. In this case, since rehabilitation exercises generally do not require fast movements, the actuation frequency would not be as critical as in the application presented in this thesis.

Bibliography

[1] J. L. Pons, ed., *Wearable Robots: Biomechatronic Exoskeletons*. John Wiley & Sons Ltd, 2008.

[2] C. Majidi, “Soft robotics: a perspective - Current trends and prospects for the future,” *Soft Robotics*, vol. 1, no. 1, pp. 5–11, 2014.

[3] C. Laschi and M. Cianchetti, “Soft robotics: new perspectives for robot bodyware and control,” *Frontiers in bioengineering and biotechnology*, vol. 2, p. 3, 2014.

[4] D. Trivedi, C. D. Rahn, W. M. Kier, and I. D. Walker, “Soft robotics: biological inspiration, state of the art, and future research,” *Applied Bionics and Biomechanics*, vol. 5, no. 3, pp. 99–117, 2008.

[5] S. Kim, E. Hawkes, K. Choy, M. Joldaz, J. Foleyz, and R. Wood, “Micro artificial muscle fiber using NiTi spring for soft robotics,” in *IEEE/RSJ International Conference on Intelligent Robots and Systems, IROS 2009.*, pp. 2228–2234, IEEE, 2009.

[6] B. Trimmer, “A practical approach to soft actuation [Editorial],” *Soft Robotics*, vol. 4, pp. 1–2, mar 2017.

[7] F. Iida and C. Laschi, “Soft robotics: challenges and perspectives,” *Procedia Computer Science*, vol. 7, pp. 99–102, 2011.

[8] S. Kim, C. Laschi, and B. Trimmer, “Soft robotics: a bioinspired evolution in robotics,” *Trends in biotechnology*, vol. 31, no. 5, pp. 287–294, 2013.

[9] J. M. Jani, M. Leary, A. Subic, and M. A. Gibson, “A review of shape memory alloy research, applications and opportunities,” *Materials and Design*, vol. 56, pp. 1078–1113, 2014.

[10] J. L. Pons, *Emerging actuator technologies: a micromechatronic approach*. John Wiley & Sons Ltd, 2005.

[11] H. In, B. B. Kang, M. Sin, and K.-J. Cho, "Exo-Glove: A wearable robot for the hand with a soft tendon routing system," *IEEE Robotics & Automation Magazine*, vol. 22, pp. 97–105, Mar 2015.

[12] B. B. Kang, H. Lee, H. In, U. Jeong, J. Chung, and K. Cho, "Development of a polymer-based tendon-driven wearable robotic hand," in *2016 IEEE International Conference on Robotics and Automation (ICRA)*, pp. 3750–3755, May 2016.

[13] M. Nilsson, J. Ingvast, J. Wikander, and H. von Holst, "The Soft Extra Muscle system for improving the grasping capability in neurological rehabilitation," in *2012 IEEE-EMBS Conference on Biomedical Engineering and Sciences*, pp. 412–417, Dec 2012.

[14] D. Fausti and C. Seneci, "Hand rehabilitation device," Mar 2013.

[15] M. A. Delph, S. A. Fischer, P. W. Gauthier, C. H. M. Luna, E. A. Clancy, and G. S. Fischer, "A soft robotic exomusculature glove with integrated sEMG sensing for hand rehabilitation," in *2013 IEEE 13th International Conference on Rehabilitation Robotics (ICORR)*, pp. 1–7, Jun 2013.

[16] C. J. Nycz, M. A. Delph, and G. S. Fischer, "Modeling and design of a tendon actuated soft robotic exoskeleton for hemiparetic upper limb rehabilitation," in *2015 37th Annual International Conference of the IEEE Engineering in Medicine and Biology Society (EMBC)*, pp. 3889–3892, Aug 2015.

[17] H. In, K.-J. Cho, K. Kim, and B. Lee, "Jointless structure and under-actuation mechanism for compact hand exoskeleton," in *2011 IEEE International Conference on Rehabilitation Robotics*, pp. 1–6, Jun 2011.

[18] E. Thompson-Bean, O. Steiner, and A. McDaid, "A soft robotic exoskeleton utilizing granular jamming," in *2015 IEEE International Conference on Advanced Intelligent Mechatronics (AIM)*, pp. 165–170, July 2015.

[19] P. Polygerinos, Z. Wang, K. C. Galloway, R. J. Wood, and C. J. Walsh, "Soft robotic glove for combined assistance and at-home rehabilitation," *Robotics and Autonomous Systems*, vol. 73, pp. 135–143, Nov 2015.

[20] P. Polygerinos, K. C. Galloway, E. Savage, M. Herman, K. O. Donnell, and C. J. Walsh, "Soft robotic glove for hand rehabilitation and task specific training," in *2015 IEEE International Conference on Robotics and Automation (ICRA)*, pp. 2913–2919, May 2015.

[21] P. Polygerinos, K. C. Galloway, S. Sanan, M. Herman, and C. J. Walsh, "EMG controlled soft robotic glove for assistance during activities of daily living," in *2015 IEEE International Conference on Rehabilitation Robotics (ICORR)*, pp. 55–60, Aug 2015.

[22] H. K. Yap, J. H. Lim, F. Nasrallah, J. C. H. Goh, and R. C. H. Yeow, "A soft exoskeleton for hand assistive and rehabilitation application using pneumatic actuators with variable stiffness," in *2015 IEEE International Conference on Robotics and Automation (ICRA)*, pp. 4967–4972, May 2015.

[23] S.-S. Yun, B. B. Kang, and K.-J. Cho, "Exo-glove PM: An easily customizable modularized pneumatic assistive glove," *IEEE Robotics and Automation Letters*, vol. 5, no. 3, pp. 1725–1732, 2017.

[24] K. C. Galloway, P. Polygerinos, C. J. Walsh, and R. J. Wood, "Mechanically programmable bend radius for fiber-reinforced soft actuators," in *2013 16th International Conference on Advanced Robotics (ICAR)*, pp. 1–6, Nov 2013.

[25] P. Maeder-York, T. Clites, E. Boggs, R. Neff, P. Polygerinos, D. Holland, L. Stirling, K. Galloway, C. Wee, and C. Walsh, "Biologically inspired soft robot for thumb rehabilitation," *Journal of Medical Devices*, vol. 8, pp. (020933)1–(020933)3, Apr 2014.

[26] A. T. Asbeck, R. J. Dyer, A. F. Larusson, and C. J. Walsh, "Biologically-inspired soft exosuit," in *2013 IEEE International Conference on Rehabilitation Robotics (ICORR)*, pp. 1–8, 2013.

[27] A. T. Asbeck, S. M. M. De Rossi, I. Galiana, Y. Ding, and C. J. Walsh, "Stronger, smarter, softer: next-generation wearable robots," *IEEE Robotics & Automation Magazine*, vol. 21, no. 4, pp. 22–33, 2014.

[28] A. T. Asbeck, K. Schmidt, and C. J. Walsh, "Soft exosuit for hip assistance," *Robotics and Autonomous Systems*, vol. 73, pp. 102–110, 2014.

[29] A. T. Asbeck, S. M. M. D. Rossi, K. G. Holt, and C. J. Walsh, "A biologically inspired soft exosuit for walking assistance," *International Journal of Robotics Research*, vol. 34, no. 6, pp. 744–762, 2015.

[30] Y. Park, B. Chen, D. Young, L. Stirling, R. J. Wood, E. Goldfield, and R. Nagpal, "Bio-inspired active soft orthotic device for ankle foot pathologies," in *2011 IEEE/RSJ International Conference on Intelligent Robots and Systems*, pp. 4488–4495, Sep. 2011.

[31] Y.-L. Park, B. rong Chen, N. O. Pérez-Arancibia, D. Young, L. Stirling, R. J. Wood, E. C. Goldfield, and R. Nagpal, "Design and control of a bio-inspired soft wearable robotic device for ankle-foot rehabilitation," *Bioinspiration & Biomimetics*, vol. 9, no. 1, pp. 1–17, 2014.

[32] M. Wehner, B. Quinlivan, P. M. Aubin, E. Martinez-Villalpando, M. Baumann, L. Stirling, K. Holt, R. Wood, and C. Walsh, "A lightweight soft exosuit for gait assistance," in *2013 IEEE International Conference on Robotics and Automation*, pp. 3362–3369, May 2013.

[33] C. Walsh, K. Endo, and H. Herr, "A quasi-passive leg exoskeleton for load-carrying augmentation," *International Journal of Humanoid Robotics*, vol. 4, no. 3, pp. 487–506, 2007.

[34] A. Villoslada, A. Flores, D. Copaci, D. Blanco, and L. Moreno, "High-displacement flexible Shape Memory Alloy actuator for soft wearable robots," *Robotics and Autonomous Systems*, vol. 73, pp. 91–101, Nov 2015.

[35] A. Villoslada, A. Flores, D. Copaci, D. Blanco, and L. Moreno, "High-displacement fast-cooling flexible Shape Memory Alloy actuator: Application to an anthropomorphic robotic hand," in *2014 14th IEEE-RAS International Conference on Humanoid Robots (Humanoids)*, pp. 27–32, Nov 2014.

[36] A. Villoslada, N. Escudero, F. Martín, A. Flores, C. Rivera, M. Collado, and L. Moreno, "Position control of a shape memory alloy actuator using a four-term bilinear PID controller," *Sensors and Actuators A: Physical*, vol. 236, pp. 257–272, Dec 2015.

[37] A. Villoslada, C. Rivera, N. Escudero, F. Martín, D. Blanco, and L. Moreno, "Hand exo-muscular system for assisting astronauts during Extravehicular Activities," *Soft Robotics*, vol. 6, no. 1, pp. 21–37, 2019.

[38] G. V. Kurdyumov and L. G. Khandros, "On the thermoelastic equilibrium on martensitic transformations," *Doklady Akademii Nauk SSSR*, vol. 66, no. 2, pp. 211–214, 1949.

[39] A. Ölander, "An electrochemical investigation of solid cadmium-gold alloys," *Journal of the American Chemical Society*, vol. 54, pp. 3819–3833, Oct. 1932.

[40] W. A. Rachinger, "A "super-elastic" single crystal calibration bar," *British Journal of Applied Physics*, vol. 9, pp. 250–252, June 1958.

[41] L. C. Chang and T. A. Read, "Plastic deformation and diffusionless phase changes in metals - the gold-cadmium beta phase," *Journal of Metals*, vol. 3, no. 1, pp. 47–52, 1951.

[42] J. E. Reynolds and M. B. Bever, "On the reversal of the strain induced martensitic transformation in the Copper-Zinc system," *Journal of Metals*, p. 1065, 1952.

[43] M. W. Burkart and T. A. Read, "Diffusionless phase change in the Indium-Thallium system," *Journal of Metals*, vol. 5, pp. 1516–1524, 1953.

[44] R. M. Genevray, *Martensitic transformation in muntz metal.* PhD thesis, MIT, May 1953.

[45] E. J. Suoninen, *An investigation of martensitic transformation in metastable beta brass.* PhD thesis, MIT, Aug. 1954.

[46] C. W. Chen, "Some characteristics of the martensite transformation of Cu-Al-Ni alloys," *Journal of Metals*, vol. 9, pp. 1202–1203, Oct. 1957.

[47] L. Muldawer and R. Feder, "Temperature responsive Cadmium-Silver-Gold alloys," 1961.

[48] C. M. Wayman and J. D. Harrison, "The origins of the shape memory effect," *Journal of Metals*, vol. 41, pp. 26–28, Sept. 1989.

[49] W. Buehler and R. Wiley, "The properties of TiNi and associated phases," tech. rep., U. S. Naval Ordnance Laboratory, 1961.

[50] W. J. Buehler. Personal communication, Aug. 1991.

[51] W. J. Buehler. Letter to A. A. Hanson, June 1991.

[52] F. E. Wang, W. J. Buehler, and S. J. Pickart, "Crystal structure and a unique martensitic transformation of TiNi," *Journal of Applied Physics*, vol. 36, pp. 3232–3239, 1965.

[53] C. M. Jackson, H. J. Wagner, and R. J. Wasilewski, "55-Nitinol - The alloy with a memory: its physical metallurgy, properties and applications," techreport, NASA Technology Utilization Office, 1972.

[54] Aerofit, Inc., *Shape Memory Alloy (SMA) Fluid Fitting System.*

[55] M. H. Wu and L. M. Schetky, "Industrial applications for shape memory alloys," in *Proceedings of the International Conference on Shape Memory and Superelastic Technologies*, 2000.

[56] H. C. Doonkersloot and V. Vucht, “Martensitic transformation in Au-Ti, Pd-Ti and Pt-Ti alloys,” *Journal of Less-Common Metals*, vol. 20, pp. 83–91, 1970.

[57] K. Ullakko, J. K. Huang, C. Kantner, R. C. O’Handley, and V. V. Kokorin, “Large magnetic-field-induced strains in Ni_2MnGa single crystals,” *Applied Physics Letters*, vol. 69, no. 13, pp. 1966–1968, 1996.

[58] H. E. Karaca, I. Karaman, B. Basaran, Y. I. Chumlyakov, and H. J. Maier, “Magnetic field and stress induced martensite reorientation in NiMnGa ferromagnetic shape memory alloy single crystals,” *Acta Materialia*, vol. 54, no. 1, pp. 233–245, 2006.

[59] G. Andreasen and T. Hilleman, “An evaluation of 55 cobalt substituted nitinol wire for use in orthodontics,” *Journal of the American Dental Association*, vol. 82, pp. 1373–1375, 1971.

[60] N. Pandis and C. P. Bourauel, “Nickel-Titanium (NiTi) arch wires: the clinical significance of super elasticity,” *Seminars in Orthodontics*, vol. 16, pp. 249–257, Dec. 2010.

[61] S. Tyagi, S. Singh, S. Mukhopadhyay, and U. A. Kaul, “Self- and balloon-expandable stent implantation for severe native coarctation of aorta in adults,” *American Heart Journal*, vol. 146, no. 5, pp. 920–928, 2003.

[62] B. D. Thanopoulos, C. V. Laskari, G. S. Tsaousis, A. Zarayelyan, A. Vekiou, and G. S. Papadopoulos, “Closure of atrial septal defects with the amplatzer occlusion device: preliminary results,” *Journal of the American College of Cardiology*, vol. 31, no. 5, pp. 1110–1116, 1998.

[63] W. Small, T. S. Wilson, P. R. Buckley, W. J. Benett, J. M. Loge, J. Hartman, and D. J. Maitland, “Prototype fabrication and preliminary in vitro testing of a shape memory endovascular thrombectomy device,” *IEEE Transactions on Biomedical Engineering*, vol. 54, no. 9, pp. 1657–1666, 2007.

[64] K. Yamauchi, T. Kugo, and Y. Miyano, “Catheter guidewire with pseudo elastic shape memory alloy,” 1991.

[65] Z. Laster, A. D. MacBean, P. R. Ayliffe, and L. C. Newlands, “Fixation of a frontozygomatic fracture with a shape-memory staple,” *British Journal of Oral and Maxillofacial Surgery*, vol. 39, no. 4, pp. 324–325, 2001.

[66] M. A. Schmerling, M. A. Wilkor, A. E. Sanders, and J. E. Woosley, “A proposed medical application of the shape memory effect: an Ni-Ti Harrington rod

for treatment of scoliosis," *Journal of Biomedical Materials Research*, vol. 10, pp. 879–902, 1976.

[67] R. DesRoches and M. Delemont, "Seismic retrofit of simply supported bridges using shape memory alloys," *Engineering Structures*, vol. 24, no. 3, pp. 325–332, 2002.

[68] M. Speicher, D. Hodgson, R. DesRoches, and R. Leon, "Shape memory alloy tension/compression device for seismic retrofit of buildings," *Journal of Materials Engineering and Performance*, vol. 18, no. 5, pp. 746–753, 2009.

[69] M. Indirli, M. G. Castellano, P. Clemente, and A. Martelli, "Demo-application of shape memory alloy devices: the rehabilitation of the S. Giorgio Church bell tower," in *Smart Structures and Materials 2001: Smart Systems for Bridges, Structures, and Highways*, vol. 4330, pp. 262–272, SPIE, 2001.

[70] Y. Mo, G. Song, and K. Otero, "Development and testing of a proof-of-concept smart concrete structure," in *Proceedings of smart structures technologies and earthquake engineering*, 2004.

[71] R. G. Loewy, "Recent developments in smart structures with aeronautical applications," *Smart Materials and Structures*, vol. 6, no. 5, pp. 11–42, 1997.

[72] J. K. Strelec, D. C. Lagoudas, M. A. Khan, and J. Yen, "Design and implementation of a shape memory alloy actuated reconfigurable airfoil," *Journal of Intelligent Material Systems and Structures*, vol. 14, no. 4-5, pp. 257–273, 2003.

[73] D. J. Hartl and D. C. Lagoudas, "Aerospace applications of shape memory alloys," *Proceedings of the Institution of Mechanical Engineers, Part G: Journal of Aerospace Engineering*, vol. 221, no. 4, pp. 535–552, 2007.

[74] I. Chopra, "Status of application of smart structures technology to rotorcraft systems," *Journal of the American Helicopter Society*, vol. 45, no. 4, pp. 228–252, 2000.

[75] O. J. Godard, M. Z. Lagoudas, and D. C. Lagoudas, "Design of space systems using shape memory alloys," in *Smart Structures and Materials 2003: Smart Structures and Integrated Systems*, vol. 5056, pp. 545–558, 2003.

[76] G. Costanza and M. E. Tata, "A novel methodology for solar sail opening employing shape memory alloy elements," *Journal of Intelligent Material Systems and Structures*, vol. 29, no. 9, pp. 1793–1798, 2018.

[77] L. M. Schetky, "Shape memory alloy applications in space systems," *Materials & Design*, vol. 12, no. 1, pp. 29–32, 1991.

[78] J. W. Jeong, K. C. Shin, K. W. Kim, J. H. Lim, and J. J. Lee, "SMA damped tape spring hinge for quasi-static deployment of a satellite solar array," *Applied Mechanics and Materials*, vol. 705, pp. 96–100, 2015.

[79] C.-H. Lee, J.-W. Jeong, Y.-J. Kim, and J.-J. Lee, "Deployment shock attenuation of a solar array tape hinge by means of the martensite detwinning of NiTi shape memory alloy," *Review of Scientific Instruments*, vol. 87, no. 3, pp. 1–9, 2016.

[80] P. P. Jenkins and G. A. Landis, "A rotating arm using shape-memory alloy," in *NASA. Johnson Space Center, The 29th Aerospace Mechanisms Symposium*, pp. 167–171, 1995.

[81] K. Otsuka and T. Kakeshita, "Science and technology of shape-memory alloys: New developments," *MRS Bulletin*, vol. 27, no. 2, pp. 91–100, 2002.

[82] A. Bellini, M. Colli, and E. Dragoni, "Mechatronic design of a shape memory alloy actuator for automotive tumble flaps: A case study," *IEEE Transactions on Industrial Electronics*, vol. 56, no. 7, pp. 2644–2656, 2009.

[83] P. K. Kumar and D. C. Lagoudas, *Shape Memory Alloys - Modeling and Engineering Applications*, ch. 1, pp. 19–51. Springer US, 2008.

[84] B. Barnes, D. Brei, J. Luntz, A. Browne, and K. Strom, "Panel deployment using ultrafast SMA latches," in *Proceedings of the ASME International Mechanical Engineering Congress and Exposition*, pp. 273–280, 2006.

[85] F. Butera, M. Biasiotto, and S. Alacqua, "Actuator device with a flexible cable incorporating a shape-memory element," 2004.

[86] DYNALLOY, Inc., *Technical Characteristics of Flexinol Actuator Wires*, 2014.

[87] R. J. Wasilewski, "On the nature of the martensitic transformation," *Metallurgical Transactions A*, vol. 6, no. 7, pp. 1405–1418, 1975.

[88] K. Otsuka and C. M. Wayman, *Shape Memory Materials*, ch. 1, pp. 1–26. Cambridge University Press, 1998.

[89] J. Ortín, A. Planes, and L. Delaey, *The Science of Hysteresis*, vol. 3, ch. 5, pp. 467–553. Academic Press Oxford, 2005.

[90] J. Ortín and A. Planes, "Thermodynamic analysis of thermal measurements in thermoelastic martensitic transformations," *Acta metallurgica*, vol. 36, no. 8, pp. 1873–1889, 1988.

[91] J. Ortín and A. Planes, "Thermodynamics of thermoelastic martensitic transformations," *Acta Metallurgica*, vol. 37, no. 5, pp. 1433–1441, 1989.

[92] J. V. Humbeeck, E. Aernoudt, L. Delaey, L. Li, H. Verguts, and J. Ortín, "Hysteretic transformation behaviour of shape memory alloys," *Revue de Physique Appliquée*, vol. 23, pp. 557–564, 1988.

[93] M. Zarinejad and Y. Liu, "Dependence of transformation temperatures of NiTi-based shape-memory alloys on the number and concentration of valence electrons," *Advanced Functional Materials*, vol. 18, pp. 1–6, 2008.

[94] J. Van Humbeeck and R. Stalmans, *Shape Memory Materials*, ch. 7, pp. 149–183. Cambridge University Press, 1998.

[95] C. Cisse, W. Zaki, and T. B. Zineb, "A review of constitutive models and modeling techniques for shape memory alloys," *International Journal of Plasticity*, vol. 76, pp. 244–284, 2016.

[96] K. Tanaka, "A thermomechanical sketch of shape memory effect: one-dimensional tensile behavior," *Res Mechanica: International Journal of Structural Mechanics and Materials Science*, vol. 18, no. 3, pp. 251–263, 1986.

[97] C. Liang and C. A. Rogers, "One-dimensional thermomechanical constitutive relations for shape memory materials," *Journal of intelligent material systems and structures*, vol. 1, no. 2, pp. 207–234, 1990.

[98] L. C. Brinson, "One-dimensional constitutive behavior of shape memory alloys: thermomechanical derivation with non-constant material functions and redefined martensite internal variable," *Journal of intelligent material systems and structures*, vol. 4, no. 2, pp. 229–242, 1993.

[99] Y. Ivshin and T. J. Pence, "A thermomechanical model for a one variant shape memory material," *Journal of intelligent material systems and structures*, vol. 5, no. 4, pp. 455–473, 1994.

[100] J. G. Boyd and D. C. Lagoudas, "A thermodynamical constitutive model for shape memory materials. part i. the monolithic shape memory alloy," *International Journal of Plasticity*, vol. 12, no. 6, pp. 805–842, 1996.

[101] A. Visintin, *The Science of Hysteresis*, vol. 1, ch. 1, pp. 1–123. Academic Press Oxford, 2005.

[102] Z. Bo and D. C. Lagoudas, "Thermomechanical modeling of polycrystalline smas under cyclic loading, part iv: Modeling of minor hysteresis loops," *International Journal of Engineering Science*, vol. 37, no. 9, pp. 1205–1249, 1999.

[103] P. Duhem, "Die dauernden aenderungen und die thermodynamik, I," *Zeitschrift für Physikalische Chemie*, vol. 22, no. 1, pp. 545–589, 1897.

[104] A. Visintin, *Differential models of hysteresis*, vol. 111, ch. 5, pp. 130–150. Springer-Verlag Berlin Heidelberg, 1994.

[105] R. Bouc, "Forced vibration of mechanical systems with hysteresis," in *Proceedings of the fourth conference on non-linear oscillation, Prague, Czechoslovakia*, 1967.

[106] Y.-K. Wen, "Method for random vibration of hysteretic systems," *Journal of the engineering mechanics division*, vol. 102, no. 2, pp. 249–263, 1976.

[107] S. M. Dutta and F. H. Ghorbel, "Differential hysteresis modeling of a shape memory alloy wire actuator," *IEEE/ASME Transactions on Mechatronics*, vol. 10, pp. 189–197, April 2005.

[108] Y. Feng, C. A. Rabbath, and C.-Y. Su, "Inverse duhem model based robust adaptive control for flap positioning system with sma actuators," *IFAC Proceedings Volumes*, vol. 44, no. 1, pp. 8126–8131, 2011.

[109] S.-H. Liu, T.-S. Huang, and J.-Y. Yen, "Tracking control of shape-memory-alloy actuators based on self-sensing feedback and inverse hysteresis compensation," *Sensors*, vol. 10, no. 1, pp. 112–127, 2010.

[110] A. Likhachev and Y. N. Koval, "On the differential equation describing the hysteretic behavior of shape-memory alloys," *Scripta metallurgica et materialia*, vol. 27, no. 2, pp. 223–227, 1992.

[111] A. Likhachev, "Differential equation of hysteresis: Application to partial martensitic transformation in shape-memory alloys," *Scripta metallurgica et materialia*, vol. 32, no. 4, pp. 633–636, 1995.

[112] A. Likhachev and Y. N. Koval, "The model of hysteretic behavior of sma based on the high order approximation of differential equation method," *Le Journal de Physique IV*, vol. 7, no. C5, pp. C5–77, 1997.

[113] F. Preisach, “Über die magnetische nachwirkung,” *Zeitschrift für Physik A Hadrons and Nuclei*, vol. 94, no. 5, pp. 277–302, 1935.

[114] M. A. Krasnosel’skii and A. V. Pokrovskii, *Systems with hysteresis.* Springer-Verlag Berlin Heidelberg, 1989.

[115] L. Prandtl, “Ein gedankenmodell zur kinetischen theorie der festen körper,” *ZAMM-Journal of Applied Mathematics and Mechanics/Zeitschrift für Angewandte Mathematik und Mechanik*, vol. 8, no. 2, pp. 85–106, 1928.

[116] A. Y. Ishlinskii, “Some applications of statistical methods to describing deformations of bodies,” *Izv. AN SSSR Technical Series*, vol. 9, pp. 580–590, 1944.

[117] D. Carnevale, S. Nicosia, and L. Zaccarian, “A differential hysteresis model,” *IFAC Proceedings Volumes*, vol. 38, no. 1, pp. 301–306, 2005.

[118] E. Asua, V. Etxebarria, and A. García-Arribas, “Neural network-based micropositioning control of smart shape memory alloy actuators,” *Engineering Applications of Artificial Intelligence*, vol. 21, no. 5, pp. 796–804, 2008.

[119] N. Ma, G. Song, and H. Lee, “Position control of shape memory alloy actuators with internal electrical resistance feedback using neural networks,” *Smart materials and structures*, vol. 13, no. 4, p. 777, 2004.

[120] I. J. Busch-Vishniac, *Electromechanical sensors and actuators.* Springer Science & Business Media, 1999.

[121] J. D. Ertel and S. A. Mascaro, “Dynamic thermomechanical modeling of a wet shape memory alloy actuator,” *Journal of Dynamic Systems, Measurement, and Control*, vol. 132, pp. 1–9, 2010.

[122] S. Pittaccio, S. Viscuso, M. Rossini, L. Magoni, S. Pirovano, E. Villa, S. Besseghini, and F. Molteni, “SHADE: A shape-memory-activated device promoting ankle dorsiflexion,” *Journal of Materials Engineering and Performance*, vol. 18, pp. 824–830, 2009.

[123] K. Andrianesis, Y. Koveos, G. Nikolakopoulos, and A. Tzes, *Shape Memory Alloys*, ch. Experimental Study of a Shape Memory Alloy Actuation System for a Novel Prosthetic Hand, pp. 81–106. Sciyo, 2010.

[124] K. Andrianesis and A. Tzes, “Design of an innovative prosthetic hand with compact shape memory alloy actuators,” in *21st Mediterranean Conference on Control & Automation (MED)*, pp. 697–702, 2013.

[125] G. Mammano and E. Dragoni, "Design and characterization of a continuous rotary minimotor based on shape-memory wires and overrunning clutches," *Journal of Mechanical Design*, vol. 139, no. 1, pp. 1–9, 2016.

[126] G. Song, "Design and control of a Nitinol wire actuated rotary servo," *Smart Materials and Structures*, vol. 16, no. 5, pp. 1796–1801, 2007.

[127] H. Taniguchi, "Flexible artificial muscle actuator using coiled shape memory alloy wires," *APCBEE Procedia*, vol. 7, pp. 54–59, 2013.

[128] Y. She, C. Li, J. Cleary, and H. Su, "Design and fabrication of a soft robotic hand with embedded actuators and sensors," *Journal of Mechanisms and Robotics*, vol. 7, no. 2, pp. 1–9, 2015.

[129] Y. She, J. Chen, H. Shi, and H.-J. Su, "Modeling and validation of a novel bending actuator for soft robotics applications," *Soft Robotics*, vol. 3, no. 2, pp. 71–81, 2016.

[130] A. Villanueva, C. Smith, and S. Priya, "A biomimetic robotic jellyfish (Robojelly) actuated by shape memory alloy composite actuators," *Bioinspiration & Biomimetics*, vol. 6, no. 3, pp. 1–16, 2011.

[131] S. Mao, E. Dong, H. Jin, M. Xu, S. Zhang, J. Yang, and K. H. Low, "Gait study and pattern generation of a starfish-like soft robot with flexible rays actuated by SMAs," *Journal of Bionic Engineering*, vol. 11, no. 3, pp. 400–411, 2014.

[132] W. Wang, J.-Y. Lee, H. Rodrigue, S.-H. Song, W.-S. Chu, and S.-H. Ahn, "Locomotion of inchworm-inspired robot made of smart soft composite (SSC)," *Bioinspiration & Biomimetics*, vol. 9, no. 4, pp. 1–10, 2014.

[133] S.-H. Ahn, K.-T. Lee, H.-J. Kim, R. Wu, J.-S. Kim, and S.-H. Song, "Smart soft composite: An integrated 3D soft morphing structure using bend-twist coupling of anisotropic materials," *International Journal of Precision Engineering and Manufacturing*, vol. 13, no. 4, pp. 631–634, 2012.

[134] H.-J. Kim, S.-H. Song, and S.-H. Ahn, "A turtle-like swimming robot using a smart soft composite (SSC) structure," *Smart Materials and Structures*, vol. 22, no. 1, pp. 1–11, 2012.

[135] H. Rodrigue, W. Wang, B. Bhandari, M.-W. Han, and S.-H. Ahn, "Cross-shaped twisting structure using SMA-based smart soft composite," *International Journal of Precision Engineering and Manufacturing-Green Technology*, vol. 1, no. 2, pp. 153–156, 2014.

[136] H. Rodrigue, B. Bhandari, M.-W. Han, and S.-H. Ahn, "A shape memory alloy-based soft morphing actuator capable of pure twisting motion," *Journal of Intelligent Material Systems and Structures*, vol. 26, no. 9, pp. 1071–1078, 2015.

[137] S.-H. Song, J.-Y. Lee, H. Rodrigue, I.-S. Choi, Y. J. Kang, and S.-H. Ahn, "35 Hz shape memory alloy actuator with bending-twisting mode," *Scientific Reports*, vol. 6, pp. 1–13, 2016.

[138] W. Wang, H. Rodrigue, and S.-H. Ahn, "Deployable soft composite structures," *Scientific Reports*, vol. 6, pp. 1–10, 2016.

[139] T. Duerig, K. Melton, and J. Proft, "Wide hysteresis shape memory alloys," *Engineering aspects of shape memory alloys*, pp. 130–136, 1990.

[140] H. J. Lee and J. J. Lee, "Time delay control of a shape memory alloy actuator," *Smart Materials and Structures*, vol. 13, no. 1, pp. 227–239, 2004.

[141] H. Sayyaadi and M. R. Zakerzadeh, "Position control of shape memory alloy actuator based on the generalized Prandtl-Ishlinski inverse model," *Mechatronics*, vol. 22, no. 7, pp. 945–957, 2012.

[142] E. P. Da Silva, "Beam shape feedback control by means of a shape memory actuator," *Materials & Design*, vol. 28, pp. 1592–1596, 2007.

[143] E. Asua, V. Etxebarria, and A. García-Arribas, "Micropositioning control using shape memory alloys," in *Proceedings of 2006 IEEE Conference on Control Applications, CCA 2006*, (Munich, Germany), pp. 3229–3234, 2006.

[144] S. M. Yang, J. H. Roh, J. H. Han, and I. Lee, "Experimental studies on active shape control of composite structures using SMA actuators," *Journal of Intelligent Material Systems and Structures*, vol. 17, no. 8-9, pp. 767–777, 2006.

[145] A. V. Popov, M. Labib, J. Fays, and R. M. Botez, "Closed-loop control simulations on a morphing wing," *Journal of Aircraft*, vol. 45, no. 5, pp. 1794–1803, 2008.

[146] N. Ma and G. Song, "Control of shape memory alloy actuator using pulse width modulation," *Smart Materials and Structures*, vol. 12, pp. 712–719, Sep 2003.

[147] G. Song and N. Ma, "Control of shape memory alloy actuators using pulse-width pulse-frequency (PWPF)," *Journal of Intelligent Material Systems and Structures*, vol. 14, no. 1, pp. 15–22, 2003.

[148] E. Shameli, A. Alasty, and H. Salaarieh, “Stability analysis and nonlinear control of a miniature shape memory alloy actuator for precise applications,” *Mechatronics*, vol. 15, no. 4, pp. 471–486, 2005.

[149] J. Jayender, R. V. Patel, S. Nikumb, and M. Ostojic, “Modelling and gain scheduled control of shape memory alloy actuators,” in *Proceedings of 2005 IEEE Conference on Control Applications, CCA 2005.*, pp. 767–772, 2005.

[150] J. Jayender, R. V. Patel, S. Nikumb, and M. Ostojic, “Modeling and Control of Shape Memory Alloy Actuators,” *IEEE Transactions on Control Systems Technology*, vol. 16, no. 2, pp. 279–287, 2008.

[151] A. Kilicarslan, K. Grigoriadis, and G. Song, “Compensation of hysteresis in a shape memory alloy wire system using linear parameter-varying gain scheduling control,” *IET Control Theory & Applications*, vol. 8, no. 17, pp. 1875–1885, 2014.

[152] P.-A. Gédouin, E. Delaleau, J.-M. Bourgeot, C. Join, S. A. Chirani, and S. Calloch, “Experimental comparison of classical PID and model-free control: position control of a shape memory alloy active spring,” *Control Engineering Practice*, vol. 19, pp. 433–441, 2011.

[153] M. Fliess and C. Join, “Model-free control and intelligent PID controllers: towards a possible trivialization of nonlinear control?,” in *Proceedings of the 15th IFAC Symposium on System Identification*, pp. 1531–1550, 2009.

[154] S. Majima, K. Kodama, and T. Hasegawa, “Modeling of shape memory alloy actuator and tracking control system with the model,” *IEEE Transactions on Control Systems Technology*, vol. 9, no. 1, pp. 54–59, 2001.

[155] G. Song, V. Chaudhry, and C. Batur, “A neural network inverse model for a shape memory alloy wire actuator,” *Journal of Intelligent Material Systems and Structures*, vol. 14, pp. 371–377, 2003.

[156] A. Kumagi, T. I. Liu, and P. Hozian, “Control of shape memory alloy actuators with a neuro-fuzzy feedforward model element,” *Journal of Intelligent Manufacturing*, vol. 17, no. 1, pp. 45–56, 2006.

[157] A. Rezaeeian, A. Y. Koma, B. Shasti, and A. Doosthoseini, “ANFIS modeling and feedforward control of shape memory alloy actuators,” in *Proceedings of the 10th WSEAS International Conference on Automatic Control, Modelling & Simulation, ACMOS 2008*, pp. 243–248, 2008.

[158] K. K. Leang, S. Ashley, and G. Tchoupo, "Iterative and feedback control for hysteresis compensation in SMA," *Journal of Dynamic Systems, Measurement, and Control*, vol. 131, no. 1, pp. 014502–1–014502–6, 2009.

[159] H. Ashrafiuon and V. R. Jala, "Sliding mode control of mechanical systems actuated by shape memory alloy," *Journal of Dynamic Systems, Measurement, and Control*, vol. 131, pp. 1–6, 2009.

[160] M. Elahinia, *Effect of System Dynamics on Shape Memory Alloy Behavior and Control*. PhD thesis, Virginia Polytechnic Institute and State University, Blacksburg, Virginia, USA, 2004.

[161] M. H. Elahinia, T. M. Seigler, D. J. Leo, and M. Ahmadian, "Nonlinear stress-based control of a rotary SMA-actuated manipulator," *Journal of Intellligent Materials, Systems and Structures*, vol. 15, pp. 495–508, 2004.

[162] M. H. Elahinia and M. Ahmadian, "Application of the extended Kalman filter to control of a shape memory alloy arm," *Smart Materials and Structures*, vol. 15, no. 5, pp. 1370–1384, 2006.

[163] J. S. Ruth, S. Nakshatharan, and Dhanalakshmi, "Differential resistance feedback control of a self-sensing shape memory alloy actuated system," *ISA Transactions*, vol. 53, no. 2, pp. 289–297, 2014.

[164] C.-C. Lan and C.-H. Fan, "An accurate self-sensing method for the control of shape memory alloy actuated flexures," *Sensors and Actuators A: Physical*, vol. 163, no. 1, pp. 323–332, 2010.

[165] T.-M. Wang, Z.-Y. Shi, D. Liu, C. Ma, and Z.-H. Zhang, "An accurately controlled antagonistic shape memory alloy actuator with self-sensing," *Sensors*, vol. 12, no. 6, pp. 7682–7700, 2012.

[166] W. S. Galinaitis, *Two methods for modeling scalar hysteresis and their use in controlling actuators with hysteresis*. PhD thesis, Virginia Polytechnic Institute and State University, Blacksburg, Virginia, USA, 1999.

[167] C. Ru, L. Chen, B. Shao, W. Rong, and L. W. Sun, "A hysteresis compensation method of piezoelectric actuator: model, identification and control," *Control Engineering Practice*, vol. 17, no. 9, pp. 1107–1114, 2009.

[168] K. K. Ahn and N. B. Kha, "Improvement of the performance of hysteresis compensation in SMA actuators by using inverse Preisach model in closed-loop control system," *Journal of Mechanical Science and Technology*, vol. 20, no. 5, pp. 634–642, 2006.

[169] D. Hughes and J. Wen, "Preisach modeling and compensation for smart material hysteresis," in *Active Materials and Smart Structures. Proceedings of SPIE on*, vol. 2427, pp. 50–64, 1994.

[170] G. V. Webb, D. C. Lagoudas, and A. J. Kurdila, "Hysteresis modeling of SMA actuators for control applications," *Journal of Intelligent Material Systems and Structures*, vol. 9, no. 6, pp. 432–448, 1998.

[171] H. Rodrigue, W. Wang, M.-W. Han, T. J. Y. Kim, and S.-H. Ahn, "An overview of shape memory alloy-coupled actuators and robots," *Soft Robotics*, vol. 4, no. 1, pp. 3–15, 2017.

[172] H. Meier and A. Czechowicz, "Computer-aided development and simulation tools for shape-memory actuators," *Metallurgical and Materials Transactions A*, vol. 43, no. 8, pp. 2882–2890, 2012.

[173] A. Schiele, P. Letier, R. van der Linde, and F. van der Helm, "Bowden cable actuator for force-feedback exoskeletons," in *2006 IEEE/RSJ International Conference on Intelligent Robots and Systems*, pp. 3599–3604, Oct 2006.

[174] J. Mohd Jani, M. Leary, and A. Subic, "Designing shape memory alloy linear actuators: a review," *Journal of Intelligent Material Systems and Structures*, vol. 28, no. 13, pp. 1699–1718, 2017.

[175] V. Novák, P. Sittner, G. N. Dayananda, F. M. Braz-Fernandes, and K. K. Mahesh, "Electric resistance variation of NiTi shape memory alloy wires in thermomechanical tests: experiments and simulation," *Materials Science and Engineering: A*, vol. 481-482, pp. 127–133, May 2008.

[176] H. Song, E. Kubica, and R. Gorbet, "Resistance modelling of SMA wire actuators," in *Smart materials, structures & NDT in aerospace*, 2011.

[177] H. Meier and L. Oelschlaeger, "Numerical thermomechanical modelling of shape memory alloy wires," *Materials Science and Engineering: A*, vol. 378, pp. 484–489, Jul 2004.

[178] R. Velázquez and E. E. Pissaloux, "Modelling and temperature control of shape memory alloys with fast electrical heating," *International Journal of Mechanics and Control*, vol. 13, no. 2, pp. 1–8, 2012.

[179] M. A. Iadicola and J. A. Shaw, "An experimental method to measure initiation events during unstable stress-induced martensitic transformation in a shape memory alloy wire," *Smart Materials and Structures*, vol. 16, pp. 155–169, Jan 2007.

[180] J. Van Humbeeck, "Non-medical applications of shape memory alloys," *Materials Science and Engineering: A*, vol. 273, pp. 134–148, 1999.

[181] F. Schiedeck and S. Mojrzisch, "Design of a robust control strategy for the heating power of shape memory alloy actuators at full contraction based on electric resistance feedback," *Smart Materials and Structures*, vol. 20, no. 4, p. 045002, 2011.

[182] L. C. Brinson and M. S. Huang, "Simplifications and comparisons of shape memory alloy constitutive models," *Journal of intelligent material systems and structures*, vol. 7, no. 1, pp. 108–114, 1996.

[183] F. Auricchio and E. Sacco, "A one-dimensional model for superelastic shape-memory alloys with different elastic properties between austenite and martensite," *International Journal of Non-Linear Mechanics*, vol. 32, no. 6, pp. 1101–1114, 1997.

[184] C. Liang, *The constitutive modeling of shape memory alloys.* PhD thesis, Virginia Polytechnic Institute and State University, 1990.

[185] M. H. Elahinia and M. Ahmadian, "An enhanced SMA phenomenological model: II. The experimental study," *Smart materials and structures*, vol. 14, no. 6, pp. 1309–1319, 2005.

[186] A. Flores, D. Copaci, A. Martín, D. Blanco, and L. Moreno, "Smooth and Accurate control of multiple Shape Memory Alloys based actuators via low cost embedded hardware," in *Workshop on Smart materials and alternative techonologies for bio-inspired robots and systems at: IEEE/RSJ International Conference on Intelligent Robots and Systems (IROS)*, 2012.

[187] C. Bruni, G. Dipillo, and G. Koch, "Bilinear systems: An appealing class of nearly linear systems in theory and applications," *IEEE Transactions on Automatic Control*, vol. 19, no. 4, pp. 334–348, 1974.

[188] A. Dunoyer, K. J. Burnham, A. Heeley, and S. Marcroft, "Control of continuously-operated high temperature furnaces," in *Proceedings of the UKACC International Conference on CONTROL '98*, vol. 1, pp. 422–427, Sept. 1998.

[189] K. J. Burnham, A. Dunoyer, D. F. Hibberd, and J. A. Minihan, "A bilinear controller with PID structure," in *Proceedings of the American Control Conference*, pp. 4363–4367, June 1999.

[190] S. Martineau, K. J. Burnham, O. C. L. Haas, G. Andrews, and A. Heeley, “Four-term bilinear PID controller applied to an industrial furnace,” *Control Engineering Practice*, vol. 12, no. 4, pp. 457–464, 2004.

[191] R. R. Mohler and R. E. Rink, “Control with a multiplicative model,” *ASME Journal of Basic Engineering*, vol. 91, pp. 201–205, 1969.

[192] A. P. Dunoyer, *Bilinear self-tuning control and bilinearisation of nonlinear industrial systems.* PhD thesis, Coventry University, Covventry, UK, 1996.

[193] R. E. Rink and R. Mohler, “Completely controllable bilinear systems,” *SIAM Journal on Control*, vol. 6, no. 3, pp. 477–486, 1968.

[194] A. Dunoyer, L. Balmer, K. J. Burnham, and D. J. G. James, “On the characteristics of practical bilinear model structures,” *International Journal of Systems Science*, vol. 22, no. 2, pp. 43–58, 1996.

[195] A. Dunoyer, L. Balmer, K. J. Burnham, and D. J. G. James, “On the discretisation of single-input single-output bilinear systems,” *International Journal of Control*, vol. 68, no. 22, pp. 361–372, 1997.

[196] C.-C. Lan, J.-H. Wang, and C.-H. Fan, “Optimal design of rotary manipulators using shape memory alloy wire actuated flexures,” *Sensors and Actuators A: Physical*, vol. 153, pp. 258–266, Aug. 2009.

[197] S. Strauss, “Extravehicular mobility unit training suit symptom study report,” tech. rep., NASA, 2004.

[198] R. R. Bishu and G. Klute, “The effects of extra vehicular activity (EVA) gloves on human performance,” *International Journal of Industrial Ergonomics*, vol. 16, pp. 165–174, Sep 1995.

[199] M. Mesloh, S. England, E. Benson, S. Thompson, and S. Rajulu, “The effects of extravehicular activity (EVA) glove pressure on hand strength,” in *3rd International Conference on Applied Human Factors and Ergonomics*, 2010.

[200] S. Appendino, A. Battezzato, F. C. Chen, A. Favetto, M. Mousavi, and F. Pescarmona, “Effects of EVA spacesuit glove on grasping and pinching tasks,” *Acta Astronautica*, vol. 96, pp. 151–158, Mar 2014.

[201] S. Appendino, E. P. Ambrosio, F. C. Chen, A. Favetto, D. Manfredi, M. Mousavi, and F. Pescarmona, “Effects of EVA glove on hand performance,” in *41st International Conference on Environmental Systems*, 2011.

[202] M. Mousavi, S. Appendino, A. Battezzato, F. C. Chen, A. Favetto, and F. Pescarmona, "Stiffness of an EVA glove: objective evaluation and testing procedures," in *12th Symposium on Advanced Space Technologies in Robotics and Automation (ASTRA)*, 2013.

[203] C. Walz and M. Gernhardt, "Extravehicular activity - challenges in planetary exploration." 3^{rd} Space Exploration Conference and Exhibit, 2008.

[204] J. A. Main, S. W. Peterson, and A. M. Strauss, "A prototype power assist EVA glove," in *21st International Conference on Environmental Systems*, 1991.

[205] J. A. Main, S. W. Peterson, and A. M. Strauss, "Power assist EVA glove development," in *22nd International Conference on Environmental Systems*, 1992.

[206] E. A. Sorenson, R. M. Sanner, R. D. Howard, D. L. Akin, B. Lingo, and D. Cadogan, "Development of a power-assisted space suit glove joint," in *27th International Conference on Environmental Systems*, 1997.

[207] E. Sorenson, R. Sanner, and C. Ranniger, "Experimental testing of a power-assisted space suit glove joint," in *1997 IEEE International Conference on Systems, Man, and Cybernetics. Computational Cybernetics and Simulation*, vol. 3, pp. 2619–2625, 1997.

[208] Y. Yamada, T. Morizono, S. Sato, T. Shimohira, Y. Umetani, T. Yoshida, and S. Aoki, "Proposal of a SkilMate finger for EVA gloves," in *2001 IEEE International Conference on Robotics and Automation (ICRA)*, vol. 2, pp. 1406–1412, 2001.

[209] T. E. Pillsbury, C. S. Kothera, N. M. Wereley, and D. L. Akin, "Pneumatically power assisted extra-vehicular activity glove," in *45th International Conference on Environmental Systems*, 2015.

[210] A. Favetto, F. C. Chen, E. P. Ambrosio, D. Manfredi, and G. C. Calafiore, "Towards a hand exoskeleton for a smart EVA glove," in *2010 IEEE International Conference on Robotics and Biomimetics (ROBIO)*, pp. 1293–1298, Dec 2010.

[211] A. Favetto, E. P. Ambrosio, S. Appendino, F. C. Chen, D. Manfredi, M. Mousavi, F. Pescarmona, and G. C. Calafiore, "A preliminary study towards an EVA glove exoskeleton," in *11th Symposium on Advanced Space Technologies in Robotics and Automation (ASTRA)*, 2011.

[212] A. Favetto, E. P. Ambrosio, S. Appendino, A. Battezzato, F. C. Chen, D. Manfredi, M. Mousavi, and F. Pescarmona, "Embedding an exoskeleton hand in

the astronaut's EVA glove: Feasibility and ideas," *International Journal of Aerospace Sciences*, vol. 1, pp. 68–76, Jan 2012.

[213] B. Shields, J. Main, S. Peterson, and A. Strauss, "An anthropomorphic hand exoskeleton to prevent astronaut hand fatigue during extravehicular activities," *IEEE Transactions on Systems, Man, and Cybernetics - Part A: Systems and Humans*, vol. 27, pp. 668–673, Sep 1997.

[214] A. Favetto, *Glove Exoskeleton for Extra-Vehicular Activities - Analysis of Requirements and Prototype Design.* PhD thesis, Politecnico di Torino, 2014.

[215] E. Matheson and G. Brooker, "Augmented robotic device for EVA hand manoeuvres," *Acta Astronautica*, vol. 81, pp. 51–61, Dec 2012.

[216] P. Freni, E. M. Botta, L. Randazzo, and P. Ariano, *Innovative Hand Exoskeleton Design for Extravehicular Activities in Space.* SpringerBriefs in Applied Sciences and Technology, Springer International Publishing, 2014.

[217] M. A. Diftler, C. A. Ihrke, L. B. Bridgwater, J. M. Rogers, D. R. Davis, D. M. Linn, E. A. Laske, K. G. Ensley, and J. H. Lee, "RoboGlove - A grasp assist device for earth and space," in *45th International Conference on Environmental Systems*, 2015.

[218] J. M. Rogers, B. J. Peters, E. A. Laske, and E. R. McBryan, "Initial work toward a robotically assisted extravehicular activity glove," in *46th International Conference on Environmental Systems*, 2016.

[219] H. W. Jones, "The recent large reduction in space launch cost," in *48th International Conference on Environmental Systems*, 2018.

[220] P. H. Sutter, J. C. Iatridis, and N. V. Thakor, "Response to reflected-force feedback to fingers in teleoperations," in *NASA Conference on Space Telerobotics*, vol. 4, pp. 65–74, 1989.

[221] A. Hadi, K. Alipour, S. Kazeminasab, A. Amerinatanzi, and M. Elahinia, "Design and prototyping of a wearable assistive tool for hand rehabilitation using shape memory alloys," in *ASME 2016 Conference on Smart Materials, Adaptive Structures and Intelligent Systems*, pp. 1–7, American Society of Mechanical Engineers, 2016.

[222] J. M. Rogers, B. J. Peters, E. A. Laske, and E. R. McBryan, "Development and testing of robotically assisted extravehicular activity gloves," in *47th International Conference on Environmental Systems*, 2017.

[223] D. K. Dittmer, R. O. Buchal, D. E. MacArthur, *et al.*, "The SMART wrist-hand orthosis (WHO) for quadriplegic patients.," *JPO: Journal of Prosthetics and Orthotics*, vol. 5, no. 3, p. 73, 1993.

[224] T. Tang, D. Zhang, T. Xie, and X. Zhu, "An exoskeleton system for hand rehabilitation driven by shape memory alloy," in *Robotics and Biomimetics (ROBIO), 2013 IEEE International Conference on*, pp. 756–761, IEEE, 2013.

[225] A. M. B. Hamid, M. R. Makhdoomi, T. Saleh, and M. Bhuiyan, "Development of a shape memory alloy (SMA) based assistive hand," in *Advanced Materials Research*, vol. 1115, pp. 454–457, Trans Tech Publ, 2015.